Simulation of Red Blood Cells in microcapillaries: on the study of a deformable particle in steady and oscillating Poiseuille flow.

Dissertation

zur Erlangung des Grades des Doktors der
Naturwissenschaften der Naturwissenschaftlich-Technischen
Fakultäten der Universität des Saarlandes

Von

Zakaria Boujja

Saarbrücken
2019

Tag des Kolloquiums:	October 22nd, 2019
Dekan:	Prof. Dr. Guido Kickelbick
Berichterstatter:	Prof. Dr. Christian Wagner
	Prof. Dr. Jens Harting
Vorsitz:	Prof. Dr. Rolf Pelster
Akad. Mitarbeiter:	Dr. Herbert Wolf

"Panta rhei" Everything flows

Heraclitus

Abstract: Red blood cells (RBCs) are the major cellular component of blood (about 98%). Therefore, they are the principal responsible for blood dynamics. At the scale of cells, the inertial forces are negligible and the blood flow is modeled with the Stokes equation.
In this thesis, we present a two-dimensional numerical study of RBC behavior under flow using the capsule and the vesicle model. First, in a shear flow, we compare the motion and deformation of the shape in both models. Next, we investigate the behavior of a single, and a pair of vesicles in a steady and oscillating Poiseuille flow. For the steady Poiseuille flow the shape of the vesicle depends on the flow strength, the mechanical properties of the membrane, and the width of the channel as reported in the past. The oscillation of the flow is introduced using amplitude modulation of the Poiseuille flow to mimic the pulsatile flow in the human circulatory system. We found that the flow oscillation can accelerate the transition of the vesicle from its initial to its final shape. We also observed shape transition of the Snaking shape (a shape where the vesicle shows an oscillatory motion like a swimmer flagella) to parachute or unconfined slipper shapes. For the pair of vesicles, the flow oscillation also decreases the distance between the vesicles. The influence of the oscillation flow was only observed for low flow rate. While for a higher rate, as the shape transition becomes instantaneous the influence of flow oscillation is then insignificant.

Kurzzusammenfassung: Rote Blutzellen (RBCs, engl. Red Blood Cells) sind der zelluläre Hauptbestandteil des Blutes (ca. 98%). Aufgrunddessen sind sie hauptverantwortlich für die dynamischen Eigenschaften des Blutes. Auf zellulärer Ebene sind die Inertialkräfte vernachlässigbar und die Blutströmung wird durch die Stokes-Gleichung modelliert.
In der vorliegenden Arbeit präsentieren wir eine zweidimensionale numerische Studie des Verhaltens von RBC in Strömung mithilfe des Kapsel- sowie des Vesikelmodells. Als Erstes wird die Bewegung sowie die Deformation in beiden Modellen im Scherfluss verglichen. Im nächsten Schritt untersuchen wir das Verhalten eines einzelnen sowie eines Vesikelpaars in stationärer sowie oszillierender Poiseuilleströmung. Für stationäre Poiseuilleströmung wurde in der Vergangenheit bereits aufgezeigt, dass die Form des Vesikels von der Flussstärke, den mechanischen Eigenschaften der Membran sowie der Kanalbreite abhängt. Die Oszillation der Strömung wird mittels Amplitudenmodulation des Poiseuilleflusses erreicht und ahmt die pulsierende Strömung im menschlichen Kreislaufsystem nach. Es zeigte sich, dass die Strömungsoszillation den Übergang des Vesikels von seinem Anfangs- zu seinem Endzustand beschleunigen kann. Wir beobachteten auch den Übergang der «Snaking»-Form (ein Zustand, bei dem das Vesikel eine oszillierende Bewegung ähnlich einem Flagellum vollführt) zur «parachute»- oder «unconfined slipper»-Form. Für ein Vesikelpaar führt die Oszillation auch zu einer Verringerug des Abstandes zwischen den Vesikeln. Der Einfluss der oszillierenden Strömung wurde nur für niedrige Flussraten beobachtet. Für höhere Flussraten ist der Einfluss der Oszillation unerheblich, da der Übergang zwischen den Formen instantan erfolgt.

Acknowledgements

First I would like to express my immense gratitude to my supervisors, Prof. Christian Wagner, Prof. Hamid Ez-Zahraoui, and Dr. Chaouqi Misbah. They gave me this valuable chance to explore a new topic in the field of fluid dynamics. I would particularly thank Prof. Wagner, with whom I spent most of my time during my Ph.D. within his research group, for his permanent, and unconditional help. Without his guidance, his support and his patience, this work would have never been achieved. I want to especially thank Prof. Abdelillah Benyoussef, Prof. Martin Michael Müller, and Dr. Thomas John for their help and all the productive discussions, and their precious advice.

Many thanks to all my friends and colleagues, with whom I shared the most precious moments of my life. Alexander Kihm, Andreas Christ, Asena Abay, Christian Ruloff, Daiki Matsunaga, Daniel Flormann, Ettore Bernardi, Greta Simionato, Javad Najafi, Jorge Fiscina, Julie Martin-Wortham, Lars Kaestner, Lee Kisung, Matthias Brust, Oliver Köhn, Othmane Aouane, Revaz Chachanidze, Rishab Handa, Sebastien Himbert, Stephan Quint, Viviana Claveria, and those who I may have forgotten to mention. Thanks to all of you, for your kindness, for the "Saarbrücken Friday nights", for those movie nights, for the delicious shared cakes and cookies, for the Mensa time, and all the barbecues and birthday parties we had together. Many thanks also go to Ms. Elke Huschens and Ms. Karin Kretsch who always were present when I needed help.

Above all, I want to thank my awesome family, my parents Jamila and Abdelfettah, my brothers Anoir, Yassine and Nassim, my sister Bouchra, my grandparents Fatima, Omar, my uncles Khalid, Mohamed, my aunts Hafida, Leila, and Rachida, and all my cousins. You are the lighthouse that guides me. I love you from the depths of my heart.

Contents

Acknowledgements vi

General Introduction 1

State of the art 4

1 Generalities about Blood 6
- 1.1 Blood components . . . 7
  - 1.1.1 Plasma . . . 7
  - 1.1.2 Leukocytes . . . 7
  - 1.1.3 Platelets . . . 8
  - 1.1.4 Erythrocytes . . . 8
- 1.2 The Cell Membrane . . . 8
- 1.3 The Cytoskeleton . . . 9
- 1.4 Experimental Methods for Measuring Cell Mechanics . . . 9
- 1.5 Blood viscosity . . . 11
- 1.6 The circulatory system . . . 12
  - 1.6.1 Arteries . . . 13
  - 1.6.2 Arterioles . . . 13
  - 1.6.3 Capillaries . . . 13
  - 1.6.4 Venules and Veins . . . 14
- 1.7 Conclusion . . . 14

2 RBC Modelization 16
- 2.1 Vesicles and Capsules . . . 17
- 2.2 Mechanical properties of membranes . . . 18
  - 2.2.1 Equilibrium shapes . . . 18
  - 2.2.2 Bending energy . . . 19
  - 2.2.3 Elastic in-plane energy . . . 20
  - 2.2.4 Area dilatation energy . . . 22
  - 2.2.5 Membrane forces . . . 22
  - 2.2.6 Membrane-membrane interaction . . . 24
- 2.3 The numerical methods . . . 24
  - 2.3.1 Immersed Boundary method . . . 25
  - 2.3.2 Element Boundary methods . . . 25
- 2.4 Hydrodynamic equations . . . 30
- 2.5 Conclusion . . . 32

3 Cells under flow 34
- 3.1 Algorithm . . . 35
- 3.2 Single cells in shear flow . . . 37
  - 3.2.1 Vesicles under shear flow . . . 37
  - 3.2.2 Capsules under shear flow . . . 38

3.3 Vesicles in Poiseuille flow . . . 41
3.3.1 Steady shapes . . . 42
3.3.2 The snaking shape . . . 45
3.4 Vesicles in modulated Poiseuille flow . . . 49
3.4.1 Steady shapes . . . 51
3.4.2 The snaking shape . . . 53
3.5 Two vesicles in Poiseuille flow . . . 60
3.6 Conclusion . . . 64

4 Flow fields **66**
4.1 Flow field for a single vesicle . . . 67
4.1.1 Shear flow . . . 67
4.1.2 Poiseuille flow . . . 68
4.2 Flow field for two vesicles . . . 71
4.2.1 Pair of parachute . . . 71
4.2.2 Pair of slipper . . . 71
4.3 Conclusion . . . 72

Conclusion & perspectives. **73**

Appendices **75**

A Free-space Green's function for steady Stokes flow **76**

B Boundary integral representation of unbounded steady Stokes flow **80**

C Boundary integral representation for flow past a closed interface **85**

Bibliography **88**

General Introduction

Blood is a fluid that fascinated many civilizations since ancient times and made it one of the most important subjects of study in human history. The first medical practices in antiquity were all related to the physical properties of blood. Therefore, the hemorheology, the study of the flow properties of blood, is considered as one of the oldest research fields in human history [1].
Probably the first phenomenon related to blood that was studied is the blood sedimentation. The ancient Greeks noticed that sedimented blood generally forms four layers, which led them to conclude that blood is composed of four fluids. The top layer is the blood plasma and was referred to yellow bile or cholera due to its color. The second layer that consists of white blood cells and platelets was called phlegm or the mucus due to its colorless and viscous form. The third layer contains the red blood cells (RBC), called sanguine or blood. Finally, the last layer is filled with deoxygenated RBC, called the black bile for its deep red color [2]. In ancient times, Greeks used this separation as a diagnostic tool, where any disproportion between the four layers was associated with diseases.
This concept has origins in ancient Egyptian medicine, but Hippocrates (460-370 BC) was the one who applied this idea to medicine. In his work *On the Nature of Man*, he describes the theory as follows: "*The Human body contains blood, phlegm, yellow bile, and black bile. These are the things that make up its constitution and cause its pains and health. Health is primarily that state in which these constituent substances are in the correct proportion to each other, both in strength and quantity, and are well mixed. Pain occurs when one of the substances presents either a deficiency or an excess, or is separated in the body and not mixed with others.*"[3].
Hippocrates laid the foundation of Greek medicine which was spread far and wide throughout the entire world and expanded by other physicians and philosophers from Romans to nowadays. One of the greatest physicians of the Roman empire was Claudius Galenus (129-216 BC) often anglicized as Galen. He was a supporter of the humoral theory of Hippocrates. In his view, an imbalance in one of the four bodily fluids corresponded to a particular human temperament.
Based on the humoral theory, and the effect of disproportion of the blood layers in disease, the physicians began to develop techniques to correct this imbalance and thus relieve the patient. The most common method used was the bloodletting. It consists of withdrawing blood from a patient by lancing a major vessel or by using leeches to balance the components. This method often resulted in the death of patients.
During the Renaissance, classical Greco-Roman and Islamic science flocked to Europe, and a new era of scientific progress was in the air. Leonardo da Vinci (1452-1519) was one of the most exceptional scientists of that time. There was a moment at which his passion for art leads him to the study of human anatomy, not to improve his drawing, but to understand its functioning. Some of these drawings have survived in the *Leicester Codex*. Alongside with these representations, he paid particular attention to the vortices of water flowing around different obstacles, which seems

to be the basis of his later studies on the heart mechanisms, and the blood flow, in which he devoted much of his time between 1508 and 1513 [4]. From these drawings, comes what was later acknowledged to be the first hemodynamic records. In one of his sketch, see Figure 1, Leonardo demonstrates the formation of vortices in the sinus during the closure of the aortic valve.
In the early seventeenth century, William Harvey (1578-1657), an English physician, discovered blood circulation, one of the most significant discoveries of all time, and one of the pivotal points in the history. Before Harvey's discovery, it was thought that blood flowed through the veins and arteries, transmitting the so-called "*vital spirit*" to all tissues and the heart was responsible in the reconstitution of the blood consumed during this process.
In his reasoning, Harvey relied on his observations of the one-way valves in the veins in and around dissected animal hearts [6]. He also hypothesized the existence of microvessels between arteries and veins, but since he did not have access to microscopy, he could not see these microcirculatory vessels. It was left to Marcelo Malpighi (1628-1694) in 1661 who was the first to observe the capillary vessels using one of the first microscopes in human history which proved Harvey's theory [7]. He stated that capillaries were connected to arteries and veins and that they allowed the backflow of blood to the heart in our circulation system.
Besides the discovery of the circulatory system, the true nature of blood remained a mystery. It was considered as a simple liquid, but this began to change with the advent of the microscope. Thirteen years after the first observations of the red blood cells by Malpighi, Anthoni Van Leeuwenhoek (1632-1723), gave the first accurate description of the red cells [8]. He observed the blood flowing in microcirculation,

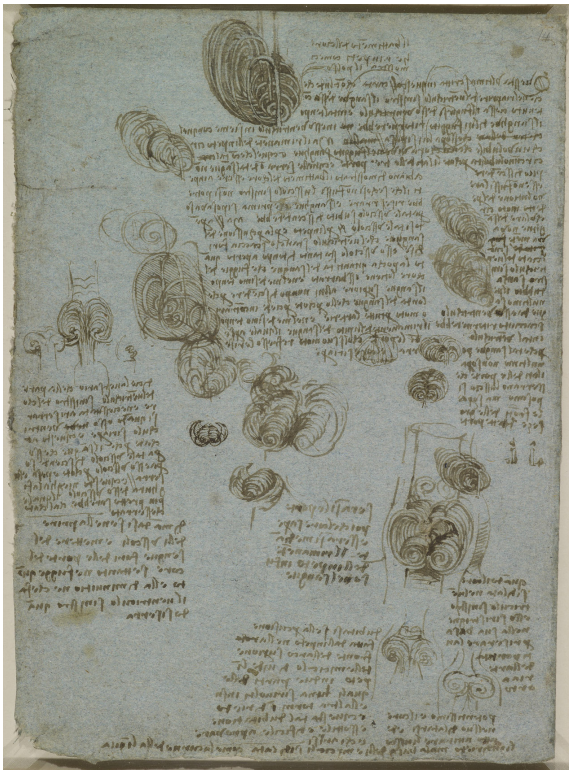

FIGURE 1: Study of vortices in blood flow inside the heart and in the ascending aorta. Various types of waves of blood flow can be seen, with eddies in the opposite direction [5].

and realized that large deformability was necessary for them to pass through the smaller blood capillaries. He also observed RBC aggregation, and even estimated their diameter at 8.5 µm [9].
After Harvey's discovery, physicians and scientists began to investigate the factors that determined the flow of blood in and to different organs. Jean-Leonard-Marie Poiseuille (1797-1869) believed that these factors were linked to the flow properties of the blood. To prove this assumption, he simplified the problem and investigated flow in cylindrical glass tubes. As blood was too difficult to use due to its non-Newtonian behavior, he performed most of his studies on simpler liquids such as water and alcohol. Around 1839-1844 Poiseuille and Gotthilf Heinrich Ludwig Hagen published, experimentally and independently, the Hagen-Poiseuille Law [10, 11], summarized in the equation:

$$\Delta P = \frac{8\mu L Q}{\pi r^4}, \tag{1}$$

where ΔP is the pressure drop between the two ends of the tube, μ is the dynamic viscosity, L and r represent the length and the radius of the tube, respectively, and Q is the volumetric flow rate. This equation is only valid for Newtonian liquids.
Previously in this introduction, blood sedimentation was mentioned and how the ancient Greeks used it as a diagnostic tool. Robin Fåhraeus (1888-1968) provided a clear view of the phenomenon [2]. He studied the factors affecting the blood sedimentation in sickness and in health which led to the development of the Erythrocyte Sedimentation Rate (ESR) test as a valuable quantitative diagnostic tool. Fåhraeus made many other contributions to hemorheology, especially his conclusions resulting from his studies of blood flow in very small diameter glass tubes. In collaboration with the Swedish physician Johan Torsten Lindqvist (1906-2007), he was able to show that the apparent viscosity of blood decreases as the diameter of the tube through which it flows decreases. This is now known as the Fåhraeus-Lindqvist Effect [12]. This effect is due to the migration of RBCs to the center of the vessel, leaving plasma at the boundaries.
During a considerable time, there was no technique for measuring the non-Newtonian blood characteristics until the second half of the twentieth century, when viscometers capable of measuring non-Newtonian viscosity emerged. Initially, the devices were developed for commercial applications on complex liquids, like paints. One of the most remarkable was the Weissenberg Rheogoniometer, manufactured by the Austrian physicist Karl Weissenberg (1893-1976). Subsequently, many physicist and engineers have made a considerable contribution to the hemorheology field by modifying the rheometer instrument to allow its use in blood experiments, and for the first time, data from different laboratories around the world became comparable.
Until now, the main area of research on blood was its viscosity, but with the appearance of new techniques and devices, scientists began to be interested in the mechanical properties of RBCs, and their deformability in particular.

State of the art

In the larger vessels of the human circulatory system like the arteries, blood can be modeled as a homogeneous and non-Newtonian fluid [13]. However, in narrow vessels, like the capillaries (the smallest blood vessels in the body) the blood cells can only travel through them one by one (Figure 2), and therefore, blood in this condition is considered as a suspension of RBCs in plasma, rather than a homogeneous fluid.

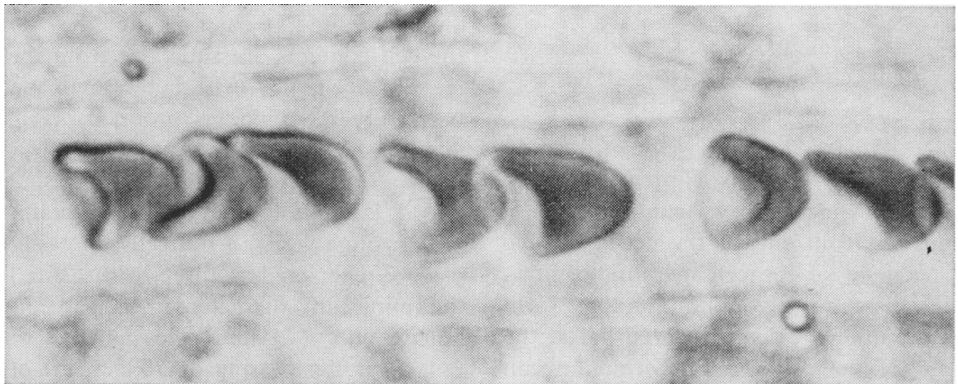

FIGURE 2: Photography of red blood cells flowing in a capillary vessel (from [14]).

The membrane of red blood cells is a lipid bilayer of phospholipids with a network of proteins. Due to this complexity, simplified systems, like vesicles and capsules are used as models for RBCs. Constitute laws, like the Mooney-Rivlin or Skalak laws (see section 2.2), are used to model the membrane mathematically. The membrane model is formulated so that any deviation from the resting shape increases the membrane energy and induces response forces that drive the membrane shape towards a new equilibrium shape. In 1973 Helfrich proposed a constitutive law describing the membrane resistance to bending [15]. For the resistance to stretching, the Neo-Hookean law is the most used because of its simplicity [16, 17] but it is limited to small deformations. For large deformations, Skalak [18] introduced the Skalak constitutive law which accounts for shear deformations and area dilatation.
Two types of methods can be used to solve the fluid-membrane interaction. The first, called the immersed boundary method (IBM), was initially developed by Peskin for the coupled simulation of blood flow and muscle contraction in a beating heart [19]. It consists of two grids, a Eulerian mesh for the fluid domain, whereas a Lagrangian mesh is used for the membrane. The two meshes are then coupled with an approximate Dirac delta function [20]. The second method is called the boundary integral method (BIM), presented first by Youngren and Acrivos [21] for flow past a rigid particle, and later on extended by Pozrikidis [22] for deformable particles. In the BIM approach, only the mesh of the membrane is used, the fluid flow and the membrane energy are coupled using the Lorentz reciprocal formula and the Green's functions (see section 2.3.2).
Under blood flow conditions, RBCs are usually subjected to two types of flow: they

can be locally sheared in large vessels such as arteries or deformed by the parabolic flow in small vessels such as capillaries. Several experimental approaches are used to study RBC behaviors (see section 1.4), e.g., Flow techniques like microfluidic devices are used to mimic the flow condition of RBC in the circulatory system. Goldsmith [23] showed that for smalls shear rate suspensions of single and a rouleau of RBCs rotates like a rigid circular disk, in Poiseuille and shear flow. This was called later the "Tumbling" motion. Using a cone-plate rheometer Fischer [24] showed that in shear flow the RBCs maintain a fixed angle relative to the flow direction, while the membrane is rotating periodically around its center of mass. This motion was named "tank-treading". They also found that the tank-treading frequency and the cell elongation are proportional to the flow shear rate. Later on, Abkarian [25] found that under a moderate shear rate, RBCs adopt a so-called "swinging" motion, where the long axis of the vesicle oscillates up and down about the flow direction. Experimental studies of blood flow in capillary vessels [14, 26] or in microfluidic devices [27, 28] of the same order of diameter as RBC (that is, below 10 µm) observed that the red cells could flow in two shapes, a parachute-like (also called umbrella-like shape), or a slipper-like shape. The parachute shape is symmetrical with respect to the axis of symmetry of the channel, and its center of mass lies on this axis. In contrast, the slipper shape is asymmetric. Its center of mass is shifted vertically, and the membrane shows a tank-treading motion.
Using the vesicle model [29, 30], previous numerical works from Kaoui [31], Tahiri [32], and Aouane [33] showed that a two-dimensional vesicle in a confined Poiseuille flow can adopt three different shapes. The usual symmetric parachute shape, the asymmetrical shapes, confined and unconfined slippers, and a transition shape called "snaking shape". The same shapes were also observed by Fedosov [34] in three-dimensional simulations. In the circulatory system, when the heart contracts to pump the blood, the pressure in the aorta and other large arteries rises and during the expansion falls again. This induces a cyclic oscillation of the vessel walls with a frequency of oscillation equal to that of the heartbeat. This process occurs during every cardiac cycle (every contraction, expansion of the heart), and makes the blood flow in an oscillating manner, in response to the pulsatile pressure [35]. This thesis aims to study, numerically, the effect of this oscillating flow on the RBC shapes.

Chapter 1

Generalities about Blood

Content

1.1 Blood components . . . 7
1.1.1 Plasma . . . 7
1.1.2 Leukocytes . . . 7
1.1.3 Platelets . . . 8
1.1.4 Erythrocytes . . . 8
1.2 The Cell Membrane . . . 8
1.3 The Cytoskeleton . . . 9
1.4 Experimental Methods for Measuring Cell Mechanics . . . 9
1.5 Blood viscosity . . . 11
1.6 The circulatory system . . . 12
1.6.1 Arteries . . . 13
1.6.2 Arterioles . . . 13
1.6.3 Capillaries . . . 13
1.6.4 Venules and Veins . . . 14
1.7 Conclusion . . . 14

This chapter consists of a brief introduction and overview of the human circulatory system, also known as the cardiovascular system, which consists of the heart pumping blood through a closed system of vessels. The primary function of blood is to supply oxygen, nutrients, and other substances to all of the body's tissues and organs, and to remove waste products. We shall briefly describe the blood components, namely the plasma, leukocytes, platelets, and erythrocytes. The latter, also commonly referred as red blood cells (RBCs), constitute by far the major component (about 98%) of blood, and consequently, have the most significant influence on its mechanical properties like the viscosity. The higher viscosity of the blood, the greater its resistance to flow, and more energy is required from the heart to pump it through the circulatory system. We will also describe the cell membrane, a double layer of lipids and proteins that surrounds a cell and separates its content (cytoplasm) from its surrounding environment. It gives the RBC its structure and regulates the exchange of materials between the inner and the outer cell environment. We will also shortly describe some techniques used to measure the mechanical properties of cell membranes. Finally, we will review different types of vessel constituting the circulatory system.

1.1 Blood components

Blood is a viscous, non-homogeneous liquid. Its most important components are red blood cells (or erythrocytes), white cells (or leukocytes), platelets (or thrombocytes), and plasma. The function of blood is to feed all the tissues of the body and to remove waste. The blood travels through a complex vascular network of the human body at a specific flow rate. This rate of circulation is determined by the driving pressure generated by the heart, the geometrical resistance in the vessel network and the flow properties of the blood [36].

1.1.1 Plasma

The plasma is a liquid which mostly contains water (more than 95% of its volume) and a mixture of dissolved proteins, ions, and metabolic molecules. The smallest of the solutes are the ions of dissolved and dissociated inorganic salts. They represent about 1% of the plasma by weight. The most concentrated one is the sodium (Na^+) derived from dissociated sodium chloride ($NaCl$). If its concentration falls or exceeds a certain range (135 to 145 mmol for a healthy human), the RBC shrinks or swells. Therefore, it influences their mechanical properties and, consequently, the viscosity of blood. The other important ion is the potassium HCO_3^-. The concentration in the human body normally lies in the range of 24 to 30 mmol. It is also one of the factors controlling blood pH and maintaining it between 7.35 and 7.45, which is vital for normal functioning of the body. Metabolic molecules such as glucose, urea and amino acids represent about 1% by weight of the plasma. Their concentrations are generally smaller and better controlled than those of the ions mentioned above, which is why they have a relatively minor hemorheological effect. The plasma proteins are all very bulky and represent about 7% of the plasma by weight. They are necessary to carry many vital materials, to protect against infections, to hemostasis, and so forth. From the hemorheological point of view, they are important for two main reasons: first, because of their relatively high concentration and their large size, they have a strong effect on the viscosity of the plasma. The second reason is that some of them cause the RBCs to stick together like stacks of coins, called rouleau so that the viscosity of blood is highly dependent on the shear rate to which it is exposed [1].

1.1.2 Leukocytes

Leukocytes play a vital role in the battle against infections in the body via the destruction of bacteria and viruses and the formation of antibodies and sensitized lymphocytes. Since there is only one leukocyte for 30 platelets and 600 RBCs, the role that plays white cells in determining the viscosity of the whole blood is weak except in microcirculation like capillaries or disease condition. In this case, their influence is increased because they have much greater viscoelastic properties due to their internal contents, and a larger volume compared to RBCs [37].
There are five morphologically different varieties of leukocytes, monocytes which are the largest one, basophils, eosinophils and neutrophils (collectively called granulocytes), and lymphocytes which are the smallest ones.

1.1.3 Platelets

Platelets, also called thrombocytes, are small fragments of non-nucleated discoid cells with a diameter in the order of 2-3 µm, making them much smaller than erythrocytes and leukocytes. Because of that, they do not affect blood viscosity. Their primary role is the prevention of blood loss. When they come into contact with a damaged vascular surface, they release chemicals that activate nearby platelets and make them adhere to each other which lead to a platelet plug which is sufficient to stop bleeding in small wounds. For larger injuries, platelets play an important role in solidifying blood as clots [36].

1.1.4 Erythrocytes

Erythrocytes, or red blood cells, are highly flexible cells made of a two-dimensional fluid bilayer of phospholipids. They are filled with a saturated solution of hemoglobin in water as well as inorganic elements (like potassium and calcium). Hemoglobin is the protein inside RBC that gives blood its red color. It is primarily involved in the transport of oxygen and carbon dioxide between the lungs and body tissues. A Normal human RBC in the unstressed state has the shape of a biconcave disk with a maximum diameter of 8 µm, a thickness of 2.5 µm, a surface area of 140 μm^2 and a volume of 90 μm^3 Figure 1.1. This shape can be changed due to mechanical, chemical or thermal effects. Such a structure allows the cells to undergo large deformations in flow and achieve complex shapes that differ significantly from the biconcave resting shape. Red blood cells are by far the major component (about 98%). Therefore, they have the most significant influence on the mechanical properties of blood. The volume concentration of RBCs in the blood is called hematocrit. The properties of an individual RBC changes with its age. The average lifespan of an RBC in human blood is approximately 120 days [36].

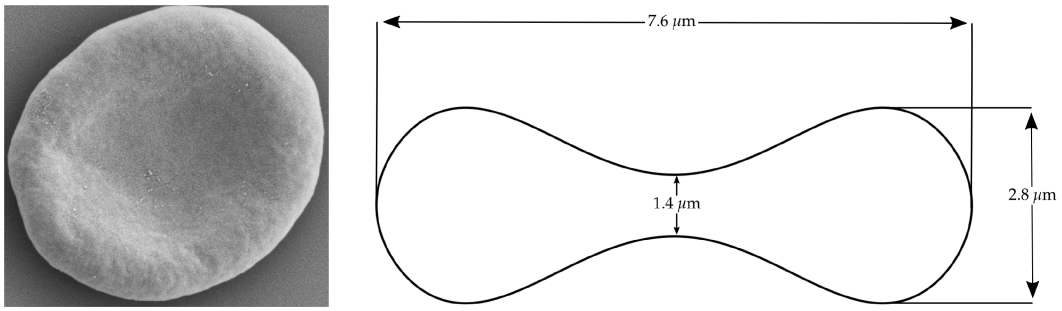

FIGURE 1.1: (a) Scanning electron image of a RBC (with permission from G. Simionato); (b) Profile schematic of a discoid RBC.

1.2 The Cell Membrane

RBCs can deform both due to in-plane stretching and out of plane bending of the membrane. The high deformability of RBC is due to the lack of a nucleus, to the geometric factors such as the shape, volume, and surface, plus the elastic and viscous properties of its membrane [38].

The RBC membrane is an extremely flexible structure composed of two adjacent layers of phospholipids (like all human cells). The lipid tails of one layer, face the lipid tails of the other layer, joining at the interface of the two layers, the phospholipid heads being turned outward. One layer is exposed to the intracellular fluid (the fluid inside the cell) and the other layer is exposed to the extracellular fluid (the surrounding fluid outside the cell membrane). A single phospholipid molecule has a phosphate group at one end, called the "head", and two-sided chains of acids that form the lipid tails. The phosphate group is negatively charged, which makes the head polar and hydrophilic, and therefore attracted by water. Lipid tails, on the other hand, are not charged and are hydrophobic. They repel themselves and are repelled by water. Since the lipid tails are hydrophobic, They meet in the internal region of the membrane, separating the intracellular and extracellular fluid of this space.
RBCs have different proteins distributed on their membrane. Cholesterol is also present, which contributes to the fluidity of the membrane. Various membrane-integrated proteins perform a variety of functions. An essential characteristic of the membrane is that it remains fluid, so the lipids and proteins in the cell membrane are not rigidly blocked (Figure 1.2).

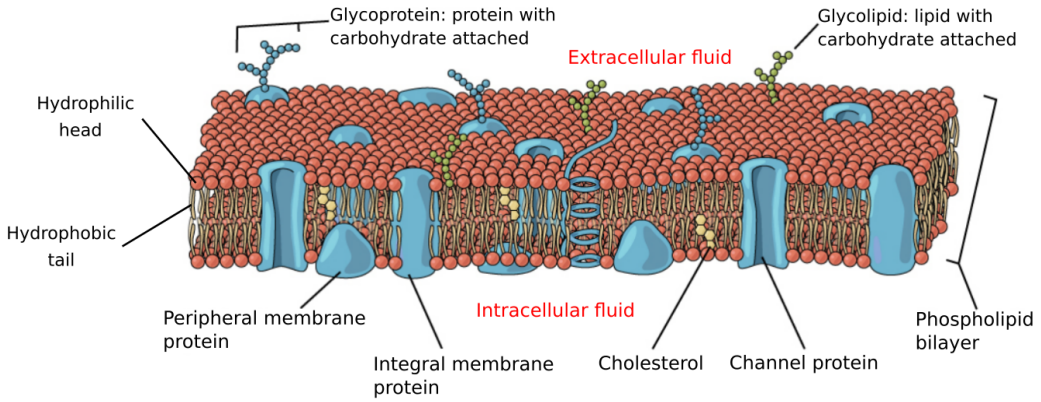

FIGURE 1.2: Sketch of a cell membrane from [36] including phospholipids, proteins and cholesterol.

1.3 The Cytoskeleton

The cytoskeleton forms a complex network of filamentous proteins that provide structural support for cells. It plays an important role in maintaining cell shape, for cellular motility, cell division, and the transportation of substances within the cell. The three major types of cytoskeletal filaments are (i) Microtubules, formed from a protein called tubulin. (ii) Microfilaments, a thin type of filament. The primary component of these filaments is actin protein. The final cytoskeletal filament is (iii) intermediate filaments that are thicker than microfilaments and thinner than microtubules. They are made up of a long fibrous protein called keratin [36, 39].

1.4 Experimental Methods for Measuring Cell Mechanics

One of the most commonly used techniques for measuring RBC deformability is based on the use of small glass micropipettes with similar dimensions of the RBCs,

in which part of the cell membrane is sucked into the pipette. From its radius of curvature and the suction pressure rate, an estimation of the mechanical properties of the membrane could be established [40, 41]. In the same field, another common technique relied on the use of micropore filters. These filters had pores with a similar size of small blood capillaries, and simple filtration methods gave evidence of RBC deformability [42].

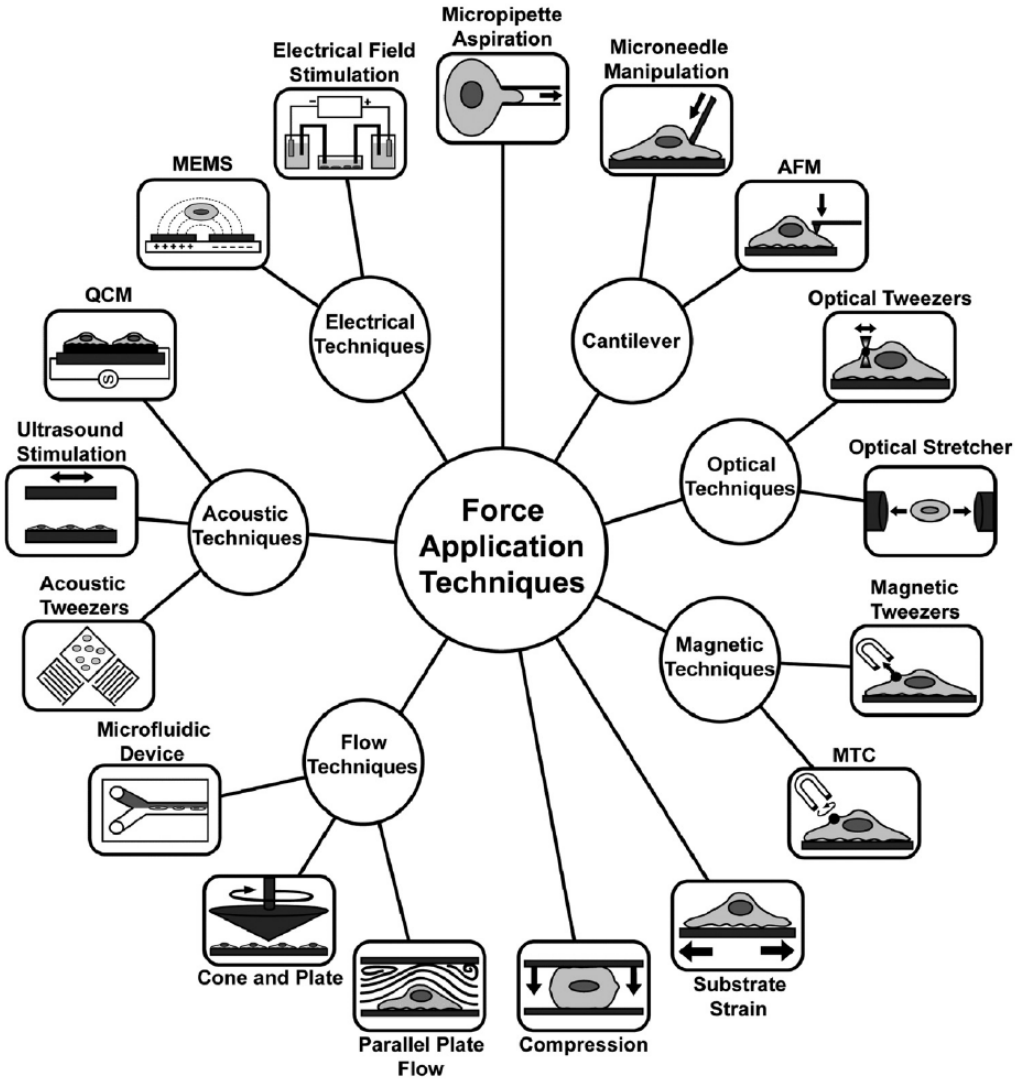

FIGURE 1.3: Picture from [43] illustrating different experimental techniques used to extract different mechanical proprieties of cells.

More complex and more precise experimental techniques for measuring cell mechanics have gradually begun to emerge, such as microneedles, and the atomic force microscope. In microneedle experiments, a thin and flexible fiberglass microneedle is used to push or pull on a cell or one of its subcellular structures, since the glass microneedle acts as a cantilever spring. The deflection of the tip of the needle can determine the force applied to the cell, which can be measured electrically or optically [44, 45]. Atomic force microscopy (AFM) also offers excellent measurement accuracy. It is similar to the manipulation of microneedles in that it also uses a flexible cantilever with a fine tip at its free end. The tip is used to probe a sample of a

cellular structure by measuring its displacement in the vertical direction when the tip is directed downwards by a piezoelectric stage. Using this technique, an approximation of Young's modulus of the indented cell can be determined as a function of the force applied by the AFM, the shape of the AFM tip and the indentation depth [46, 47].
Optical techniques employing photon trapping are also widely used, the most common ones are optical tweezers and optical stretching. The optical tweezers or optical trapping uses an infrared laser and a microscope to trap an object and control its movements through photons. When the photons pass through an object, their direction changes as a function of the refractive index of the object. This change of direction causes a change in momentum resulting in a trapping force on the object. This force can be calculated from the laser intensity gradient, the refractive index of the bead, and the refractive index of the surrounding cell medium [48]. Alternatively, in an optical stretcher, laser light is coupled to one or more optical fibers with fiber couplers and delivered to the cell chamber. Two-dimensional trapping can be achieved using a single beam fiber, while three-dimensional trapping requires two fibers [49]. These systems can be used to trap and, or, stretch cells and have been used primarily to study the mechanical properties of cells [50], their response to stretching [51], and to distinguish between diseased and healthy cells [52].
In another interesting technique, the cell is exposed to a shear flow system to mimic flow conditions in the human body. The three most popular types of shear flow devices are the cone-plate system, the parallel plate flow chamber, and microfluidic devices. In these systems, cells can be subject to laminar, transient or turbulent flow profiles. In the cone-plate system, rotation of the fluid in the cell chamber is induced by rotating the cone perpendicularly to the surface of the plate. The geometry of the rotating cone generates uniform shear stress on the entire cell population of the chamber [53]. Alternatively, in a parallel plate flow chamber, a pressure drop between the openings on either side of the chamber is used to drive the fluid through a layer of cells [25]. There is also a wide range of microfluidic devices developed to study the effect of physical properties of cells. These devices can control the cell environment while simultaneously measuring its mechanics. They can also be designed to approach physiological conditions and can measure several types of mechanical, electrical, and chemical properties of the cell culture [54]. Further techniques for evaluating the mechanical properties of RBCs or cells are shown in Figure 1.3.

1.5 Blood viscosity

Blood viscosity is defined as the ability of blood to flow through the vessels. Experimental studies show that blood behaves as a non-Newtonian fluid. The viscosity of human blood varies dynamically from high shear to low shear during each cardiac cycle: at a higher shear rate (systole), blood is physically thinner, while at a lower shear rate (diastole), blood is thicker and stickier. The phenomenon is known as shear-thinning. The primary determinants of blood viscosity are hematocrit, red blood cell deformability, red blood cell aggregation, and plasma viscosity.
Indeed when the RBCs are subjected to smaller shear rates, they tend to aggregate and stack together. Therefore, the viscoelastic properties of blood are dominated by the aggregation and RBC's deformability is insignificant. As the shear rate increases, the size of the aggregates begins to decrease. The influence of the aggregation properties on the viscoelasticity then drops, and the influence of the deformability of

RBCs begins to increase. At the higher shear rates, the viscoelasticity of the blood only depends on the RBC's deformability [1].

1.6 The circulatory system

The human circulatory system consists of a muscular pumping mechanism, the heart, and a closed network of vessels. The heart pumps the blood, which is rich in oxygen, and nutrients contained in the system around a circuit of vessels, providing all the body's tissues with the blood by the process of bulk flow.

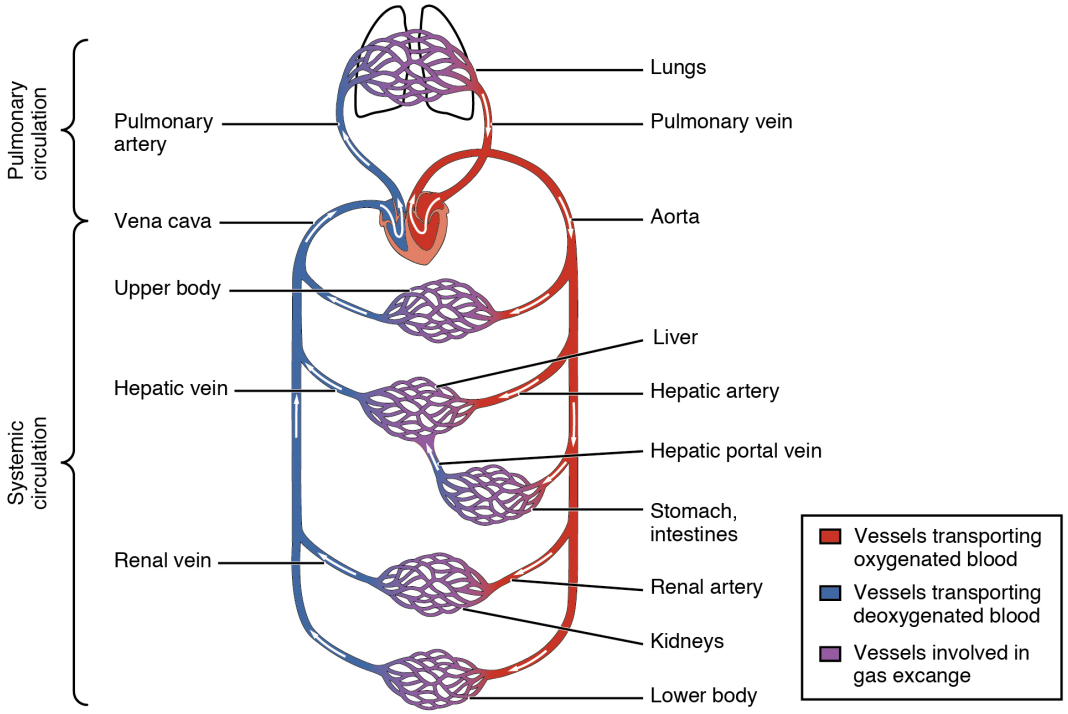

FIGURE 1.4: Schematic of the human cardiovascular circulation [36].

Through this process, air and blood pass from high-pressure regions to low-pressure regions. In the human circulatory system, the heart is the pump that generates the pressure gradients that cause the bulk flow of blood. Such a system allows rapid transport of respiratory gas molecules and nutrients over long distances to reach all tissues of the body [36].
The circulatory system is composed of two separate circuits. The pulmonary circuit (supplied by the right side of the heart), receives blood returning to the heart from the body and pumps it to the lungs. This circuit serves to exchange carbon dioxide in the blood with oxygen from the lungs. The systemic circuit (supplied by the left side of the heart) takes the freshly oxygenated blood and delivers it to the entire body. In both circuits, the blood passes through a series of blood vessels. Blood is pumped out of the heart into large muscle arteries that branch out into smaller arteries, then the arterioles, followed by intricate networks of tiny capillaries. Capillaries are the sites of exchange between blood and neighboring cells. After leaving the capillaries, the blood is collected in venules and veins of increasing size, before being returned to the heart. In both systems, the arteries remove the blood from the heart, and the veins bring blood to the heart. To keep the body's blood in motion, the heart pumps

about 8000 liters of blood per day.
Within each of the two circuits, there are five basic types of blood vessels: arteries, arterioles, capillaries, venules, and veins. Each type of blood vessel differs in their structure, but they share the same general features.

1.6.1 Arteries

An artery is a blood vessel that conducts blood away from the heart and distributes it to all of the body's tissues, including the heart itself. First, blood enters large arteries that immediately begin to branch into medium-sized and then smaller arteries. The larger arteries have elastic walls that can withstand the high pressure of the blood ejected from the heart. The medium-sized arteries distribute blood to skeletal muscles and major organs. These arteries, in general, have a thinner muscle layer, but the difference in arterial structure from the larger arteries is insignificant. The elastic retraction of the vascular wall helps to maintain arterial pressure [36].

1.6.2 Arterioles

Arterioles, also called resistance vessels, are very small arteries that lead to capillaries. They have an inner layer of smooth muscle cells connected to the central neural system. If the arterioles receive a signal to increase their diameter (or vasodilate), blood pressure is reduced. Conversely, when stimulated to decrease their diameter (or vasoconstrict), they resist blood flow and increase blood pressure. These vessels play the most critical role in the determination of blood pressure, as they are the primary site of resistance and regulation of blood pressure [36].

1.6.3 Capillaries

Capillaries are the smallest blood vessels in the body. They are microscopic channels that supply blood to tissues, a process called perfusion. Exchange of gases and other substances occurs in the capillaries between the blood and the interstitial fluid of the surrounding cells. The diameter of a capillary range from 5 to 10 µm, just barely wide enough for an RBC to squeeze through.
Flow through capillaries is often described as microcirculation. The wall of a capillary consists of the endothelial layer surrounded by a basement membrane with occasional smooth muscle fibers. The walls of the capillaries leak, letting the substances pass through. There are three main types of capillaries, which differ according to their degree of leakiness: continuous, fenestrated, and sinusoidal capillaries (Figure 1.5).
Continuous capillaries are the most common. They are characterized by a complete endothelial lining with tight junctions between endothelial cells. Although a tight junction is generally impermeable and allows only the passage of water and ions, they are often incomplete in the capillaries, leaving intercellular slits allowing the exchange of water and other very small molecules between the blood plasma and the interstitial fluid. A fenestrated capillary has pores in addition to tight junctions in the endothelial lining. These pores make the capillary permeable to larger molecules. They are common in the small intestine, which is the main site of absorption of nutrients, as well as in the kidneys, which filter the blood. They are also found in many other endocrine structures.

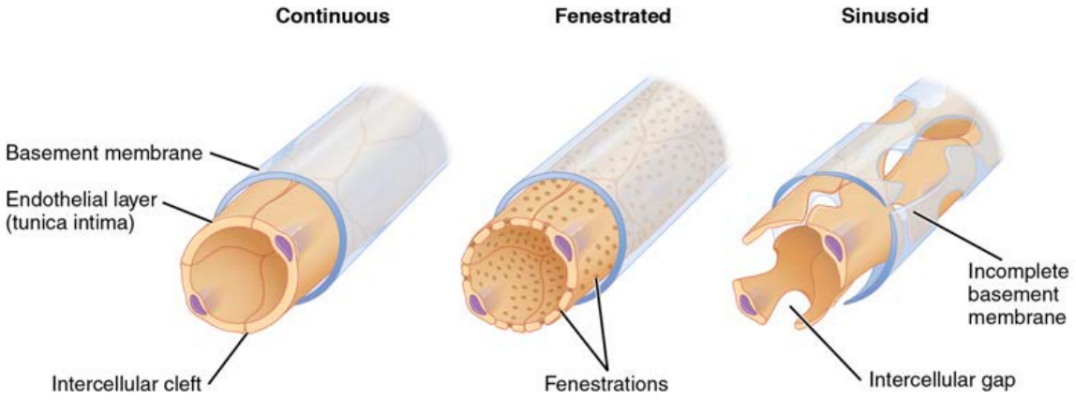

FIGURE 1.5: The three major types of capillaries: continuous, fenestrated, and sinusoid, picture from [36].

Sinusoid capillaries are flattened, and they have extensive intercellular interstices and incomplete basement membranes, in addition to intercellular clefts and pores. These very large openings allow the passage of larger molecules, including plasma proteins and even cells. Blood flow through the sinusoids is very slow, allowing more time for the exchange of gases, nutrients, and wastes. Sinusoids are found in the liver and spleen, bone marrow and many endocrine glands. For example, in the bone marrow, when a new RBC is formed, it must enter the blood and can only do so through the large openings of a sinusoidal capillary.

1.6.4 Venules and Veins

As the capillaries converge, venules are formed whose function is to collect deoxygenated blood and metabolic debris from the capillary networks. Venules consist of an endothelial tube supported by a small amount of collagenous tissue and, in larger venules, few smooth muscle fibers. Venules and capillaries are the primary sites in which white blood cells adhere to the endothelial lining of vessels and then squeeze through adjacent cells to enter the tissue fluid.
Multiple venules join to form veins, the vessels that conduct blood toward the heart. Because they are low-pressure vessels, the larger veins are usually equipped with valves that promote a unidirectional flow of blood to the heart and prevent backflow toward the capillaries caused by the inherent low blood pressure in the veins as well as gravity [36].

1.7 Conclusion

The function of blood is to supply oxygen, nutrients, and other substances to all of the body's tissues and organs, and to remove waste products. It is constituted by (i) plasma, a liquid made mostly of water and a mixture of dissolved proteins, ions, and metabolic molecules. (ii) white blood cells (leukocytes) which are the cells of the immune system that are involved in fighting infections and foreign bacteria, and viruses. (iii) platelets, which prevent blood loss from vessels in case of injuries by clumping and thereby initiating a blood clot. (iv) Red blood cells (RBCs), which are involved in oxygen and carbon dioxide transport between the lungs and tissues of the body. The latter constitute about 98% of blood, and consequently, have the most

significant influence on the mechanical proprieties of blood. An RBC is a highly flexible cell, made of a membrane surrounding a hemoglobin solution. The membrane is made of a fluid bilayer of phospholipids and contains different proteins, cholesterol, and various membrane-integrated proteins, distributed on it. Blood supplies oxygen, nutrients, and other substances through a circulatory system made of vessels of different sizes and properties.

Chapter 2

RBC Modelization

Content

2.1 Vesicles and Capsules . . . 17
2.2 Mechanical properties of membranes . . . 18
2.2.1 Equilibrium shapes . . . 18
2.2.2 Bending energy . . . 19
2.2.3 Elastic in-plane energy . . . 20
2.2.4 Area dilatation energy . . . 22
2.2.5 Membrane forces . . . 22
2.2.6 Membrane-membrane interaction . . . 24
2.3 The numerical methods . . . 24
2.3.1 Immersed Boundary method . . . 25
2.3.2 Element Boundary methods . . . 25
2.4 Hydrodynamic equations . . . 30
2.5 Conclusion . . . 32

The membrane of an RBC is a fluid bilayer of phospholipids, containing a network of proteins and transmembrane proteins (like ion channels). Due to this complexity, simplified systems like vesicles (made of a pure bilayer of phospholipids) and capsules (made of an extensible polymer shell) are used as models for RBCs. Both systems reproduce several features known for RBCs under flow. There are different types of vesicles and capsules classified by form, size, and type of production. In the following chapter, we shall review the mechanical properties of each model. The cell membrane can undergo in-plane and out-of-plane deformations. Constitute laws, like Helfrich or Skalak law, are used to model these deformations mathematically. The numerical procedures to solve fluid-structure interaction problems may be classified into two approaches: the monolithic approach and the partitioned approach. The monolithic approach treats the fluid and structure dynamics in the same mathematical framework to form a single system formulation for the entire problem, which is solved simultaneously by a unified algorithm. In contrast, the partitioned approach treats the fluid and the structure as two computational fields which can be solved separately with their respective mesh discretization and numerical algorithm. The interfacial conditions are used explicitly to communicate information between the fluid and structure solutions [55].

2.1 Vesicles and Capsules

Due to their similarity to living cells, vesicles and capsules have been extensively studied theoretically as well by experiments [56, 57], in order to understand and distinguish the characteristics of RBC mechanics that arise from the components of the cell membrane.
Lipid vesicles, or liposomes, are self-assembled lipid structures in the shape of a closed membrane consisting of a phospholipid bilayer. They can act as bio-mimetic compartments with a membrane that closely resembles that of living cells encapsulating materials such as proteins, drugs or other chemicals. They can be formed, manipulated, and modified in a variety of ways. Liposomes were first described in 1961 by Bangham [58]. In the following years a variety of macroscopic methods has been developed for their production, such as extrusion through porous membranes [59], electroformation [60], freeze-drying [61], hydration or swelling [62] to name a few of them. Vesicles may have a diameter ranging from a few nanometers to a few hundred micrometers classified as small unilamellar vesicles (SUVs), large unilamellar vesicles (LUVs), and giant unilamellar vesicles (GUVs) (Figure 2.1). Different type of phospholipid can be used to act on the stiffness of the membrane. Another important aspect of the membrane structure is its lamellarity, a term that defines the number of bilayers of which it is composed. Liposomes that contain more than one bilayer are called multilamellar vesicles (like MLVs). Another type of liposome called multivesicular vesicle consists of one giant vesicle containing several smaller vesicles (MVV). Giant unilamellar vesicles (GUVs) resemble to the living cells in their structure, functions, and geometry (such as membrane inextensibility of red blood cells), which is why they serve as a simplified system of RBC.

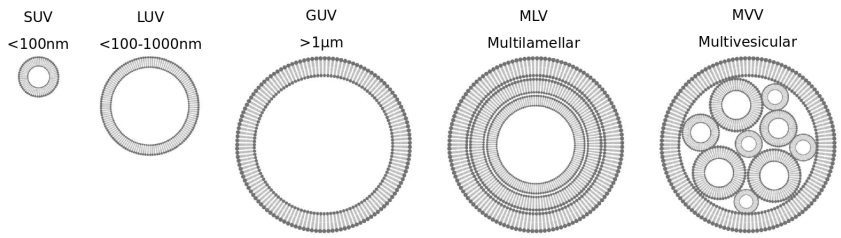

FIGURE 2.1: The common types of vesicle according to their size and lamellarity [63].

Capsules are found in nature in the form of cells, bacteria, seeds, and eggs. They consist of an internal substance enclosed by a semi-permeable membrane made of polymers. Depending on the fabrication process their membrane can be extensible, unlike vesicles. In turn they are endowed with shear elasticity, mimicking the cytoskeleton of the RBCs. The primary role of the capsule membrane is to confine and protect the encapsulated substance, as well as to control the exchange between the capsule's content and the ambient environment. The size of capsules can range from a few nanometers to a few hundred millimeters, where the later corresponds to a pharmaceutical capsule used for drug delivery. Artificial capsules are commonly used in cell sorting and cell characterization devices [27], determination of membrane properties [64], and of course to mimick blood flow in vascular capillaries [65, 13]. Several techniques based on physical and/or chemical methods are used in the fabrication process like air-suspension coating, pan coating, spray–drying, solvent evaporation or polymerization [66].

2.2 Mechanical properties of membranes

Theoretically, the membrane is considered as a two-dimensional impermeable and incompressible Newtonian fluid with a negligible mass due to its finite thickness. Four relevant energies contribution can be identified: (i) The local in-plane energy which is caused by the resistance to shear and dilation deformation. (ii) The local out-of-plane energy due to the bending deformation. (iii) The constraint energy for the total surface and volume conservation. (iv) The energy acting between pairs of membranes or membranes and walls, but are not part of the membrane model itself. It is assumed that the contribution of the energies mentioned above are independent of each other, which is a common idealization in simulations. Two approaches can be used to obtain a constitutive law for a two-dimensional membrane. In the first approach, the mathematical modeling of tensions and bending moments is an extrapolation of a three-dimensional elastic relation which relies on the classical theory of thin shells developed and widely used in structural engineering [67, 68]. Another approach is to postulate directly a two-dimensional constitutive law, which has been accomplished by different authors to describe biological membranes [18, 69]. The membrane model is formulated in such a way that any deviation from the resting shape increases the membrane energy and response forces are induced which drive the membrane shape towards an equilibrium shape [70].

2.2.1 Equilibrium shapes

The parameter controlling the shape in the absence of external flow is the reduced volume, also called the swelling ratio ν_{3D} [71]. It is defined as the ratio of the actual volume of the cell over that of a sphere having the same area. In two dimensions it is defined as the reduced area ν_{2D}, which is the surface area of the cell divided by the area of a circle having the same perimeter. This parameter quantifies the degree of deflation of a cell:

$$\nu_{3D} = \frac{V}{\frac{4}{3}\pi\left(\frac{A}{4\pi}\right)^{\frac{3}{2}}}, \tag{2.1}$$

$$\nu_{2D} = \frac{A}{\pi\left(\frac{p}{2\pi}\right)^{2}}, \tag{2.2}$$

where V is the volume, A the area, and p the perimeter. Equilibrium shapes in the absence of flow can be computed by the minimization of the total bending energy (while imposing constraints of constant enclosed volume and constant area [71]). The shapes are axisymmetric and can be conveniently represented via their section as a function of the reduced volume. This investigation of shapes for vesicles was proposed by Seifert [71] as shown in Figure 2.2. If we consider a sphere ($\nu = 1$) and deflate it progressively, we first find prolate shapes, which are elongated around the rotation axis. If we swell below $\nu \approx 0.65$, the minimal equilibrium shape is oblate, or discocyte. This kind of shape is the biconcave one assumed by RBCs. Below $\nu \approx 0.59$ there is a transition towards the stomatocyte, the cell folds on itself. It must be specified that in two dimensions there is no difference between prolates and oblates, and stomatocytes do not constitute a configuration of minimal energy.

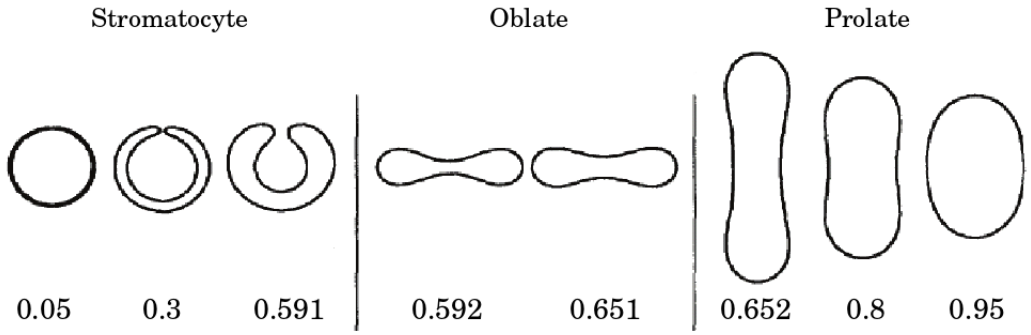

FIGURE 2.2: Different vesicle equilibrium shapes as a function of the reduced volume ν [71].

2.2.2 Bending energy

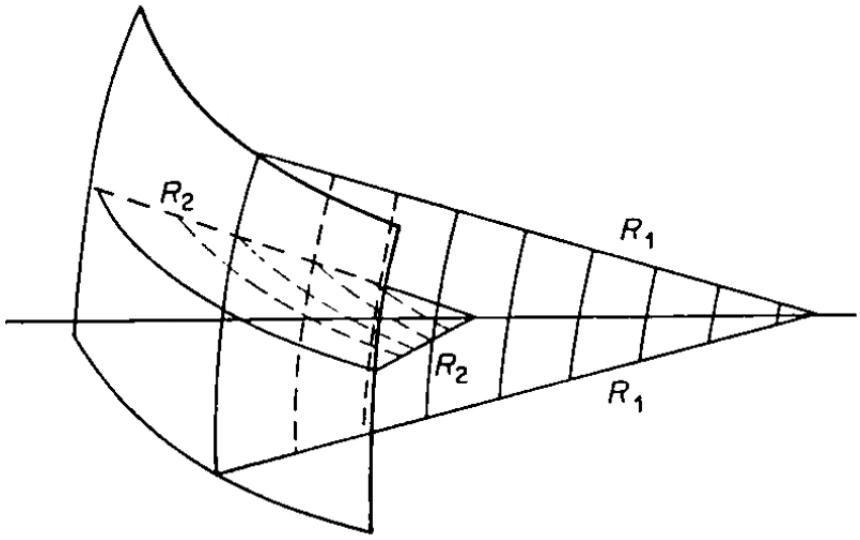

FIGURE 2.3: Section from the membrane curved in two planes [72].

The local bending energy expressed as a function of to the principal mean and Gaussian curvatures (2.3) was proposed first by Canham [72], and then generalized by Helfrich [15] for biological membranes.

$$W_B = \frac{K_B}{2} \oint_A (2H - C_0)^2 \, \mathrm{d}A + K_G \oint_A H_G \, \mathrm{d}A \,, \tag{2.3}$$

where the integration is performed over the instantaneous membrane shape.
C_0 is the spontaneous curvature, K_B is the bending modulus associated with the mean curvature H, and K_G is the bending modulus associated with the Gaussian curvature H_G. The mean and Gaussian curvatures are given by:

$$H = \frac{1}{2} \left(C_1 + C_2 \right) \tag{2.4}$$

$$H_G = C_1 \, C_2 \,, \tag{2.5}$$

C_1 and C_2 stand for the principal curvatures, which are defined as the inverse of the curvature radius $\left(C_i = R_i^{-1}\right)$ (Figure 2.3).
The concept of spontaneous curvature was introduced by Helfrich to account for possible asymmetries in the bilayer molecular structure of a biological membrane. In the case of symmetric membrane, $C_0 = 0$.
According to the Gauss-Bonnet theorem of differential geometry, the surface integral of the Gaussian curvature in equation (2.3) is a topological invariant. Since the present membrane model does not allow rupture or topology change, the Gaussian energy term is always constant and, thus, does not contribute to the energy balance. Hence, it can be neglected [73, 65].
Another non-local bending energy term may be included. It arises from the fact that the two layers of the RBC membrane do not interchange material readily. Therefore, they may have slightly different relaxed areas (due, for example, to a few additional molecules in one layer compared to the other) [73, 74]. The corresponding energy is defined as follows:

$$W_r = \frac{K_r}{2h^2 A_0} \left(\Delta A - \Delta A_0\right)^2 , \tag{2.6}$$

where K_r is the non-local bending modulus, and h is the distance between the neutral surfaces of the two layers. ΔA is the difference between the neutral surface area of the outer and the inner bilayer, which is defined as,

$$\Delta A = 2h \int_A H \ \mathrm{d}A \,, \tag{2.7}$$

ΔA_0 is the corresponding difference between the inner and outer unstressed area of these layers $\Delta A_0 = A_0^{out} - A_0^{in}$. This contribution is neglected in this work for the sake of simplicity.

2.2.3 Elastic in-plane energy

According to Evans and Skalak [75] the RBC membrane is considered as an isotropic, homogeneous, and hyperelastic continuous material. "Hyperelastic", also called Green elastic material, means that the elasticity is assumed to be non-dissipative. This implies that the membrane deformation is reversible. Since the energy is independent on the rotations or translations of the membrane (isotropic and homogeneous membrane), it is possible to align the undeformed and the deformed patches as shown in Figue 2.4.
The elastic energy is stored locally in a shear deformation and expansion of the membrane via the displacement gradient tensor $D_{i,j}$. This tensor describes the state of the local deformation of the membrane. Since the thickness is negligible, it is sufficient to treat the 2D case [70]. Here, the displacement gradient tensor is defined as:

$$D_{i,j} = \delta_{i,j} + \frac{\partial U_i}{\partial X_j} = \begin{pmatrix} 1 & 0 \\ 0 & 1 \end{pmatrix} + \begin{pmatrix} \partial_x U_x & \partial_y U_x \\ \partial_x U_y & \partial_y U_y \end{pmatrix} = \begin{pmatrix} D_{xx} & D_{xy} \\ D_{yx} & D_{yy} \end{pmatrix} \tag{2.8}$$

with:

$$\begin{cases} U_x = U_{1,1'}\vec{i} + U_{2,2'}\vec{i} + U_{3,3'}\vec{i}, \\ U_y = U_{1,1'}\vec{j} + U_{2,2'}\vec{j} + U_{3,3'}\vec{j}. \end{cases} \tag{2.9}$$

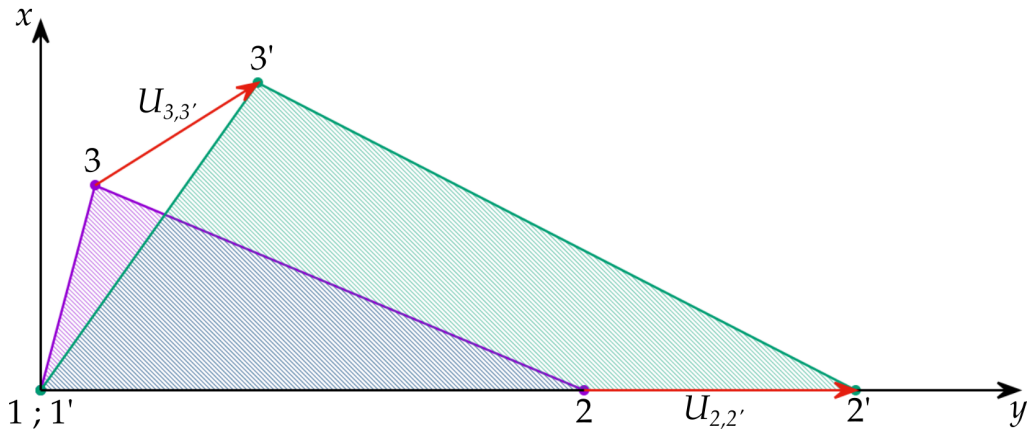

FIGURE 2.4: In-plane Deformation of a membrane face element. The undeformed face is defined by the vertices $(1,2,3)$, while the deformed one is defined with $(1',2',3')$. $U_{i,j}$ is the displacement vector from the undeformed to the deformed face.

The constitutive law for the elastic energy depends on the principal in-plane stretch ratios λ_1 and λ_2. These invariants are the eigenvalues of the displacement tensor $D_{i,j}$. Equivalently, the so-called strain invariants $I_1 = \lambda_1^2 + \lambda_2^2 - 2$ and $I_2 = \lambda_1^2\lambda_2^2 - 1$ which describe the strain and dilation state of the membrane, respectively, can be used. Several laws have been proposed to model thin membranes, but only the most used are presented here.
A classical 3D law, initially designed to describe rubber-like materials, and extrapolated with the thin shells theory is the Neo-Hookean (NH) law given in equation (2.10). Another simpler model relies on Hooke's law (H) (2.11). Both models (NH and H) are restricted to small deformations. To model the large deformations of RBCs membrane, Skalak introduced the Skalak law (SK) [18], which accounts for shear deformations and area dilatation (2.12).

$$w^{NH} = \frac{G_s}{2}\left(I_1 - 1 + \frac{1}{1+I_2}\right) \tag{2.10}$$

$$w^{H} = \frac{G_s}{4}\left(2(I_1 - I_2) + \frac{1}{1-\nu_s}I_1^2\right) \tag{2.11}$$

$$w^{SK} = \frac{G_s}{2}\left(2(I_1 - I_2) + I_1^2 + CI_2^2\right)\ , \tag{2.12}$$

where G_s denotes the surface shear modulus, ν_s is the surface Poisson ratio where $\nu_s \in \,]-1;1[$, and C is a positive dimensionless parameter preserving the area from large dilatation $C = \dfrac{\nu_s}{1+\nu_s}$.
The total elastic energy of the membrane is the surface integral : $W_s = \oint_A w^s \, \mathrm{d}A$ where w^s stands for the elastic energy law discussed above.

2.2.4 Area dilatation energy

In reality, the total surface area of an RBC is strongly conserved. To incorporate the constraints of fixed area (perimeter in 2D) it is convenient to introduce the Lagrangian multiplier ζ (2.13) which can be seen as a fluid-pressure difference that preserves locally the surface area [73]. The corresponding energy is written:

$$W_c = \oint_A \zeta \, \mathrm{d}A \,, \tag{2.13}$$

where $\mathrm{d}A$ is a surface element on the membrane surface A. Even for strongly deformed RBCs, the observed surface deviations are usually smaller than 1%.

2.2.5 Membrane forces

As the membrane is considered as a fluid (see section 2.2), we have to introduce the hydrodynamic equations and determine the membrane forces from membrane bending energy (2.3), and from the elastic (2.11, 2.10 or 2.12) and the constraint (2.13) energies, in order to get the vesicle or capsule motion in flow.
For a two-dimensinal planar membrane (one principal curvature) with zero spontaneous curvature, and negligible Gaussian energy (as previously discussed in section 2.2.2), the Helfrich bending energy (2.3) is written:

$$W_B = \frac{K_B}{2} \oint_A c^2 \, \mathrm{d}A \,. \tag{2.14}$$

The corresponding bending force is deduced from the functional derivative of this energy,

$$\mathbf{f}_B = -\frac{1}{\sqrt{g}} \frac{\delta W_B}{\delta \mathbf{r}}, \tag{2.15}$$

where $\delta\mathbf{r}$ is a small local displacement of a point $\mathbf{r}$ of the membrane, and g is the determinant of the metric tensor defining a fixed parametrization used to describe the membrane surface [76]. In two dimensions, it reads:

$$\mathbf{f}_B = K_B \left(\frac{\mathrm{d}^2 c}{\mathrm{d}l^2} + \frac{1}{2} c^3 \right) \mathbf{n} \,, \tag{2.16}$$

where $\mathbf{n}$ is the normal unit vector pointing outward at the considered position on the membrane, and $\mathrm{d}l$ the arc length (see [77] for calculation details).

For each constitutive elastic law, Biesel [78] derived, in the three-dimensional case, the tension components T_1 and T_2 respectively in the principal direction n_1 and n_2,

$$T_1^{NH} = \frac{G_s}{\lambda_1 \lambda_2} \left(\lambda_1^2 - \frac{1}{(\lambda_1 \lambda_2)^2} \right) \tag{2.17}$$

$$T_1^{H} = \frac{G_s}{(1-\nu_s)} \left[\lambda_1^2 - 1 + \nu_s \left(\lambda_2^2 - 1 \right) \right] \tag{2.18}$$

$$T_1^{SK} = \frac{G_s}{\lambda_1 \lambda_2} \left[\lambda_1^2 (\lambda_1^2 - 1) + C (\lambda_1 \lambda_2)^2 \left((\lambda_1 \lambda_2)^2 - 1 \right) \right] . \tag{2.19}$$

The principal stretch ratios λ_1 and λ_2 are measured along the principal deformation as the ratio between undeformed area by the deformed one, G_s is the shear modulus, ν_s is the Poisson ratio of the surface, and C a positive constant preserving the local membrane area from large deviation. The tension component T_2 in the second direction $\mathbf{n}_2$ is obtained by interchanging the indices 1 and 2 for each constitutive law.
For the 2D simulation, the cell is equivalent to an actual 3D cell subject to a stretching in direction 1 only: $T_1 \neq 0$, $T_2 = 0$. The stretch ratio λ_2 is not zero, but since $T_2 = 0$ we can express λ_2 in terms of λ_1 (e.g., for Neo-Hookean law $\lambda_2 = \lambda_1^{-\frac{1}{2}}$). Then for a 2D cell we have,

$$T^{NH} = \frac{G_s}{\lambda^{3/2}}\left(\lambda^3 - 1\right) \tag{2.20}$$

$$T^{H} = G_s(1+\nu_s)(\lambda^2 - 1) \tag{2.21}$$

$$T^{SK} = G_s\lambda_1(\lambda^2-1)\sqrt{\frac{1+C\lambda^2}{1+C\lambda^4}}\left[\frac{1+C\lambda^4}{1+C\lambda^2} + \frac{C}{1+C\lambda^4}\right], \tag{2.22}$$

where $T = T_1$ and $\lambda = \lambda_1$. For a membrane discretized by a set of points, T is the tension acting along a line segment connecting two adjacent points on the membrane, and $\lambda = \dfrac{\mathrm{d}l_0}{\mathrm{d}l_i}$ is the stretch ratio of the line segment. The membrane elastic force $\mathbf{f}_s$ at a point x of the membrane is then the resultant vector of the tensions in the two adjacent segments [16] (Figure. 2.5),

$$\mathbf{f}_s(x) = T_i\mathbf{t}_i - T_j\mathbf{t}_j\,. \tag{2.23}$$

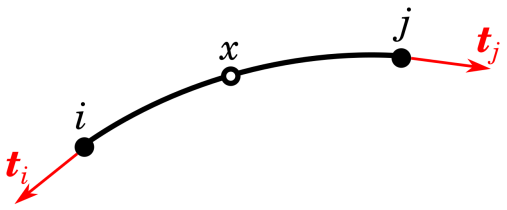

FIGURE 2.5: Illustration of the point x from the membrane with the two adjacent points i and j, with their corresponding unit tangent vectors $\mathbf{t}_i$ and $\mathbf{t}_j$ along them.

As discussed in section 2.2.4, a constraint must be introduced over the membrane surface to preserve the membrane from large deviations, for the 2D case, it reads,

$$\mathbf{f}_c = -\frac{1}{\sqrt{g}}\frac{\delta W_c}{\delta \mathbf{r}} = -\zeta c\mathbf{n} + \frac{\partial \zeta}{\partial l}\mathbf{t}\,. \tag{2.24}$$

The membrane force is then the summation of the bending, the elastic, and the constraint forces. In the capsule model the membrane can be extensible, unlike the vesicle model which shows a higher resistance to the shear elasticity. This difference is translated by considering only the constraint force for in-plane deformations for the vesicle model. For capsules, this constraint is already fulfilled in the Skalak model by the area dilatation constant C (Hooke and Neo-Hooke laws are not suited

for large deformations). Finally in the 2D case, the membrane forces for vesicle and capsule model reads,

$$\mathbf{f}_{mem}^{vesicle} = \mathbf{f}_B + \mathbf{f}_c = K_B \left(\frac{\mathrm{d}^2 c}{\mathrm{d}l^2} + \frac{1}{2} c^3 \right) \mathbf{n} - \zeta c \mathbf{n} + \frac{\partial \zeta}{\partial l} \mathbf{t} \tag{2.25}$$

$$\mathbf{f}_{mem}^{capsule} = \mathbf{f}_B + \mathbf{f}_s = K_B \left(\frac{\mathrm{d}^2 c}{\mathrm{d}l^2} + \frac{1}{2} c^3 \right) \mathbf{n} + T^m \, \mathbf{t}, \qquad (m = NH,\ H \text{ or } SK) \tag{2.26}$$

2.2.6 Membrane-membrane interaction

Between two closed lipid bilayers, there are different types of interaction forces that can be attractive, repulsive or both (oscillatory). In the absence of any other forces, unstressed bilayers attract each other via the Van der Waals force. This interaction has an effective range of at most 15 nm. Beyond this value, the effect becomes insignificant [79]. Due to the thermal agitation, the membrane fluctuates on different micro-states. This fluctuation is attenuated when two membranes are close enough, or equivalently their entropy becomes smaller, which leads to a repulsive force called entropic interaction. Another type of entropic interaction due to strongly bound water molecules on the membrane leads to an oscillatory steric-hydration force because of the energy needed to dehydrate these groups as the surfaces approach each other [80].
Other interaction that can be repulsive or oscillatory called depletion force. This interaction is associated with the macromolecules that are not attracted to or repelled from the membrane surface. Therefore, they are excluded from the area between the cells which induces an osmotic pressure between the bulk solution that contains macromolecules at a certain concentration and the depleted zone between the two surfaces that is free of macromolecules [81]. On the other hand, if the membrane adsorbs surrounding macromolecules, bridges shall be formed with the neighboring cell membrane, leading to the formation of an aggregate [82].
Another kind of force referred to as non-equilibrium (or non-conservative) force because they involve energy dissipation. They arise only as a reaction to motion or another force, like Hydrodynamic forces and viscous forces [83, 84, 85]. The interactions between biological cells are generally far more complex than can be described by just one or two types of interaction, especially if the cells have different sizes, topologies, and types (see [80]).

2.3 The numerical methods

In the approximation of small membrane deformations an analytical solution can be found [86, 87], but in the case of large deformations, a numerical simulation is necessary to solve the fully coupled equations governing the mechanics of the fluid and the membrane. Numerical methods for fluid-structure interaction are thus needed to predict the deformation of the membrane under flow conditions. At the small scale of the cells, inertial forces are negligible compared to viscous forces. Therefore, the blood flow is modeled using the Stokes equations. The load on the membrane is due to the normal and tangent components of pressure forces and viscous tractions. This problem has been studied over the last three decades and different techniques have been considered to derive numerical solutions. Many of these studies have

used a coupling strategy based on the boundary integral method to solve the Stokes flow and the equations of membrane elasticity on the same mesh [22, 88]. Another coupling method used for fluid-membrane interaction is the immersed boundary method [89, 90] where two grids are used, a stationary Eulerian grid for the fluid flow and a Lagrangian moving boundary for the interface. In this thesis, we used the Boundary integral method as a numerical method to solve the fluid-membrane interaction.

2.3.1 Immersed Boundary method

Another coupling method used for deformable particle simulation is the immersed boundary method. This method was initially developed by Peskin for the coupled simulation of blood flow and muscle contraction in a beating heart [19]. In contrast with the boundary integral method, two grids are used in this method, a stationary grid for the fluid flow and a moving boundary grid for the interface. The forces exerted by the membrane on the fluid and the flow velocity inducing membrane deformation are applied locally from one grid to the other using approximate Dirac functions [20]. The Navier-Stokes equations are generally solved using finite difference schemes [89, 98], or more recently using a lattice Boltzmann method [99, 70]. The immersed boundary method has the advantage over the boundary integral method to be applicable to non-zero Reynolds numbers and non-Newtonian fluids.

2.3.2 Element Boundary methods

Boundary Element Methods (BEM) are numerical computational methods which consist of transforming a partial differential equation (PDE), which holds over a given domain, into an integral equation over the boundary of this domain using the boundary integral method (BIM). BEM are applicable to problems for which Green's functions can be calculated, including fluid mechanics, acoustics, electromagnetics, fracture mechanics, and contact mechanics.
These methods have the advantage of reducing the geometric dimension of the problem by one, which largely decreases the total number of the meshing nodes. It also does not involve discretizing spatial derivatives (e.g., with finite element/volume methods) and is very accurate. In particular, it has been shown to be efficient, precise, and stable when modeling the deformation of vesicles or capsules subjected to flows [91, 92]. Considering the Stokes equation for an incompressible Newtonian fluid,

$$-\nabla p + \mu\, \nabla^2 \mathbf{u} + \mathbf{f} = \mathbf{0}\,, \tag{2.27}$$

$$\nabla \mathbf{u} = 0\,, \tag{2.28}$$

where $\mathbf{u}$ is the velocity of the fluid, p the pressure, $\mathbf{f}$ expresses the effect of an applied external body force, and μ the dynamic viscosity. Since the fluid is incompressible, the mass is conserved, which can be expressed by the continuity equation in (2.28).
Numerical solutions of the boundary integral equation for Stokes flow were first presented by Youngren and Acrivos [21] with reference to flow past a rigid particle. A growing body of literature on boundary integral equation methods for low Reynolds number flow has been established since that time [93, 94].

The boundary-integral representation of a two-dimensional Stokes flow is given by (see Appendix B for details),

$$u_j(\mathbf{r}_0) = -\frac{1}{4\pi\mu}\int_C G_{ij}(\mathbf{r},\mathbf{r}_0)\, f_i(\mathbf{r})\ \mathrm{d}l(\mathbf{r}) + \frac{1}{4\pi}\int_C^{PV} u_i(\mathbf{r}) T_{ijk}(\mathbf{r},\mathbf{r}_0) n_k(\mathbf{r})\ \mathrm{d}l(\mathbf{r})\,, \quad (2.29)$$

where $u_j(\mathbf{r}_0)$ is the velocity at a point $\mathbf{r}_0(x_0, y_0)$ lying inside a control area, due to a point force applied at the position $\mathbf{r}(x, y)$. $G_{ij}(\mathbf{r},\mathbf{r}_0)$ and $T_{ijk}(\mathbf{r},\mathbf{r}_0)$ are the Green's functions of Stokes flow representing, respectively, the velocity and stress field due to the point force $\mathbf{r}$, $f_j(\mathbf{r}) \equiv \sigma_{ij}\cdot n_k(\mathbf{r})$ is the traction force at the boundary C of a selected control area, l is the arc length along C. The superscript PV indicates that the integral is a principal value, and $n_k(\mathbf{r})$ is the unit normal vector pointing into the control area.

For three dimensional Stokes flow we obtain,

$$u_j(\mathbf{r}_0) = -\frac{1}{8\pi\mu}\int_A G_{ij}(\mathbf{r},\mathbf{r}_0)\, f_j(\mathbf{r})\ \mathrm{d}S(\mathbf{r}) + \frac{1}{8\pi}\int_A^{PV} u_i(\mathbf{r}) T_{ijk}(\mathbf{r},\mathbf{r}_0) n_k(\mathbf{r})\ \mathrm{d}S(\mathbf{r})\,, \quad (2.30)$$

where $u_j(\mathbf{r}_0)$ is the velocity at the point $\mathbf{r}_0(x_0, y_0, z_0)$ inside a control volume bounded by the surface A, and the unit normal vector $n_k(\mathbf{r})$ points inward.
The Boundary integral equation where $\mathbf{r}_0$ lies on the interface (e.g., closed membrane) can be deduced by combining the two BIM representations on either side of the interface. The boundary integral equation for Stokes flow in the presence of interfaces was presented by Pozrikidis [22, p.141]. For two-dimensional Stokes flow, we find (see Appendix C),

$$\begin{aligned} u_j(\mathbf{r}_0) = \frac{2}{1+\lambda}u_j^{\infty}(\mathbf{r}_0) \ - \ & \frac{1}{2\pi\mu_{ext}(1+\lambda)}\int_C G_{ij}(\mathbf{r},\mathbf{r}_0)\, f_j(\mathbf{r})\ \mathrm{d}l(\mathbf{r}) \\ & + \frac{1-\lambda}{2\pi(1+\lambda)}\int_C^{PV} u_i(\mathbf{r}) T_{ijk}(\mathbf{r},\mathbf{r}_0) n_k(\mathbf{r})\ \mathrm{d}l(\mathbf{r})\,, \end{aligned} \quad (2.31)$$

and for the three-dimensional case,

$$\begin{aligned} u_j(\mathbf{r}_0) = \frac{2}{1+\lambda}u_j^{\infty}(\mathbf{r}_0) \ - \ & \frac{1}{4\pi\mu_{ext}(1+\lambda)}\int_A G_{ij}(\mathbf{r},\mathbf{r}_0)\, f_j(\mathbf{r})\ \mathrm{d}S(\mathbf{r}) \\ & + \frac{1-\lambda}{4\pi(1+\lambda)}\int_A^{PV} u_i(\mathbf{r}) T_{ijk}(\mathbf{r},\mathbf{r}_0) n_k(\mathbf{r})\ \mathrm{d}S(\mathbf{r})\,, \end{aligned} \quad (2.32)$$

where $\lambda = \mu_{int}/\mu_{ext}$ is the viscosity ratio between the fluid inside and outside the interface, and $\mathbf{u}^{\infty}$ is the imposed flow.
In the case of unbounded flow, the so-called free-space Green's function for a two-dimensional flow are given by (see Appendix A),

$$G_{ij}(\mathbf{r},\mathbf{r}_0) = -\delta_{ij}\ln(|\mathbf{r}-\mathbf{r}_0|) + \frac{(r-r_0)_i(r-r_0)_j}{|\mathbf{r}-\mathbf{r}_0|^2}\,, \quad (2.33)$$

$$T_{ijk}(\mathbf{r},\mathbf{r}_0) = -4\,\frac{(r-r_0)_i(r-r_0)_j(r-r_0)_k}{|\mathbf{r}-\mathbf{r}_0|^4}\,. \quad (2.34)$$

For three-dimensional flow, the free-space Green's function are,

$$G_{ij}(\mathbf{r},\mathbf{r}_0) = \frac{\delta_{ij}}{|\mathbf{r}-\mathbf{r}_0|} + \frac{(r-r_0)_i(r-r_0)_j}{|\mathbf{r}-\mathbf{r}_0|^3}\,, \tag{2.35}$$

$$T_{ijk}(\mathbf{r},\mathbf{r}_0) = -6\,\frac{(r-r_0)_i(r-r_0)_j(r-r_0)_k}{|\mathbf{r}-\mathbf{r}_0|^5}\,. \tag{2.36}$$

$G_{ij}(\mathbf{r},\mathbf{r}_0)$ is also referred to as *stokeslet*, and $T_{ijk}(\mathbf{r},\mathbf{r}_0)$ as *stresslet*. The two tensors are also called the Oseen-Burgers tensors.

For a Stokes flow bounded by one infinite plane wall located at $y = W$, Blake [95] demonstrated that the Green's function can be constructed using the image system method from a stokeslet G_{ij}^{fs}, and a few image singularities, including a stokeslet equal in magnitude but opposite in sign to the initial stokeslet $-G_{ij}^{fs}$, a potential dipoles G_{ij}^{D}, and a stokeslet dipoles G_{ij}^{SD}, (2.37),

$$G_{ij}^{1W}(\mathbf{r},\mathbf{r}_0) = G_{ij}^{fs}(\mathbf{r}-\mathbf{r}_0) - G_{ij}^{fs}(\mathbf{r}-\mathbf{r}_0^{Im}) + 2h^2 G_{ij}^{D}(\mathbf{r}-\mathbf{r}_0^{Im}) - 2hG_{ij}^{SD}(\mathbf{r}-\mathbf{r}_0^{Im})\,, \tag{2.37}$$

where $h = y_0 - w$ is the distance of the point force from the wall and $\mathbf{r}_0^{Im} = (x_0, 2w - y_0)$ is the image of $\mathbf{r}_0$ with respect to wall (Figure 2.6).

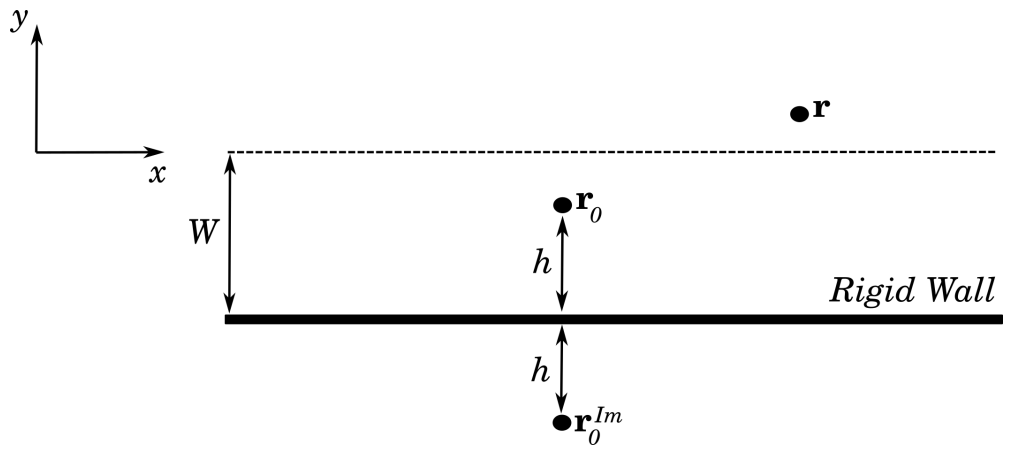

FIGURE 2.6: Illustration of a point force located at $\mathbf{r}_0$, above an infinite wall positioned at $y = W$. The point $\mathbf{r}_0^{Im}$ is the image of the point force with respect to the wall.

The potential and the stokeslet dipoles for the two-dimensional case are,

$$G_{ij}^{D}(\mathbf{r}) = \pm\left(\frac{\delta_{ij}}{\mathbf{r}^2} - 2\frac{r_i r_j}{\mathbf{r}^4}\right)\,, \tag{2.38}$$

$$G_{ij}^{SD}(\mathbf{r}) = r_y G_{ij}^{D}(\mathbf{r}) \pm \left(\frac{\delta_{jy}r_i - \delta_{iy}r_j}{\mathbf{r}^2}\right)\,, \tag{2.39}$$

where "+" stand for the *x-direction* and "−" for the *y-direction*. The associated stress tensor is given by,

$$T_{ijk}^{1W}(\mathbf{r},\mathbf{r}_0) = T_{ijk}^{fs}(\mathbf{r}-\mathbf{r}_0) - T_{ijk}^{fs}(\mathbf{r},\mathbf{r}_0^{Im}) + 2h^2 T_{ijk}^{D}(\mathbf{r},\mathbf{r}_0^{Im}) - 2hT_{ijk}^{SD}(\mathbf{r},\mathbf{r}_0^{Im})\,, \tag{2.40}$$

where,

$$T^D_{ijk}(\mathbf{r}) = \pm 4\left(-\frac{\delta_{ij}r_k + \delta_{ik}r_j + \delta_{jk}r_i}{|\mathbf{r}^4|} + 4\frac{r_i r_j r_k}{|\mathbf{r}^6|}\right), \tag{2.41}$$

$$T^{SD}_{ijk}(\mathbf{r}) = r_y T^D_{ijk}(\mathbf{r}) \pm 2\left(\frac{\delta_{jy}\delta_{ki}}{|\mathbf{r}^2|} - \frac{\delta_{jy}r_k r_i}{|\mathbf{r}^4|}\right) + \frac{2\delta_{ik}}{|\mathbf{r}|^4}\left(2r_x r_y, r_x^2 - r_y^2\right). \tag{2.42}$$

The Green's function for the case of a Stokes flow in a domain bounded by two parallel and rigid walls are the sum of a fundamental Green's function G^f_{ij} in (2.33), or (2.35) for 3D case, associated with the flow produced by the point force belonging to the domain, and its image system with respect to the two walls, and a complementary Green's function G^c_{ij} for which the associated flow field satisfies the boundary conditions on the walls. The imaging system is composed of two y-periodic sets of point force. For example, the first red point $\mathbf{r}_0^{Im}$ next to the lower wall is the reflection of the point force $\mathbf{r}_0$ by the lower wall, this first image will only cancel the contribution of the lower wall but will disturb the boundary condition in the upper wall, so that the reflection of the first image to the upper wall is to be considered, this reflection correction is $\mathbf{r}_1$, and so on (Figure. 2.7). The first green point $\mathbf{r}_{-1}^{Im}$ next to the upper wall is the reflection of the point force $\mathbf{r}_0$ by the upper wall, this image is then reflected by the lower wall and gives the image $\mathbf{r}_{-1}$.

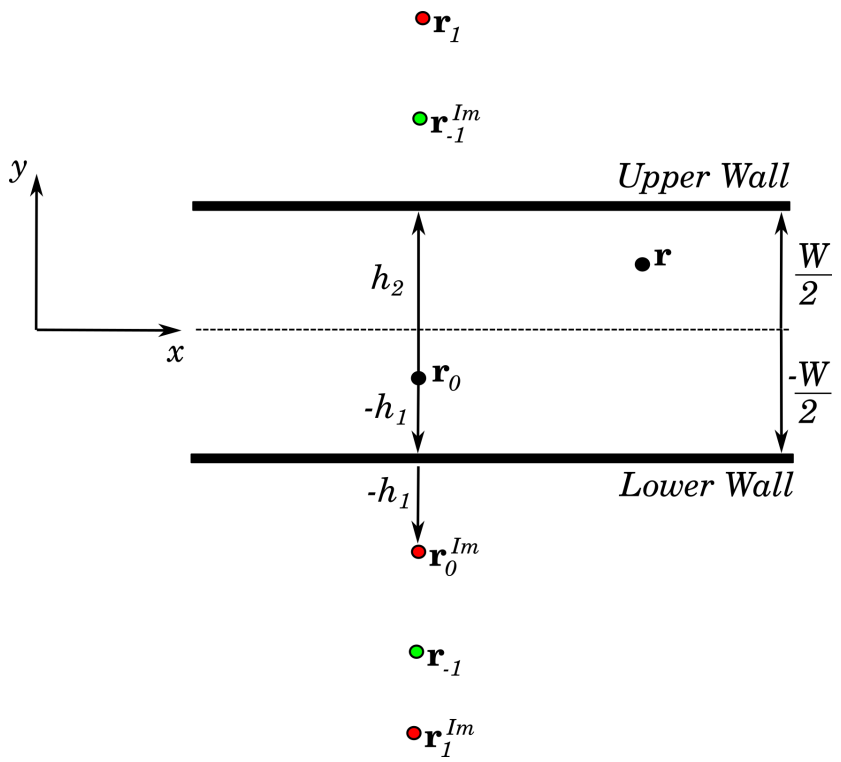

FIGURE 2.7: Illustration of a point force located at $\mathbf{r}_0$ bounded by two infinite wall positioned at $y = \pm W/2$, and it's images system $\mathbf{r}_n$ and $\mathbf{r}_n^{Im}$.

The fundamental component is the sum over all the stokeslet images N (2.43),

$$\begin{aligned} G_{ij}^{f}(\mathbf{r},\mathbf{r}_0) = &\sum_{n=-N}^{N}\left(-\delta_{ij}\ln(|\mathbf{r}-\mathbf{r}_n|)+\frac{(r-r_n)_i(r-r_n)_j}{|\mathbf{r}-\mathbf{r}_n|^2}\right) \\ &-\sum_{n=-N}^{N}\left(-\delta_{ij}\ln(|\mathbf{r}-\mathbf{r}_n^{Im}|)+\frac{(r-r_n^{Im})_i(r-r_n^{Im})_j}{|\mathbf{r}-\mathbf{r}_n^{Im}|^2}\right), \end{aligned} \tag{2.43}$$

where $\mathbf{r}_n = (x_0, y_0 + 2Wn)$ and $\mathbf{r}_n^{Im} = (x_0, -y_0 - W + 2Wn)$. The first term in the right-hand-side of (2.43) is the sum of the point force itself, and the second term is the sum of the image of the point force with respect to the walls. The force magnitude of the image point in the second term is equal to the point force in the first term, but with opposite direction.

As N tends to infinity, both sums in (2.43) diverge. To normalize (2.43) we use the summation formula proposed by Lamb [96, p.71],

$$\sum_{-\infty}^{\infty}\ln(\mathbf{r}) = \frac{1}{2}\ln\left(\cosh(r_y)-\cos(r_x)\right)+\frac{1}{2}\ln(2), \tag{2.44}$$

where the term $\frac{1}{2}\ln(2)$ was added so the Green's function close to the source point reduces to a stokeslet [22, p.94].

The fundamental Green's function is then,

$$G_{ij}^{f}(\mathbf{r},\mathbf{r}_0) = Q_{ij}(\mathbf{r}-\mathbf{r}_0) - Q_{ij}(\mathbf{r}-\mathbf{r}_0^{Im}), \tag{2.45}$$

where,

$$Q_{ij}(\mathbf{r}) = \begin{cases} Q_{xx} = -\frac{1}{2}\ln\left[\cosh\left(\frac{x\pi}{W}\right)-\cos\left(\frac{y\pi}{W}\right)\right]+\frac{x\pi}{2W}\frac{\sinh\left(\frac{x\pi}{W}\right)}{\cosh\left(\frac{x\pi}{W}\right)-\cos\left(\frac{y\pi}{W}\right)}, \\ Q_{xy} = Q_{yx} = \frac{x\pi}{2W}\frac{\sinh\left(\frac{y\pi}{W}\right)}{\cosh\left(\frac{x\pi}{W}\right)-\cos\left(\frac{y\pi}{W}\right)}, \\ Q_{yy} = -\frac{1}{2}\ln\left[\cosh\left(\frac{x\pi}{W}\right)-\cos\left(\frac{y\pi}{W}\right)\right]-\frac{x\pi}{2W}\frac{\sinh\left(\frac{x\pi}{W}\right)}{\cosh\left(\frac{x\pi}{W}\right)-\cos\left(\frac{y\pi}{W}\right)}. \end{cases} \tag{2.46}$$

Evaluating $G^f_{ij}(r, r_0)$ at the two walls we find,

$$
\begin{aligned}
&G^f_{xx}(y = \pm W/2) = G^f_{yy}(y = \pm W/2) = 0\,,\\
&G^f_{xy}(y = +W/2) = G^f_{yx}(y = +W/2) = \frac{(x - x_0)\pi}{W}\,\frac{\sinh\left(\frac{h_2\pi}{W}\right)}{\cosh\left(\frac{(x - x_0)\pi}{W}\right) - \cos\left(\frac{h_2\pi}{W}\right)},\\
&G^f_{xy}(y = -W/2) = G^f_{yx}(y = -W/2) = -\frac{(x - x_0)\pi}{W}\,\frac{\sinh\left(\frac{h_1\pi}{W}\right)}{\cosh\left(\frac{(x - x_0)\pi}{W}\right) - \cos\left(\frac{h_1\pi}{W}\right)},
\end{aligned}
\tag{2.47}
$$

where $h_1 = y_0 + \frac{W}{2}$ and $h_2 = \frac{W}{2} - y_0$ (Figure. 2.7). From (2.47) it is obvious that only the diagonal terms of G^f_{ij} vanish over each wall. We require then a complementary Green tensor G^c_{ij} which must satisfy the following boundary conditions,

$$
\begin{aligned}
&G^c_{xx}(y = \pm W/2) = G^c_{yy}(y = \pm W/2) = 0\,,\\
&G^c_{xy}(y = +W/2) = G^c_{yx}(y = +W/2) = -G^f_{xy}(y = +W/2)\,,\\
&G^c_{xy}(y = -W/2) = G^c_{yx}(y = -W/2) = -G^f_{xy}(y = -W/2)\,.
\end{aligned}
\tag{2.48}
$$

The complementary term is calculated using Fourier transforms. First, one takes the Fourier transform of the Stokes equation with the boundary conditions (2.48). Then, by an inverse Fourier transform the complementary Green's tensor G^c_{ij} is determined in real space and added to the fundamental Green's tensor G^f_{ij} in order to obtain the full Green's tensor G^{2w}_{ij}. The same approach is also used for the stresslet T^{2w}_{ijk}. The full analytical calculations of the Green's function can be found in [22, p.98] for the 2D case. The calculations for the 3D case was done by Liron and Mochon [97].
In our simulation (see Chapter 3) the complementary Green's tensor is evaluated numerically by fast Fourier transform subroutines.

2.4 Hydrodynamic equations

The velocity and the hydrodynamic pressure fields due to a point force in the membrane are found by solving the continuity equation (2.28), and the Stokes equation (2.27) with the forcing term replaced by a singular forcing term in the two-dimensional case,

$$
-\nabla p + \mu\,\nabla^2\mathbf{u} = -\mathbf{f}\,\delta(\mathbf{r} - \mathbf{r}_0)\,,
\tag{2.49}
$$

where $\mathbf{u}$ is the velocity of the fluid, p the pressure, and μ the dynamic viscosity. $\delta(\mathbf{r} - \mathbf{r}_0)$ represents the Dirac delta function imposing that the force $\mathbf{f}$ vanishes everywhere except at the singular point $\mathbf{r} = \mathbf{r}_0$. First, we write all the variables in right-hand side of (2.49) in a dimensionless form using,

$$\mathbf{r}^* = \frac{\mathbf{r}}{R_0} \quad ; \quad \mathbf{u}^* = \frac{\mathbf{u}}{U} \quad ; \quad p^* = \frac{pR_0}{\mu U}\,, \tag{2.50}$$

where the cell radius R_0 is the characteristic length scale and U is the characteristic velocity. Substituting the terms in (2.50) in the Stokes equation (2.49) and multiplying it by the quantity $\left(\frac{R_0^2}{\mu U}\right)$ we obtain,

$$-\nabla^* p^* + \nabla^{*2}\,\mathbf{u}^* = -\left(\frac{R_0^2}{\mu U}\right)\mathbf{f}\,\delta(\mathbf{r}-\mathbf{r}_0)\,. \tag{2.51}$$

Now we write the membrane forces for the vesicle or the capsule model (2.25, 2.26), and the Dirac delta function in dimensionless form using,

$$c^* = cR_0 \quad ; \quad l^* = \frac{l}{R_0} \quad ; \quad \zeta^* = \frac{\zeta}{\Gamma} \quad ; \quad \delta(\mathbf{r}-\mathbf{r}_0) = \delta\left(R_0(\mathbf{r}^*-\mathbf{r}_0^*)\right) = \frac{\delta(\mathbf{r}^*-\mathbf{r}_0^*)}{R_0}\,,^{1} \tag{2.52}$$

where Γ is the spring constant of the membrane. Introducing the shear rate with $\dot{\gamma} = \frac{U}{R_0}$, the dimensionless membrane forces for the vesicle model reads,

$$\begin{aligned}\frac{R_0}{\mu\dot{\gamma}}\,\mathbf{f}^*_{mem} =& \frac{K_B}{\mu\dot{\gamma}R_0^3}\left(\frac{\mathrm{d}^2c^*}{\mathrm{d}l^{*2}} + \frac{1}{2}\,c^{*3}\right)\delta(\mathbf{r}^*-\mathbf{r}_0^*)\mathbf{n} \\ &+ \frac{\Gamma}{\mu\dot{\gamma}R_0}\left(\frac{\partial\zeta^*}{\partial l^*}\mathbf{t} - \zeta^* c^*\mathbf{n}\right)\delta(\mathbf{r}^*-\mathbf{r}_0^*)\,.\end{aligned} \tag{2.53}$$

We introduce the following dimensionless number,

- The capillary number :

$$C_a = \frac{\mu\dot{\gamma}R_0^3}{K_B} \equiv \dot{\gamma}\tau_B\,, \tag{2.54}$$

  it measures the flow strength over the bending energy of the membrane. It also gives the ratio between the shear time $\dot{\gamma}^{-1}$ and the characteristic time in bending modes needed by a deformed vesicle to relax to its equilibrium shape $\frac{\mu R_0^3}{K_B}$.

- The tension number :

$$C_T = \frac{\mu\dot{\gamma}R_0}{\Gamma}\,, \tag{2.55}$$

  is the ratio between the spring relaxation time and the shear time.

[1] Using Dirac delta property: $\delta(ax) = \frac{1}{|a|}\delta(x)$

- For the capsule model, the dimensionless shear rate related to the shear force determines the relative importance of shearing and elasticity. It reads,

$$C_s = \frac{\mu \dot{\gamma} R_0}{G_s} \equiv \dot{\gamma} \tau_s \,. \tag{2.56}$$

- Another important parameter is the reduced ratio of bending to elasticity modulus, in the form of,

$$C_e = \frac{K_B}{G_s R_0^2} \,. \tag{2.57}$$

- For the flow confined between two parallel walls, the dimensional number C_n describes the degree of confinement of the cell. It reads,

$$C_n = \frac{2R_0}{W} \,. \tag{2.58}$$

2.5 Conclusion

Due to the complexity of the RBC membranes, simplified models like capsules, and vesicles are used to mimic RBC behaviors both in simulations and in experiments. The main difference between these two models is their extensibility. The capsules membrane, depending on the fabrication process, can be extensible unlike the vesicles. The membrane model is formulated in such a way that any deviation from the resting shape increases the membrane energy and response forces are induced which drive the membrane towards an equilibrium shape. In simulations, the unstressed shape is controlled with the reduced volume (reduced area for the two-dimensional case), also called swelling ratio. This parameter quantifies the degree of deflation of a cell. In the absence of externally applied flow, RBCs assumes a discocyte shape, where the swell ratio is around $\nu = 0.65$ (see Figure 2.2). In the presence of external flow, four relevant response forces contributions can be identified: Local in-plane forces are caused by the resistance to shear and dilation. The bending energy, giving rise to forces normal to the membrane. To ensure that the total surface and volume are constant, like for RBCs, we impose a constraint force. Furthermore, the forces that act between pairs of membranes or membranes and walls, but are not part of the membrane model itself. Constitutive laws are adopted for the bending and the stretching energies. Helfrich law (2.3) is used for the bending energy, both for the vesicle and the capsule model. For small in-plane deformation, in the capsule model, Hooke and Neo-Hooke laws are used for the stretching energy, to model the large deformations of RBC membranes, Skalak law (2.12) is used. It accounts for shear deformation and area dilatation.
Two approaches can be used as numerical procedures to solve fluid-membrane interaction problems. In the first one, the fluid and the membrane dynamics are brought together into a single formulation for the entire problem. This resulting equation can be calculated using the Boundary integral method, where the partial differential equation is transformed into an integral equation over the boundary of the domain using Green's function and the Lorentz reciprocal theorem (see Appendix B). The Green's function differs from one geometry to another (e.g.: unbounded flow, flow bounded by one or two walls, coaxial-cylinders, etc.). The imaging system method [95] is generally used to find the right Green's function associated with each geometry. In contrast, the second approach consists of two separated grids, a stationary

grid for the fluid flow and a moving boundary grid for the interface. The interaction between the fluid and the membrane grids is calculated using an approximated Dirac delta function. This approach is called the immersed boundary method.
Using dimensional analysis for the Stokes equation, and the membrane forces equation, the system of equations can be described with dimensionless quantities. The capillary number C_a, and the tension number C_T are used for the vesicle model. The dimensionless shear rate C_s, and the reduced ratio of bending C_e for the capsule model. Another dimensionless parameter used in the case of a cell confined between two walls is the confinement number C_n.

Chapter 3

Cells under flow

Content

3.1 Algorithm . . . 35
3.2 Single cells in shear flow . . . 37
3.2.1 Vesicles under shear flow . . . 37
3.2.2 Capsules under shear flow . . . 38
3.3 Vesicles in Poiseuille flow . . . 41
3.3.1 Steady shapes . . . 42
3.3.2 The snaking shape . . . 45
3.4 Vesicles in modulated Poiseuille flow . . . 49
3.4.1 Steady shapes . . . 51
3.4.2 The snaking shape . . . 53
3.5 Two vesicles in Poiseuille flow . . . 60
3.6 Conclusion . . . 64

In this chapter, we will study the shape of two-dimensional cells, for unconfined shear flow, and confined Poiseuille flow. The simulations are done with the boundary integral method, a diagram of the algorithm is shown in Figure 3.4. First, we start by a comparison between the capsule and vesicle deformation, and the observed shapes for different viscosity ratio λ in shear flow. Then, for the Poiseuille flow, we will focus only on the vesicle model for a viscosity ratio λ set equal one. We will study and summarize as a function of the capillary number C_a and the confinement C_n the vesicle shapes in a phase diagram. We will extend the discussion to time-dependent flows using amplitude modulation of the Poiseuille flow and investigating its effect on the vesicles shape. We focus on the emerging snaking shape, where the vesicle shows an oscillatory motion like a swimmer flagella even though the flow is stationary. In all simulations, we have set the reduced area v to 0.6 which is close to the one of an RBC in 2D. We will also extend the study to the case of two vesicles in steady and oscillating Poiseuille flow.

3.1 Algorithm

The vesicle membrane is discretized with a set number of nodes N. At a certain time t each node $\mathbf{r}_i(t)$ is defined by its x and y coordinates Figure 3.1.

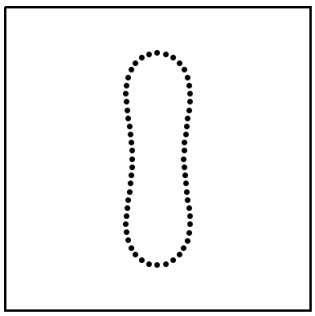

FIGURE 3.1: Vesicle membrane nodes r_i at a certain time t.

The numerical procedure begins by calculating the local curvature using the tangent and normal unit vectors. Then using equation (2.25) for vesicle model or (2.26) for capsules, the force vectors $\mathbf{f}_i(t)$ are generated on each node $\mathbf{r}_i(t)$ Figure 3.2.

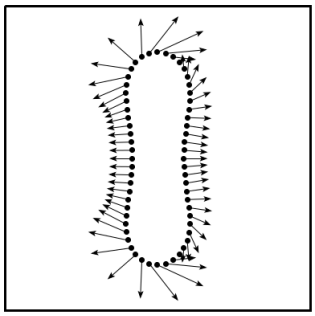

FIGURE 3.2: Force vectors $\mathbf{f}_i$ calculated from (2.25) in each membrane node $\mathbf{r}_i$.

Applying an external flow $\mathbf{u}^\infty$, the membrane will deform and move with a certain velocity. The velocity vectors $\mathbf{u}_i(\mathbf{r}_i(t))$ on each node, Figure 3.3, are obtained by solving the equation (2.29) with the appropriate Green's functions.

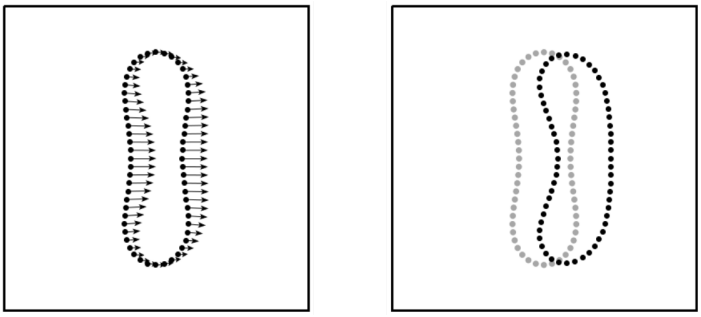

FIGURE 3.3: The figure in the left shows the velocity vectors $\mathbf{u}_i(\mathbf{r}_i)$ calculated using BIM formulation in (2.29) on each nodes. In the right figure, the new shape and position of the membrane $\mathbf{r}_i(t + \mathrm{d}t)$ are obtained with Euler integration.

Finally the new membrane shape and position are obtained by a numerical integration of the velocity vectors with Euler method $\mathbf{r}(t+dt) = \mathbf{r}(t) + \mathbf{u}(\mathbf{r}(t), t)$. Figure 3.4 shows the algorithm scheme used for the BIM method.
The combination between the BIM method and the vesicle model was initially developed by Biben and Misbah [100]. Many studies used the same approach to study vesicle behaviors in flow like [87, 101]. The numerical approach was also extended to study 3D vesicle dynamics [102].

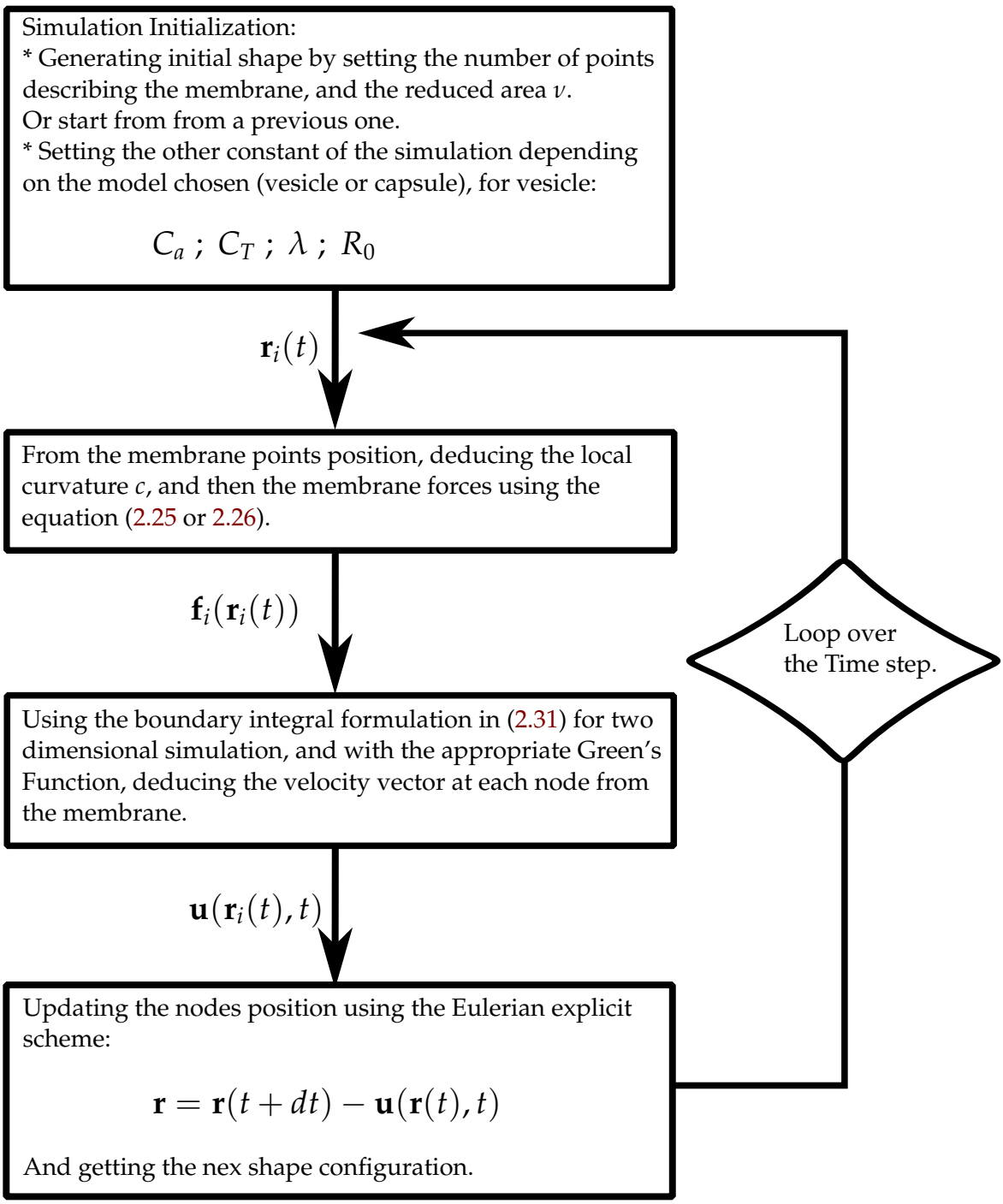

FIGURE 3.4: Illustration of the algorithm used for two-dimensional simulation with the boundary integral method.

3.2 Single cells in shear flow

Considering the Stokes equation (2.27) without external force ($\mathbf{f} = 0$), we are looking for the flow profile $\mathbf{u}(u_x(y), 0)$ between a lower plane wall at $y = {}^{-W}/_{2}$ moving parallel to itself with a constant velocity $-\mathbf{V}_0$, and an upper plane wall also moving in parallel with the constant velocity $\mathbf{V}_0$, as shown in Figure 3.5. It is assumed that no external pressure gradient is applied parallel to the walls, and the flow is fully developed, the Stokes equation is then,

$$\mu \frac{\mathrm{d}^2 u_x}{\mathrm{d}y^2} = 0\,. \tag{3.1}$$

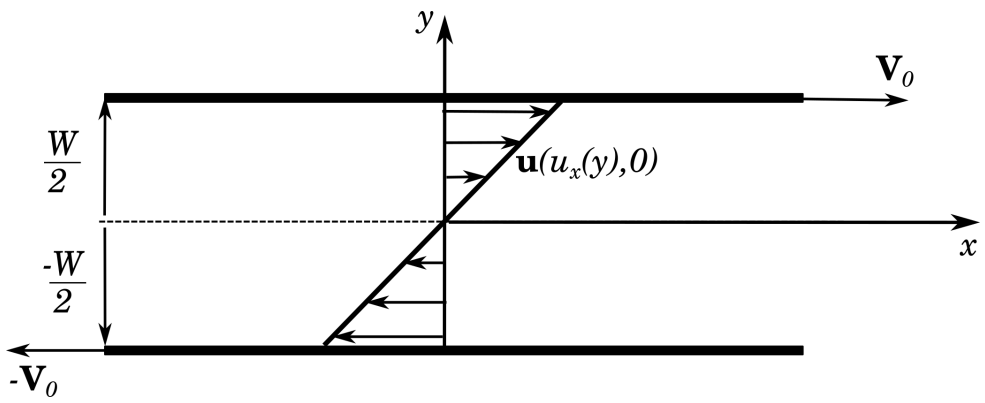

FIGURE 3.5: Shear flow illustration, the upper and lower wall are moving respectively with the constant velocity $\mathbf{V}_0$ and $-\mathbf{V}_0$.

Integrating equation (3.1) from $y = {}^{-W}/_{2}$ to $y = {}^{W}/_{2}$, and taking into account the boundary condition at the upper wall $(u_x(y = {}^{W}/_{2}) = V_0)$ and at the lower one $(u_x(y = {}^{-W}/_{2}) = -V_0)$, the velocity profile for a shear flow is then,

$$\mathbf{u}(x, y) = \begin{cases} u_x = 2V_0 \dfrac{y}{W} \\ \\ u_y = 0 \end{cases} . \tag{3.2}$$

The behavior of a cell in shear flow is used here as a test case. The objective is to compare the deformation and the motion in vesicle and capsule model with the literature.

3.2.1 Vesicles under shear flow

We consider a two-dimensional vesicle immersed in an unbounded shear flow. The membrane forces are computed using the equation (2.25). The Stokes equation is solved for each point of the membrane using (2.31) and the associated free space Green's functions (2.33, 2.34).
The flow is unbounded, means that W tends to infinity and consequently the confinement effect vanishes $C_n = 0$. Therefore, only the Capillary number C_a and the viscosity ratio λ come into play.
If the viscosities of the liquid inside and outside of the vesicle are equal, the vesicle shows a dynamic state called tank-treading (TT), this motion is due to the elongation part of the shear flow in which the vesicle becomes oriented within the shear

plane, but with a constant inclination angle θ_0 to the flow direction, as shown in Figure. 3.6. The rotational part of the shear flow induces a rotational flow of the interior liquid, which implies a rotation of the membrane around the vesicle interior. As the viscosity contrast increases, the vesicle shows a bifurcation to a different type of motion called tumbling (TB), See Figure. 3.6. Here, the vesicle rotates periodically in the shear plane, instead of only its membrane. At higher shear rates, An intermediate regime between TT and TB emerges. Called the vacillating-breathing (VB) (also named trembling or swinging) founded theoretically by Misbah [87]. In this state, the long axis of the vesicle does not perform full rotations as in the TB mode, but only oscillates up and down about the flow direction.
A phase diagram summarizing vesicle shapes were made numerically [103], analytically [29, 104], and also by in-vitro experiments [105]. Generally, the transition from TT to TB trough VB is done by an increase of the viscosity ratio and a decreasing of the capillary number C_a.

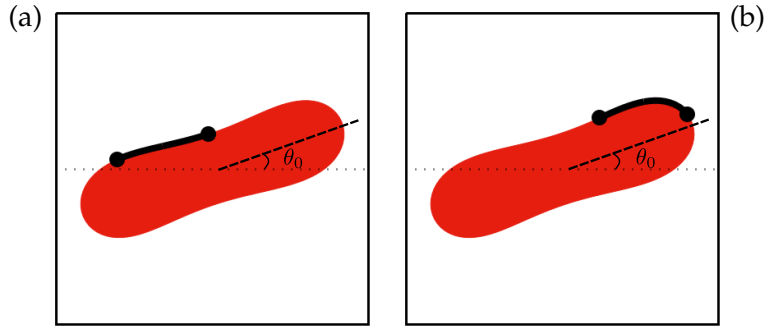

FIGURE 3.6: Tank-treading motion of a vesicle in shear flow for $C_a = 1$, $\lambda = 1$. ⬬ is a portion of the membrane. (a) and (b) shows the displacement of a portion from the membrane.

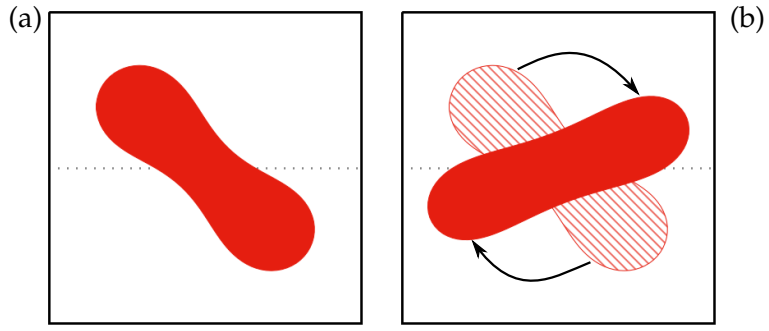

FIGURE 3.7: (a) and (b) shows the tumbling motion of a vesicle in shear flow for $C_a = 1$ and $\lambda = 5$.

3.2.2 Capsules under shear flow

In this section, we study the motion of a two-dimensional capsule with an initial circular shape under shear flow. The Skalak law is employed for the in-plane deformation due to its similarity with RBC, and the Helfrich law for the out of plane deformation. Due to the shear flow, the capsule deforms and rotates about its stationary origin. Besides the TT, TB and VB motions previously discussed for the vesicle model, the in-plane elasticity of the capsule membrane introduces two main new

effects: (i) if there is no viscosity contrast, under a weak enough flow the capsule undergoes TB, where a vesicle always exhibit a TT. (ii) A swinging (SW) or oscillatory motion at a low viscosity contrast emerges. In this mode, the inclination angle oscillates but always remains positive (not to be confused with VB, where the inclination angle oscillation is quite large).
The capsule deformation is captured within the deformation parameter D (also referred to as the Taylor parameter or elongation parameter),

$$D = \frac{L - B}{L + B}, \tag{3.3}$$

where L and B are respectively the largest and smallest axis of the deformed capsule, as shown in Figure 3.8 (for a circle $D = 0$).

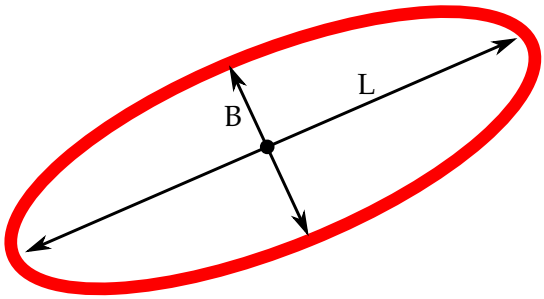

FIGURE 3.8: The elliptic shape adopted by a capsule in shear flow. L and B are the largest and smallest axis of the deformed capsule.

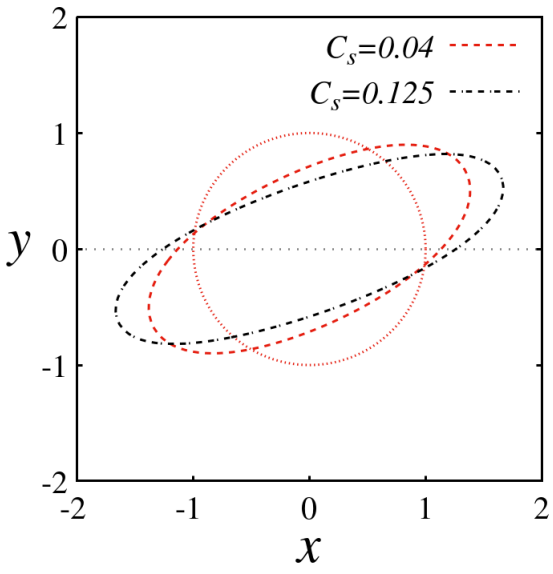

FIGURE 3.9: Deformed capsule with a circular initial shape for the dimensionless shear rates $C_s = 0.04$ and $C_s = 0.125$

Figure 3.9 shows the deformed capsule for the dimensionless shear rate ($C_s = 0.04$ and 0.125), the viscosity ratio $\lambda = 1$, and without bending stiffness effect $C_e = 0$. The capsule elongates and aligns itself with the direction of the flow as the C_s increases. After the capsule deforms to a steady configuration, its membrane undergoes a TT

motion. A slight increase in the perimeter accompanies the elongation. To quantitatively illustrate the effect of increasing the dimensionless shear rate C_s on the capsule deformation, the temporal evolution of the Taylor deformation parameter D is presented in Figure 3.10.

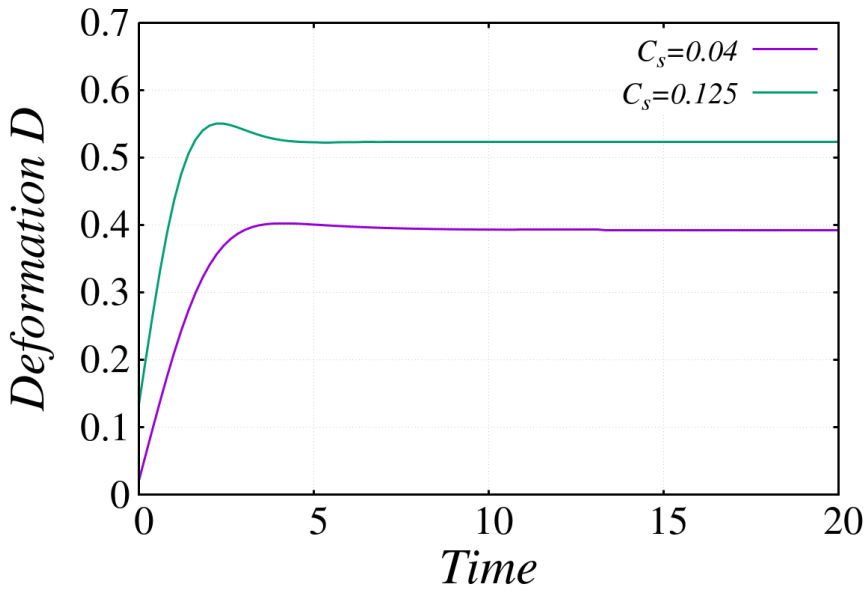

FIGURE 3.10: Temporal evolution of Taylor deformation of a capsule for $C_s = 0.04$ and $C_s = 0.125$, without bending stiffness effect ($C_e = 0$)

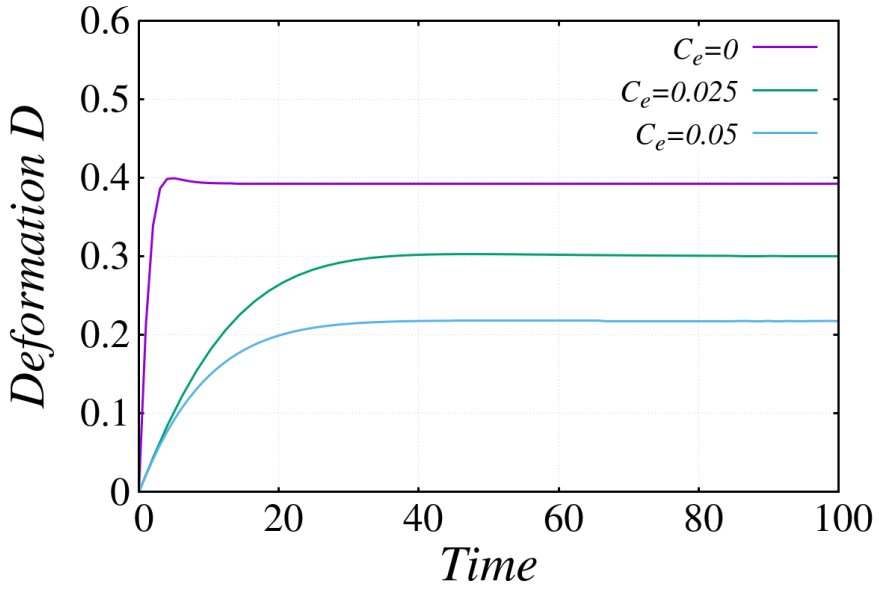

FIGURE 3.11: Temporal evolution of Taylor deformation of a capsule for a fixed dimensionless shear rate $C_s = 0.04$, and different bending ratio C_e

In Figure 3.11, and for a fixed dimensionless shear rate $C_s = 0.04$ the effect of the bending stiffness is reported. It restricts the global deformation of capsules. Increasing the bending modulus C_e, the shape of the deformed capsules tends to a circle,

and the orientation becomes less aligned with the flow direction. These results agree with those of previous researchers, e.g., Ramanujan and Pozrikidis [88], and Bagchi [16].

3.3 Vesicles in Poiseuille flow

In this section, we treat the flow of an incompressible fluid between two parallel and fixed walls. The flow is induced by a pressure difference applied between the inlet and outlet of the channel. The two walls are at $y = -W/2$ and $y = W/2$. The pressure gradient varies negatively in the direction of the x axis $\partial p/\partial x = -\Delta p/L$. Assuming that no external forces are applied, the Stokes equation is

$$\begin{cases} \dfrac{-\partial p}{\partial x} + \mu \dfrac{\partial^2 u_x}{\partial y^2} = \dfrac{\Delta p}{L} + \mu \dfrac{\partial^2 u_x}{\partial y^2} = 0 \\ \dfrac{-\partial p}{\partial y} = 0 \end{cases} . \tag{3.4}$$

Integrating this equation, and taking into account the no-slip boundary conditions on the walls of the channel ($u_x = 0$ for $y = \pm W/2$), we find:

$$\mathbf{u}(x,y) = \begin{cases} u_x = \dfrac{\Delta p}{2\mu L}\left(-y^2 + \dfrac{W^2}{4}\right) = V_{max}\left(1 - \dfrac{4y^2}{W^2}\right) \\ u_y = 0 \end{cases} . \tag{3.5}$$

The corresponding flow is referred to as the plane Poiseuille flow. Its velocity profile is parabolic as shown in Figure 3.12, and the velocity u_x has its maximum value V_{max} in the plane of symmetry of the channel ($y = 0$) with:

$$V_{max} = \frac{\Delta p}{L}\frac{W^2}{8\mu} = \left(-\frac{\partial p}{\partial x}\right)\frac{W^2}{8\mu} . \tag{3.6}$$

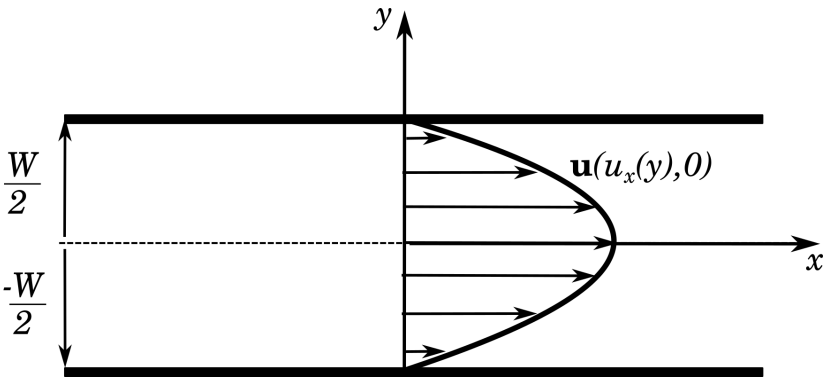

FIGURE 3.12: Poiseuille flow illustration, the velocity vanishes at the upper and lower wall and becomes maximal in the middle of the channel at $y = 0$.

The volumetric flow rate Q per unit of the channel width is given by,

$$Q = \int_{-W/2}^{W/2} u_x(y)\,\mathrm{d}y = \frac{\Delta p}{L}\frac{W^3}{12\mu} . \tag{3.7}$$

The flow rate Q is proportional to W^3 for a given pressure difference. Therefore, it decreases drastically as the width decreases. The viscosity forces, which increases with the velocity gradient, are thus higher in smaller capillaries [106].

3.3.1 Steady shapes

We consider a vesicle in two-dimensional bounded Poiseuille flow. As already mentioned, the reduced area ν is fixed to 0.6 to be close to an RBC. The Stokes equation is solved on the membrane using the boundary integral method representation (2.31), and the expression of Poiseuille flow in (3.5) for the imposed flow $\mathbf{u}^\infty$. The appropriate Green's functions for a flow bounded by two plane walls are described in section 2.3.2. Several numerical [31, 107] and experimental [108, 109] studies showed the existence of several shapes adopted by the vesicle as function of the capillary number C_a and the confinement C_n.
There are three families of shapes, the symmetric shapes, where the vesicle center of mass always remains on the symmetry axis of the channel. The asymmetric shapes, where the center of mass is dispatched vertically, while the vesicle membrane shows a TT motion. The oscillatory shapes which correspond to a transition between symmetric and asymmetric shapes, in which the vesicle shows an oscillatory motion like a swimmer flagella. In the following, those shapes will be discussed in details.
For the viscosity ratio $\lambda = 1$, Kaoui et al. presented in a phase diagram the resulting shapes as function of C_k and C_s in Figure 3.13, where five distinct regions are identified.

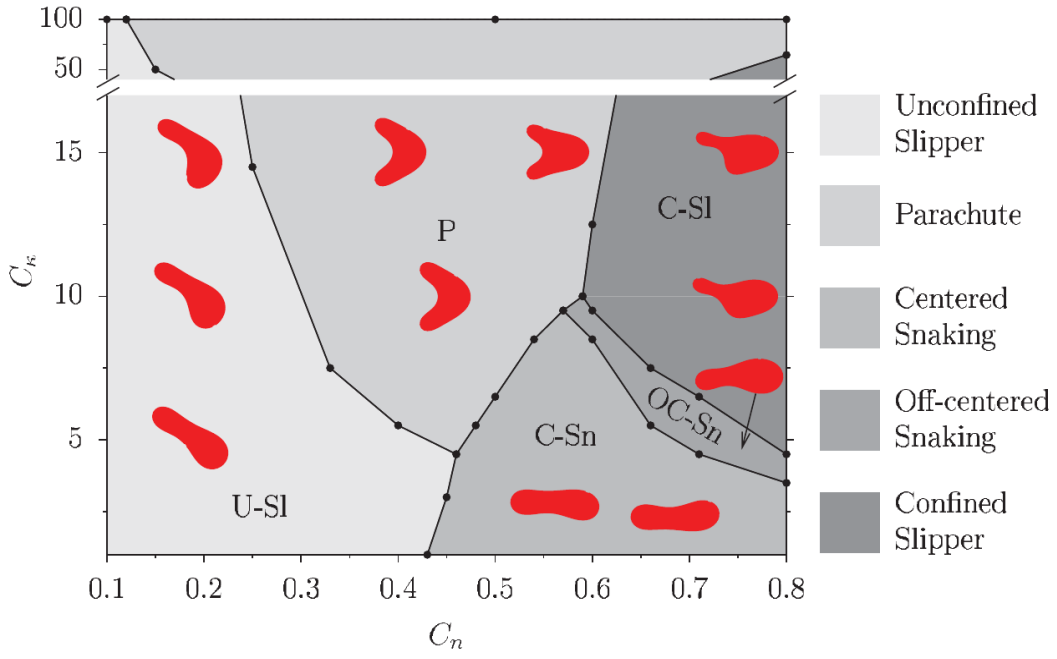

FIGURE 3.13: Phase diagram of a vesicle in Poiseuille flow for $\lambda = 1$ [31]

For $C_k \geq 10$, a weak confinement C_n gives the unconfined slipper (U-Sl)(Figure 3.16.b and 3.16.c), while a strong confinement leads to the confined slipper (C-Sl) (Figure 3.16.d and 3.16.e). The slipper shapes belongs to the asymmetric shapes. For

an intermediate confinement, the vesicle adopt the symmetric parachute shape (Figure 3.15). When the flow strength becomes weak $C_k < 10$, the intermediate oscillatory shapes emerges, that has been called "Snaking" (Sn). The oscillation may be centered (C-Sn) (where the mean value of y_{cm} component of the center of mass, over a period of oscillation, is equal to zero), or off-centered (OC-Sn) (the mean value of y_{cm} is different from zero).
In microcirculation, where the viscosity contrast is $\lambda \simeq 5$, RBCs must deform to fit the smallest blood vessels like the capillaries. Most of the experiment observe that the cells adopt the symmetric parachute-like shape. The asymmetric slipper shape is also observed experimentally in microvessels upon increasing the flow strength. Several studies investigated the different shapes encountered by the RBCs with various flow strength, degree of confinement, and viscosity ratio [27, 110, 111].
In Figure 3.14 we reproduce in parts the phase diagram from Figure 3.13 for $\lambda = 1$, where $C_k = C_a * W$. We focused on the oscillatory shape which appear in our simulation for $C_a W < 9$. We find that in this region there is coexistence between the CSn and the parachute/unconfined slipper shapes.

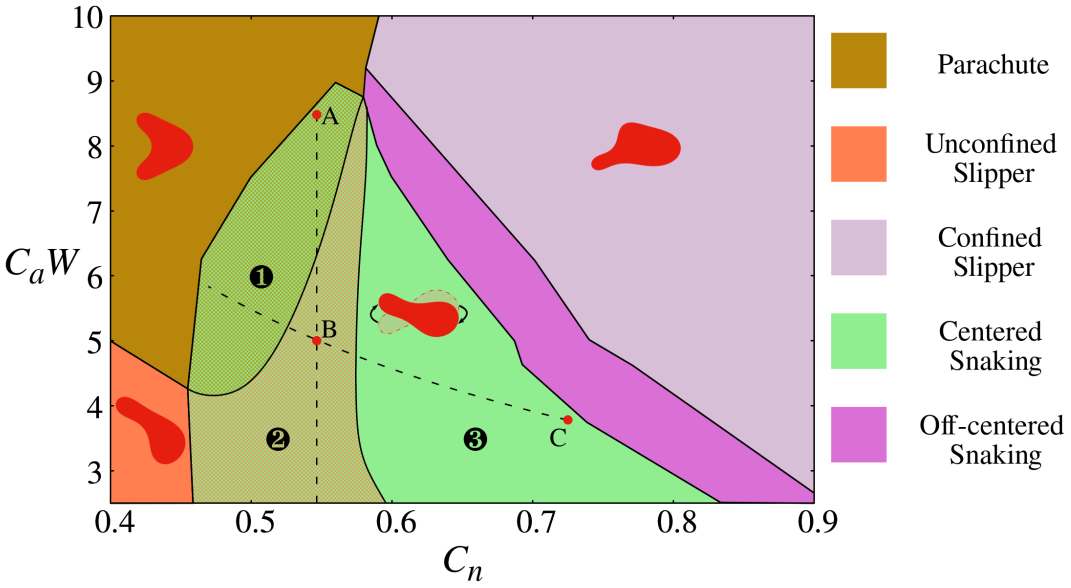

FIGURE 3.14: Phase diagram showing the different shapes of a vesicle in a steady Poiseuille flow as a function of the capillary number C_a and the confinement C_n. The region where centered snaking shapes (CSn) are found consists of three different parts: two regions of coexistence (❶: CSn and parachutes, ❷: CSn and unconfined slippers) and the region ❸, where only CSn are found. The amplitude and the frequency along the dashed lines are shown in Figure 3.22.

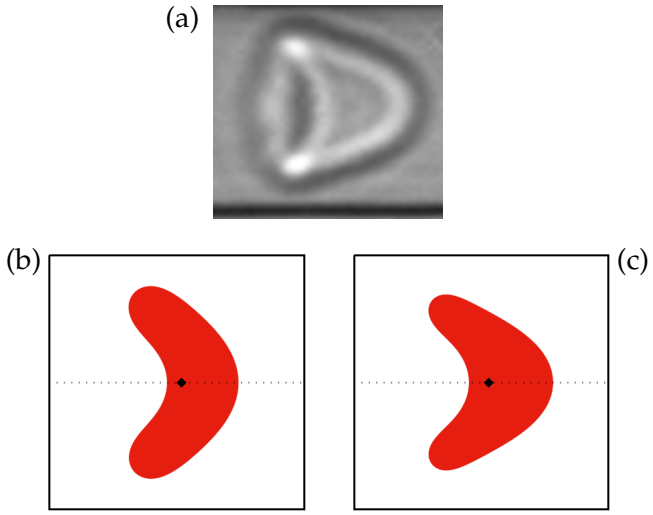

FIGURE 3.15: Parachute shape. (a) picture of parachute shape in microfluidic experiment (with permission of A.Kihm). (b) parachute shape for $C_aW = 5$ and $C_n = 0.5$. (c) parachute shape for $C_aW = 10$ and $C_n = 0.5$. ◆ represent the center of mass of the vesicle.

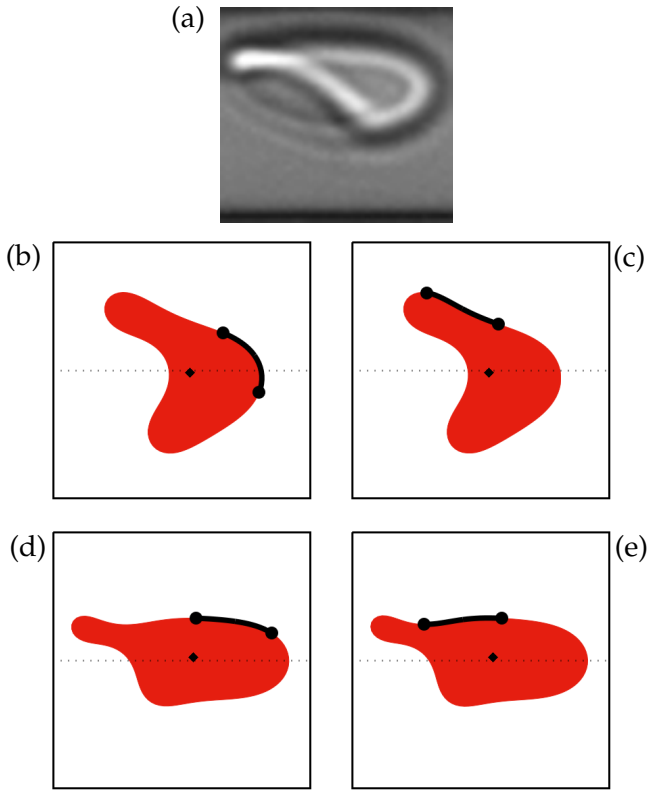

FIGURE 3.16: Slipper shape. (a) picture of slipper shape in microfluidic experiment (with permission of A.Kihm). (b) and (c) represent the unconfined slipper shape for $C_aW = 4$ and $C_n = 0.2$, respectively at a given time t and $t + dt$. (d) and (e) represent the confined slipper shape for $C_aW = 10$ and $C_n = 2$, respectively at a given time t and $t + dt$. ◆ represent the center of mass of the vesicle, and ●—● shows the TT motion from time t to $t + dt$.

3.3.2 The snaking shape

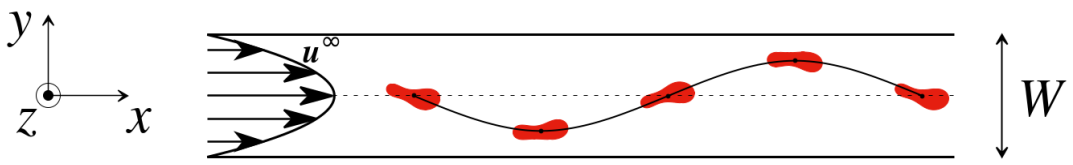

FIGURE 3.17: Sketch of the Centered snaking shape in a steady Poiseuille flow for $C_aW = 5$ and $Cn = 0.55$ (cf. point B in Figure 3.14)

The region of the CSn is located at weak external flows ($C_aW < 9$). When the walls of the confinement are sufficiently far away from the vesicle ($Cn \leq 0.45$), one either observes stable parachutes or unconfined slippers (Figure 3.18). Decreasing the size of the channel enhances the interaction between the channel and the vesicle (the lift force applied by the channels increases). During the simulation, the vesicle evolves towards a stable shape but is repelled by the fluid interactions with one wall towards the other one (lift forces). It again tries to adopt a stable shape but is pushed back again (Figure 3.19). The resulting oscillation gives rise to the CSn (Figure 3.17). When the channel is not yet too small ($0.45 \leq Cn \leq 0.6$), the vesicle will not necessarily adopt the CSn but can become a parachute or an unconfined slipper as well, depending on the initial conditions of the simulation. The resulting regions of coexistence between the CSn and the parachutes/unconfined slippers are depicted in Figure 3.14. For larger confinement ($C_n \geq 0.6$), the coexistence ceases since the walls are so close that the unconfined shapes are not possible anymore.
That regions of coexistence between parachutes and slippers have already been observed for vesicles whose inner fluid viscosity was five times the viscosity of the surrounding fluid [32].

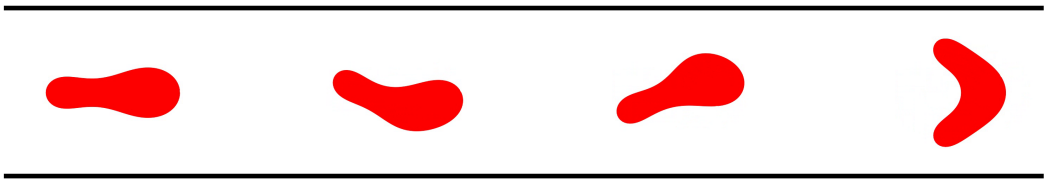

FIGURE 3.18: Transition to parachute shape for $C_aW = 5$ and $C_n = 0.4$.

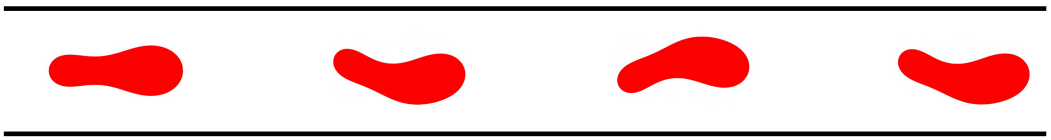

FIGURE 3.19: Transition to snaking shape for $C_aW = 5$ and $C_n = 0.55$.

To characterize the oscillation of the CSn in more detail, we choose to follow the temporal evolution of the vertical position of the center of mass of the vesicle, y_{cm}.

The maximal vertical distance of the center of mass from the mid-line, y_{cm}^{max}, is a measure for the amplitude of the CSn. Figure 3.20 shows an example for $C_aW = 5$ and $C_n = 0.55$ which corresponds to point B in the phase diagram in Figure 3.14. After the transient oscillation, the vesicle starts oscillating periodically as one can see in Figure 3.20.a and the zoom in Figure 3.20.b. The Poincare-map in Figure 3.20.c shows a non-circular limit cycle, which implies that the oscillation of the vesicle is not harmonic. The Fourier transform of y_{cm} in Figure 3.20.d confirms this observation. Increasing the confinement leads to the off-centered snaking, where the oscillation axis of the center of mass is dispatched vertically, see Figure 3.21. Aouane et al. [33] found that for certain confinement values the center of mass oscillation becomes multi-periodic and even chaotic. This behavior is out of interest in this thesis.

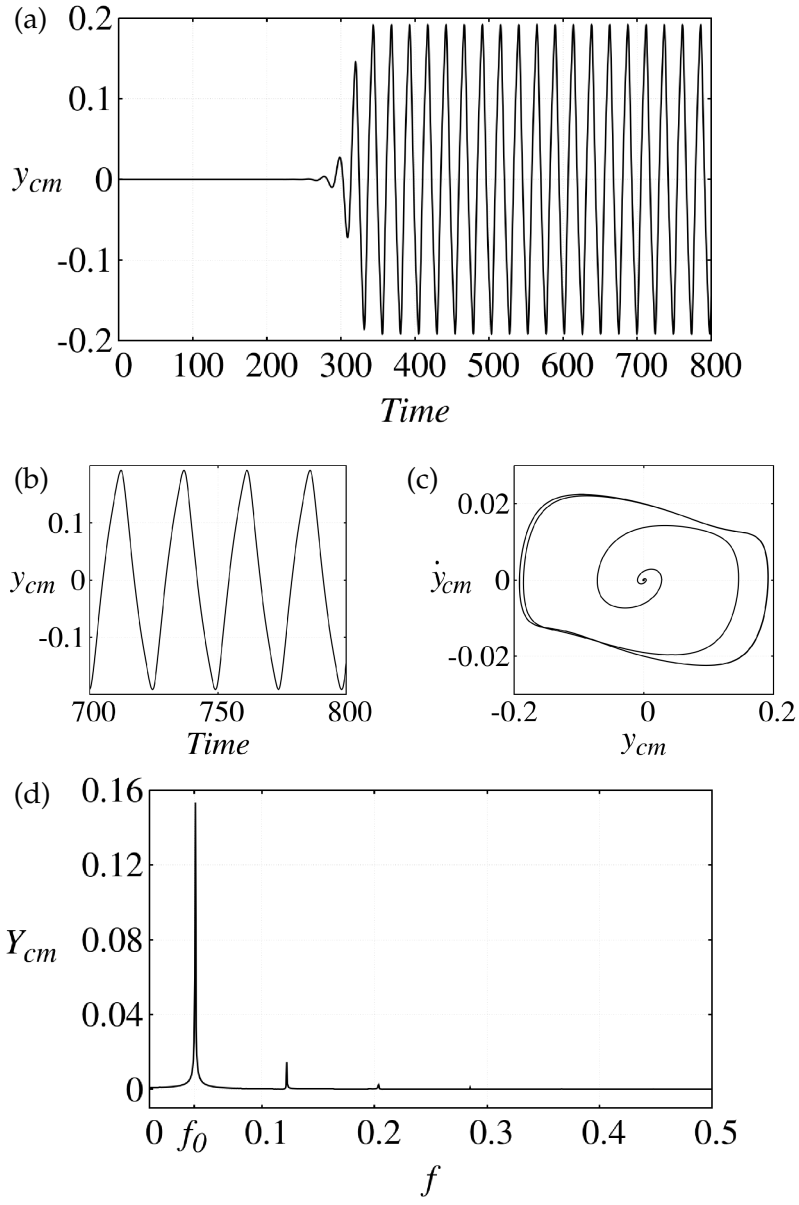

FIGURE 3.20: Centered snaking shape in a steady Poiseuille flow for $C_aW = 5$ and $C_n = 0.55$ (cf. point B in Figure 3.14). (a) Vertical component of the vesicle center of mass y_{cm} as a function of time. (b) Zoom of (a). (c) Poincare map, and (d) the Fourier transform of the signal of (a).

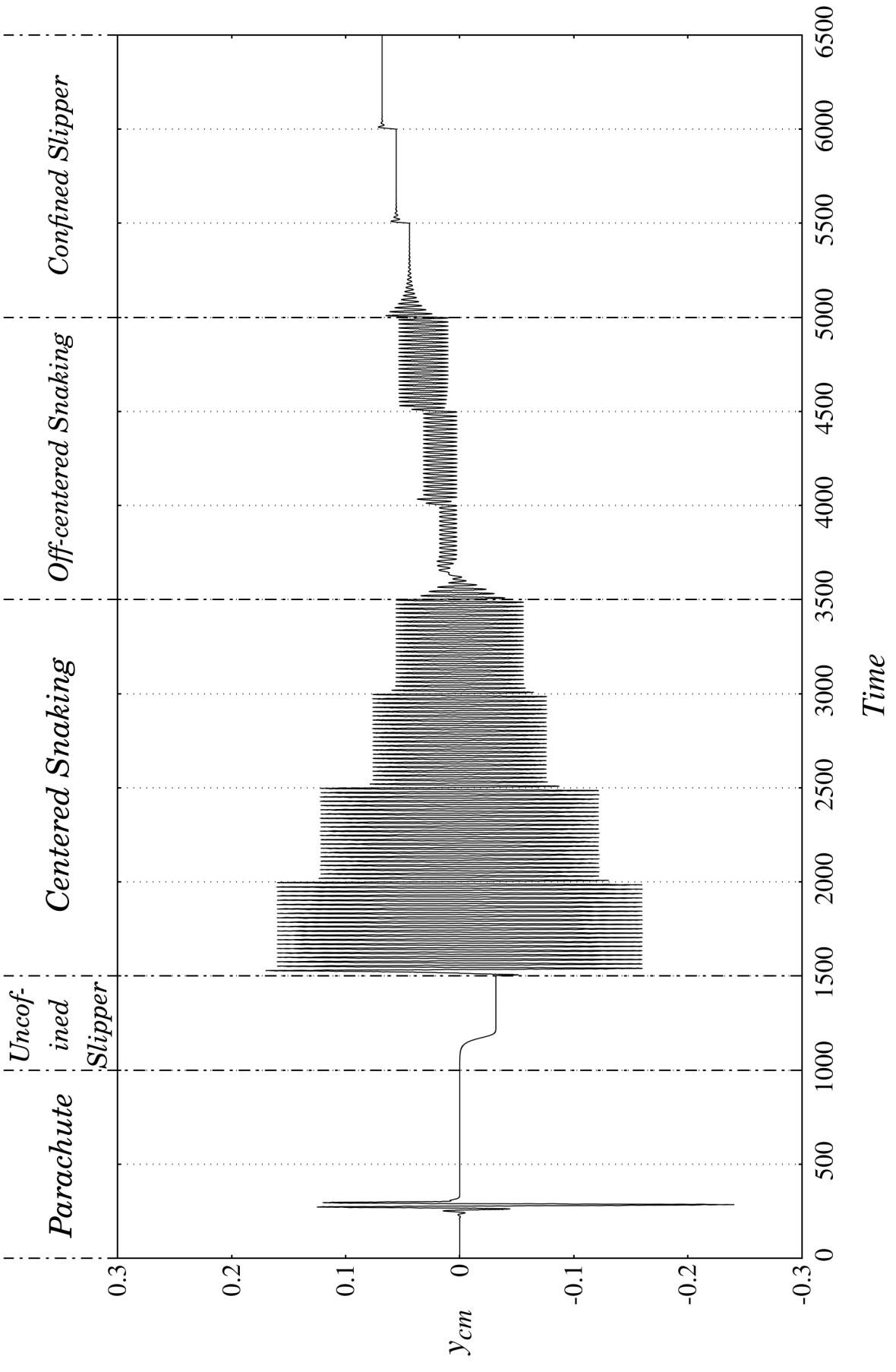

FIGURE 3.21: Temporal evolution of the vertical component of the vesicle center of mass y_{cm} for a fixed $C_a = 1.37$ and different confinement C_n. At every 500 time step the confinement is increased. from time 0 to 6500 the used channel width W are respectively:
$4.36 - 3.96 - 3.66 - 3.36 - 3.06 - 2.76 - 2.66 - 2.56 - 2.46 - 2.36 - 2.26 - 2.16 - 2.06$.

An increase of C_a or C_n intensifies the interaction between the fluid and the vesicle membrane. The amplitude of the oscillation of the CSn will thus be attenuated as one can see in Figure 3.22. At the same time we observe an increase of the fundamental frequency of the oscillation which becomes almost a constant close to the boundaries of the region of CSn. In Figure 3.22.a the confinement is set to $C_n = 0.55$ while C_a is increased until the vesicle changes its shape to a parachute. In Figure 3.22.b we fix $C_a = 1.37$ and increase Cn (decreasing the channel width) until the vesicle reaches the off-centered snaking shape.

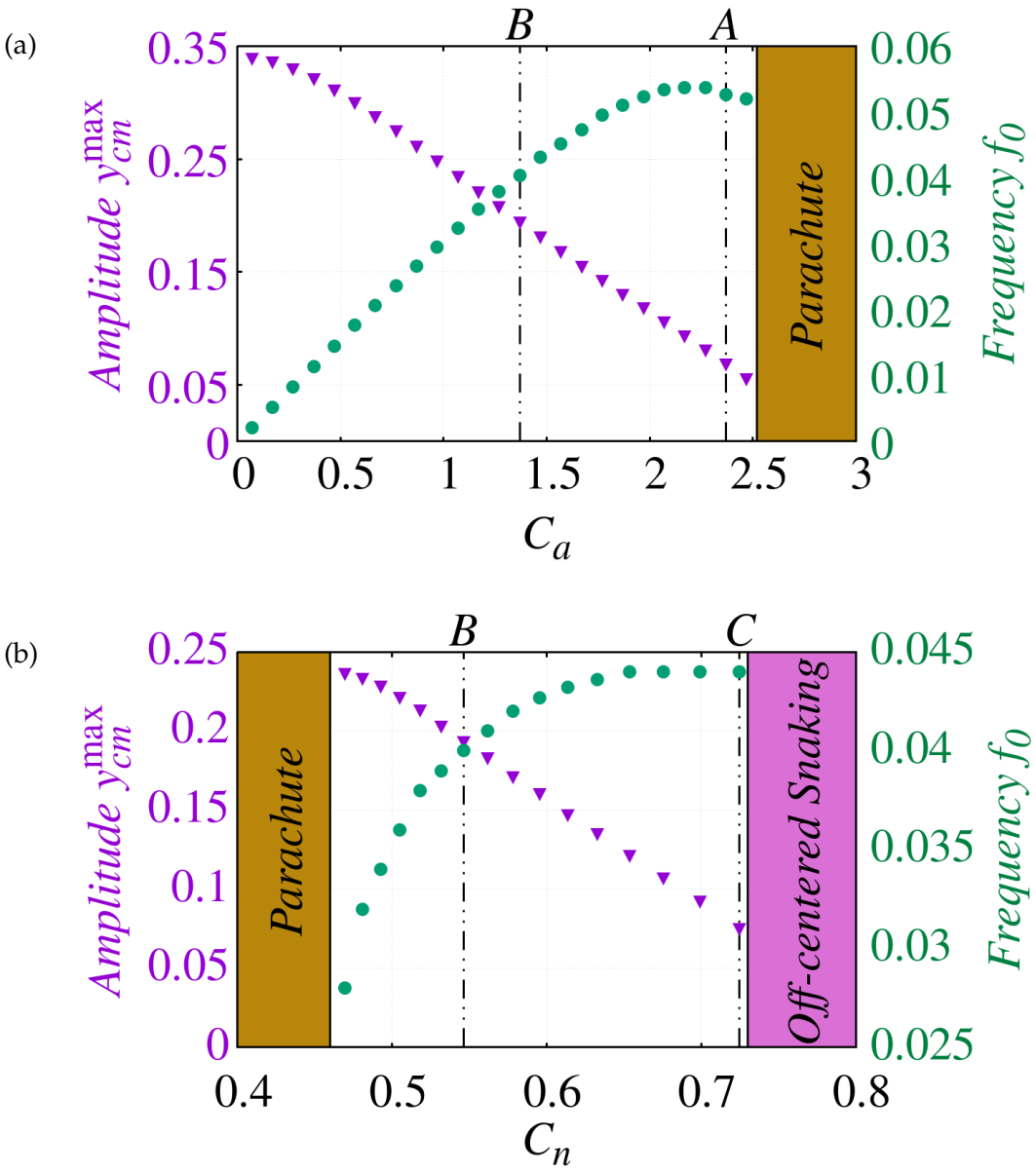

FIGURE 3.22: Amplitude (triangles) and frequency (circles) of the oscillation of the CSn (a) for a fixed confinement $C_n = 0.55$ and (b) for a fixed capillary number $C_a = 1.37$. The points A, B, and C are shown in the phase diagram, Figure 3.14, together with the two dashed curves corresponding to $C_n = 0.55$ and $C_a = 1.37$, respectively.

3.4 Vesicles in modulated Poiseuille flow

RBCs in circulation are subject to unsteady flow. The intermittent nature of heart-pumping causes the flow to be pulsatile. The unsteadiness can also arise due to the contraction and recoil of smaller arteries regulating local circulation [112], or diseased arteries with various degrees of atherosclerosis [113]. The fluctuation over the blood flow in capillaries is introduced by adding an additional term to the Poiseuille flow equation, it reads,

$$\mathbf{u}^{\infty}(x,y) = \begin{cases} u_x^{\infty} = V_{max}\left(1 - \dfrac{4y^2}{W^2}\right)\left[1 + \varepsilon_m cos\left(2\pi f_m t\right)\right] \\ u_y^{\infty} = 0 \end{cases}, \tag{3.8}$$

where V_{max} is the maximal velocity occurring in the middle of the channel. The parameters ε_m and f_m, respectively, represent the amplitude and the frequency of a modulated Poiseuille flow. The frequency f_m describes how fast the flow is oscillating, we only consider frequencies which are much smaller than the characteristic shear rate of the flow field $\dot{\gamma}$ in the channel. This implies that we can assume a quasi-steady Stokes flow, and therefore, use the BIM formulation in section 2.3.2. For $\varepsilon_m = 0$ we recover the usual steady Poiseuille flow.

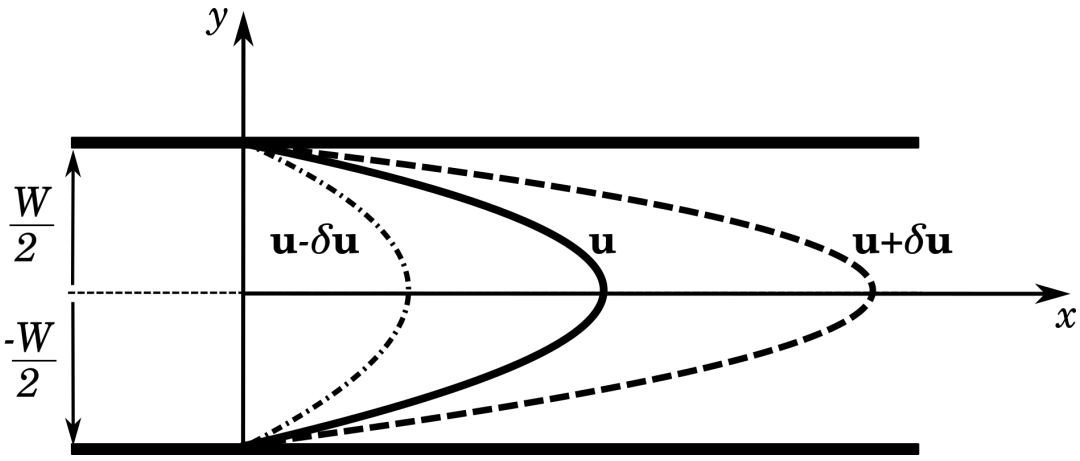

FIGURE 3.23: Sketch of a modulated Poiseuille flow, where $\delta\mathbf{u} = \mathbf{u}\,\varepsilon_m\,cos\left(2\pi f_m t\right)$ (from 3.8). — — shows flow profile for a maximal fluctuation ($cos\left(2\pi f_m t\right) = 1$), and — · — shows the minimal fluctuation ($cos\left(2\pi f_m t\right) = -1$).

The same type of flow modulation has been used by Farutin and Misbah for an analytical study of the rheological properties of a single vesicle in shear flow [114]. They have shown theoretically that the effective viscosity exhibits resonance for vesicles, similarly to what happens for capsules [115]. Matsunaga et al. also used this type of oscillating flow profile to study capsule deformation in shear flow [116]. Noguchi et al. mimicked the oscillating Poiseuille flow using a microchannel whose width varies periodically [117].
There have been also few studies that address the effect of pulsatile flow on RBC dynamics in microcirculation [118, 119, 120]. Nakajima et al., for example, have studied the deformation response of RBCs in a sinusoidally varying shear flow generated in a cone-and-plate viscometer [121]. A major finding of their experiment is that the deformation response is not identical during different phases of the shear flow. The deformation is higher during the retarding phase and lowers during the accelerating

phase. They noted that such an unequal response was probably due to the rheological properties of the intracellular fluid and its interaction with the membrane.
The effect of the fluctuation amplitude ε_m, and the frequency f_m, over the vesicle shape will be studied in the following.

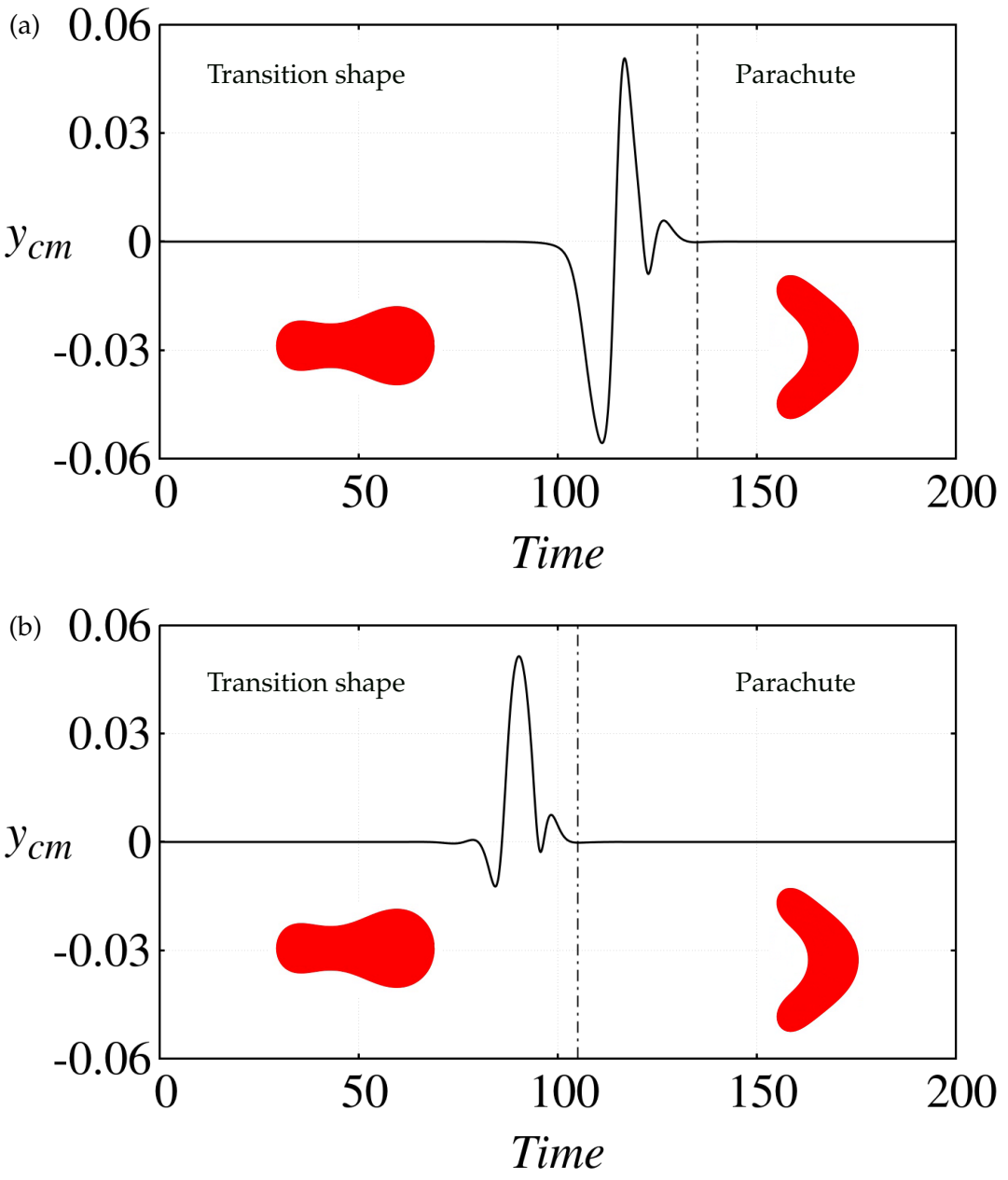

FIGURE 3.24: Temporal evolution of the vertical component of the vesicle center of mass y_{cm} for $C_a = 2.5$ and $C_n = 0.5$. (a) For a steady Poiseuille flow. (b) For oscillating Poiseuille flow modulated with $\varepsilon_m = 0.2$ and $f_m = 0.05$.

In steady Poiseuille flow, and depending on the Capillary number, the vesicle will resist to the imposed flow and will take a certain time to reach a final shape. For an oscillating flow this time can be decreased depending on the oscillation parameters ε_m and f_m. Comparing Figure 3.24.a with Figure 3.24.b we can observe that the shape transition in oscillating flow is faster than in steady flow. For the highest capillary

number, the vesicle quickly adopts the final shape (parachute or slipper). Therefore, the effect of the flow oscillation is insignificant in this case.

3.4.1 Steady shapes

Here we are interested in the response of the fully developed parachute and slipper shapes to the oscillation of the imposed flow. The oscillation amplitude is fixed at $\varepsilon_m = 0.2$ and the frequency $f_m = 0.05$. The vesicle shape response to the flow oscillation for parachute and for both, unconfined, and confined slippers are shown, respectively in Figure 3.25, 3.26, and 3.27.

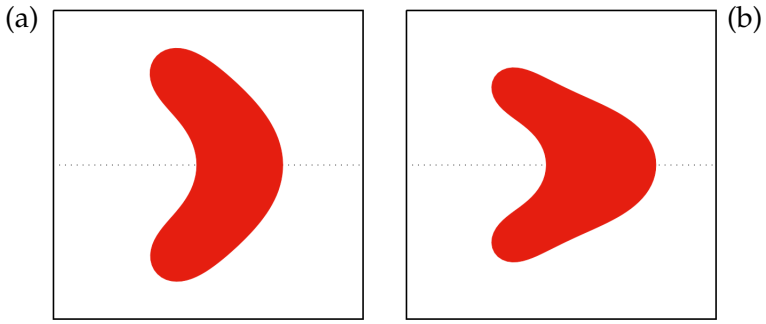

FIGURE 3.25: Parachute shape in oscillating flow, (a) is the minimal deformation, and (b) is the maximal one.

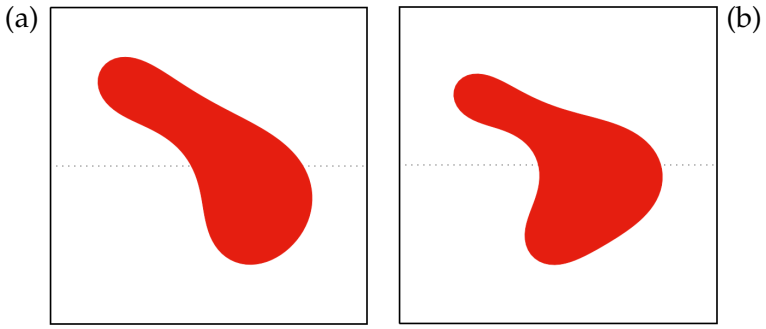

FIGURE 3.26: Unconfined slipper in oscillating flow, (a) is the minimal deformation, and (b) is the maximal one.

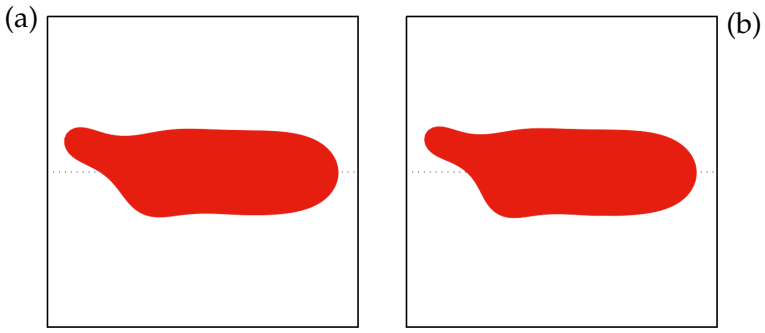

FIGURE 3.27: Confined slipper in oscillating flow, (a) is the minimal deformation, and (b) is the maximal one.

For the parachute shape, where the flow strength is more dominant over the confinement, the shape undergoes a breathing like motion following the flow oscillation, for the unconfined slipper, the vesicle will also oscillate, but between two unconfined slipper shapes. For the confined slipper, the shape is imposed by the confinement, consequently, the flow oscillation has an insignificant influence on the vesicle shape. Next, we focus only on the parachute response, where we interpret the shape response to the oscillation using the distance between two points laying on the symmetry axis of the channel, and where their vertical component is null (because of the non TT motion in the symmetric parachute shape), as shown in Figure 3.28.

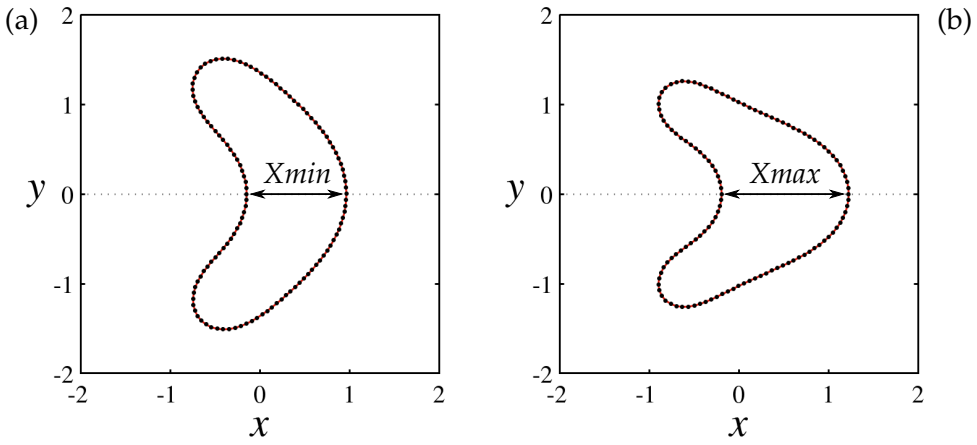

FIGURE 3.28: Parachute shape ($C_a = 2.5$ and $C_n = 0.5$) in oscillating flow, (a) is the minimal deformation, and (b) is the maximal one. X_{min} and X_{max} represent the distance between two points laying in the center x axis, respectively, for the minimal and maximal deformation.

For a fixed oscillation amplitude $\varepsilon_m = 0.2$, we have varied the frequency f_m and we report the vesicle response with the quantity $X = X_{max} - X_{min}$ in Figure 3.29. As expected, if the flow oscillation becomes faster $f_m \geq 1$, the vesicle will not follow, and the oscillation will not affect the vesicle shape anymore. Only the small frequencies have a significant effect. Increasing the amplitude ε_m will increase the vesicle oscillation (X increases), but no shape transformation has been observed.

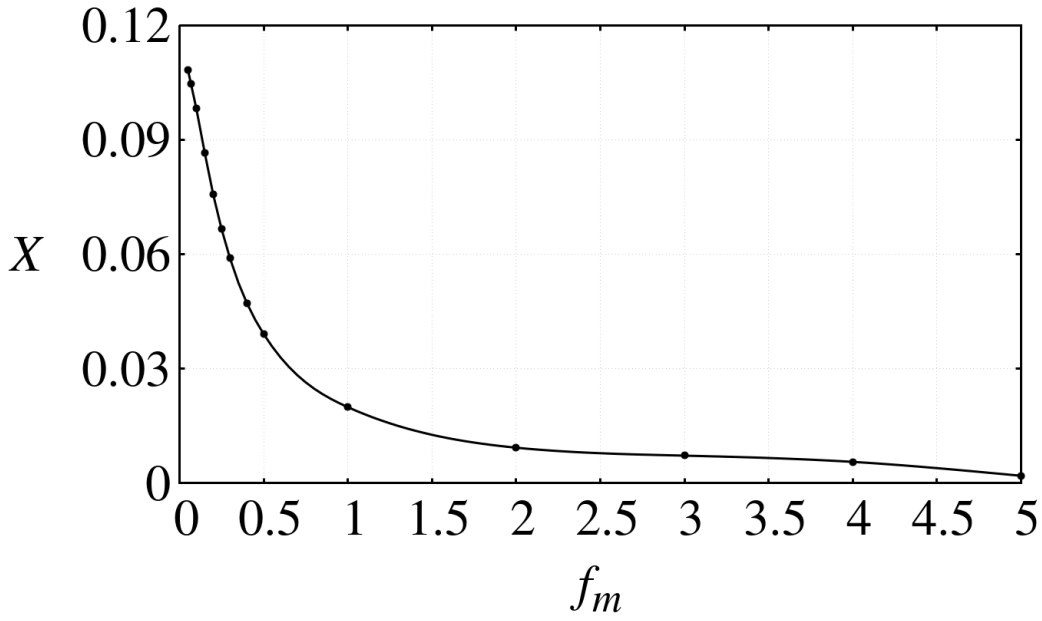

FIGURE 3.29: Variation of the distance $X = X_{max} - X_{min}$ (see Figure 3.28), as function of the oscillation frequencies f_m. The data point are linked by an spline curve.

3.4.2 The snaking shape

In the following section the effect of the oscillation over the snaking shape is studied. Three points (A, b, and C) from the phase diagram will be considered (see Figure 3.14). Each point lies in one of the three regions where the centered snaking shape can be found. The first point, A, with $C_a = 2.33$ and $C_n = 0.55$ lies in the region of coexistence between the CSn and the parachutes close to the upper boundary of the region. The second point, B, corresponds to the same confinement as point A but smaller capillary number $C_a = 1.37$. It lies in the region of coexistence between the CSn and the unconfined slippers. Finally, we choose the point C as representative of the region where only CSn are found by keeping the capillary number of point B but increasing the confinement to $C_n = 0.72$.
After the vesicle has reached the CSn in Poiseuille flow, we switch on the oscillating flow using the profile. The frequency f_m is fixed to the fundamental frequency in steady Poiseuille flow which can be read off from Figure 3.22. The vesicles corresponding to the three considered points are then perturbed by varying the amplitude ε_m. As the point A is near to the boundary of the parachute region, a small amplitude $\varepsilon_m = 0.2$ with $f_m = 0.05$ can already induce a migration to the parachute shape. When we impose a steady Poiseuille flow again, the vesicle stays in the parachute shape as expected since A lies in the region of coexistence between the two shapes. The CSn of point B can as well be forced to evolve to the parachute shape but a much higher amplitude is needed ($\varepsilon_m = 1$). After imposing a steady Poiseuille flow again the vesicle takes on the shape of an unconfined slipper since the point B lies in the region of coexistence between the CSn and the unconfined slippers, as shown in Figure 3.30. In point C the vesicle is more confined than in A and B. Therefore, we cannot force it away from the CSn even if we apply the same high perturbation ($\varepsilon_m = 1$). The shapes found in the three points for steady Poiseuille flow after switching off the time-dependence of the flow are all in agreement with the dashed areas in Figure 3.14.

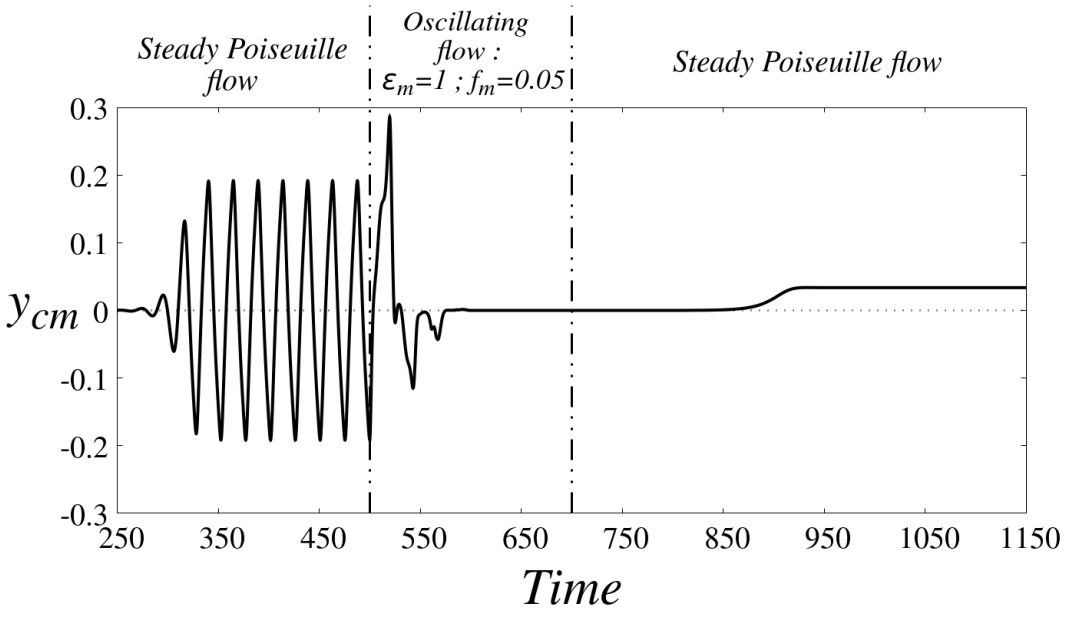

FIGURE 3.30: Shape transition from centered snaking to the unconfined slipper through the parachute under an oscillating Poiseuille flow.

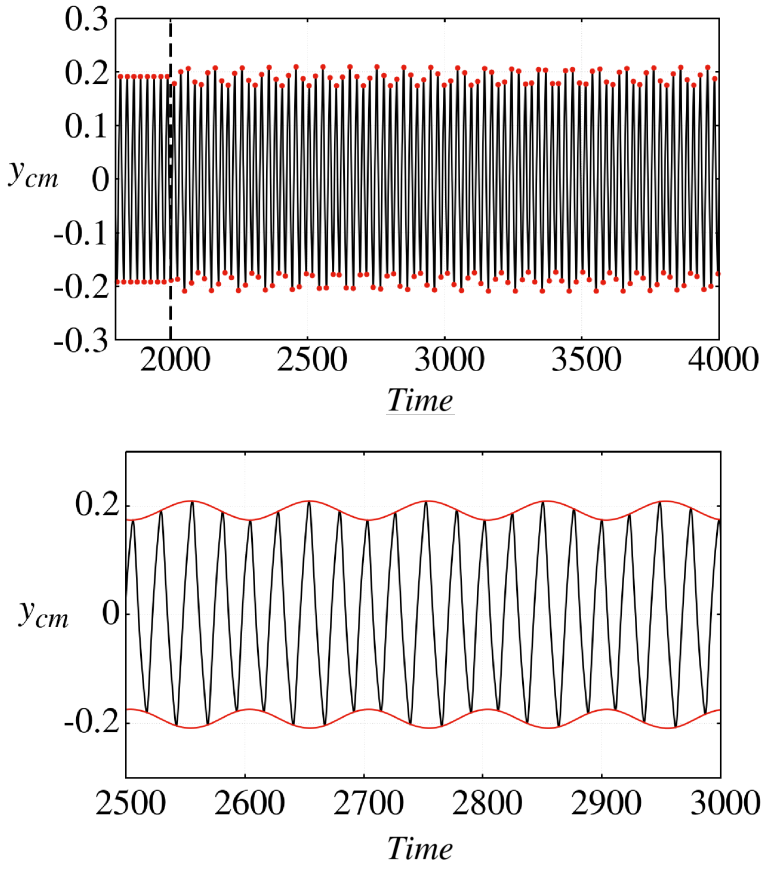

FIGURE 3.31: (a) Vertical component of the vesicle center of mass as a function of time in a modulated Poiseuille flow of amplitude $\varepsilon_m = 0.1$ and frequency $f_m = 0.01$ around the point B, for which $C_a^0 = 1.37$, $y_{cm}^0 = 0.19$, and $f_0 = 0.04$. (b) Zoom of (a).

Now, in order to study the effect of the frequency f_m, we fix the oscillation amplitude ε_m and we follow the vertical component of the center of mass y_{cm} for different oscillation frequency f_m. We start with a CSn with a center of mass that oscillates periodically with amplitude y_{cm}^0 and fundamental frequency f_0. When it is put into a modulated flow of fixed amplitude ε_m and frequency f_m, the oscillation becomes more complicated. Figure 3.31 shows one example for the point B with $\varepsilon_m = 0.1$ and $f_m = 0.01$.
The investigated system is obviously not a linear time invariant (LTI) system, because the output contains non vanishing amplitudes at frequencies different from the input frequency [122], as shown in Figure 3.32). However, at a first approximation, the nonlinear response of the system to the harmonically modulated flow can be treated using a quasi-stationary approach. The scaled frequencies f_m and f_0 are both much smaller than one which implies that the elastic modes of the vesicle relax very quickly compared to a typical period of the shape oscillation. The time-dependent flow amplitude instantaneously affects the oscillation of the vesicle. Since the flow is directly proportional to the capillary number C_a, we can use Figure 3.22.a to predict the behavior of the system. The imposed oscillation of C_a around the value of the initial CSn, C_a^0, enforces an oscillation of position and frequency of the vesicle center of mass. These quantities are approximately linear in C_a (see Figure 3.22.a), which allows to approximate the oscillation of the center of mass using a mixed modulation [123].
A vesicle with a CSn motion in steady Poiseuille flow is put into a harmonically modulated Poiseuille flow (see 3.8). This implies an oscillation of the capillary number C_a of the system which is directly proportional to the imposed flow. C_a is thus harmonically modulated with the same amplitude ε_m and frequency f_m as the flow,

$$C_a(t) = C_a^0[1 + \varepsilon_m \cos(2\pi f_m t)] \,, \tag{3.9}$$

where C_a^0 is the capillary number corresponding to the initial CSn. In other words, we force the system to oscillate on a vertical line of the phase diagram (Figure 3.14). From the data of Figure 3.22.a we can obtain linear fits for amplitude and fundamental frequency of the vertical component of the vesicle center of mass as a function of C_a,

$$y_{cm}^{\max}(C_a) = y_{cm}^0 - a(C_a - C_a^0) \quad \text{and} \quad f(C_a) = \frac{f_0}{C_a^0} C_a \tag{3.10}$$

with $a = 0.13$. The value of a is obtained by neglecting the points for which $C_a < 0.3$. The fit of f is only acceptable for $C_a < 1.6$ since the error becomes too large for higher values of C_a. The parameters y_{cm}^0 and f_0 are the fundamental frequency and capillary number of the initial CSn.
Inserting $C_a(t)$ from 3.9 into these fits yields,

$$y_{cm}^{\max}(t) = y_{cm}^0 \left[1 - m \cos(2\pi f_m t)\right] \tag{3.11}$$

with $m = \frac{aC_a^0}{y_{cm}^0} \varepsilon_m$ for the amplitude and,

$$f(t) = f_0[1 + \varepsilon_m \cos(2\pi f_m t)] \tag{3.12}$$

for the frequency as a function of time.

The whole signal thus consists of a simultaneous amplitude and frequency modulation. This mixed modulation (referred as MM) can be written as,

$$y_{cm}^{\mathrm{MM}}(t) = y_{cm}^{\max}(t)\cos\theta(t) \tag{3.13}$$

with the phase angle,

$$\theta(t) = 2\pi\int_0^t f(t')\mathrm{d}t' = 2\pi f_0 t + \beta\sin(2\pi f_m t) \tag{3.14}$$

where $\beta = \frac{f_0}{f_m}\varepsilon_m$ is the index of the frequency modulation. Putting everything together we obtain,

$$y_{cm}^{\mathrm{MM}}(t) = y_{cm}^0[1 - m\cos(2\pi f_m t)] \times \cos\left[2\pi f_0 t + \beta\sin(2\pi f_m t)\right] \tag{3.15}$$

where $m = \frac{0.13\times C_a^0}{y_{cm}^0}\varepsilon_m$ and $\beta = \frac{f_0}{f_m}\varepsilon_m$ are the indices of, respectively, amplitude and frequency modulation [1].
The envelope of y_{cm}^{MM} oscillates between $y_{cm}^0(1 \pm m)$ and does not depend on the frequency f_m of the flow. One can easily show that

$$\begin{aligned}\frac{y_{cm}^{\mathrm{MM}}(t)}{y_{cm}^0} &= \cos(2\pi f_0 t) - \frac{(\beta+m)}{2}\cos\left[2\pi(f_0 - f_m)t\right] \\ &\quad + \frac{(\beta-m)}{2}\cos\left[2\pi(f_0+f_m)t\right] + \ldots\end{aligned} \tag{3.16}$$

to highest order in m and β. The resulting spectrum consists of the fundamental frequency f_0 of the initial CSn and sidebands with frequencies $f_0 \pm nf_m$ ($n \in \mathbb{N}$), which are due to the mixed modulation.
Figure 3.32 shows for $f_m = 0.01$ and $\varepsilon_m = 0.1$ that the analytical approximation in (3.16), describes the result of the simulation surprisingly well. Even the amplitudes of the sidebands around the fundamental frequency f_0 (see FFT in Figure 3.32.b) are predicted correctly with our simple model.
When the modulation frequency f_m of the flow is exactly a multiple of the fundamental frequency, $f_m = nf_0$ ($n \in \mathbb{N}$), the upper and lower envelopes of y_{cm} should be constants according to the analytical theory in 3.15. For an even n the total envelope should be symmetric with respect to the center of the channel whereas it should be asymmetric for odd n. This implies that there are two solutions with constant envelope for odd n: one with envelope situated at y^+ and $-y^-$ and a second one with envelope at y^- and $-y^+$. To check these predictions we again focus on the point B in the following and fix ε_m to a value smaller than one to avoid any changement to the unconfined slipper shape. Looking at the simulations, we observe that the oscillation of y_{cm} *does not* display a constant envelope for $f_m = f_0$. The numerical results indicate that the two solutions with *asymmetric* constant envelope (n is odd) are linearly unstable; the system oscillates between them. However, one indeed finds a constant envelope for $f_m = 2f_0$, which is symmetric with respect to the channel. But even when f_m is not exactly $2f_0$, the envelope of the signal equals a constant whose value depends on ε_m and f_m. In the following we shows one example for a fixed $\varepsilon_m = 0.7$.

[1] Note that we do not take into account the higher harmonics of the initial CSn in this approach to simplify the discussion.

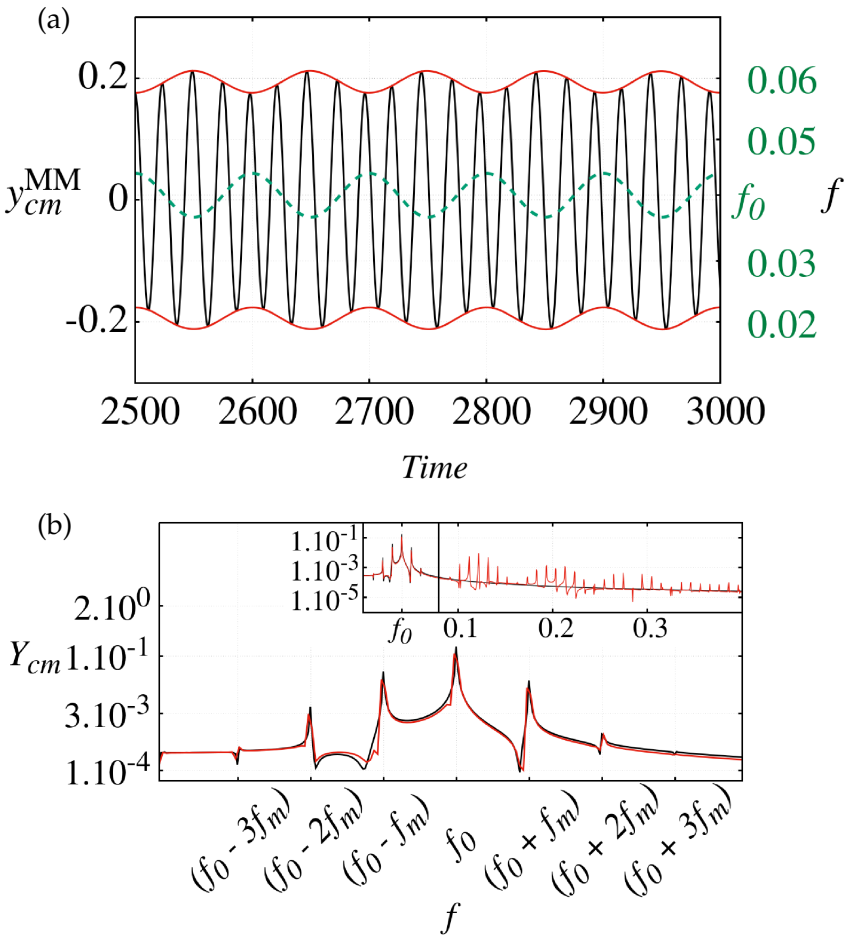

FIGURE 3.32: (a) Corresponding mixed modulation signal y_{cm}^{MM} with indices of modulation $m = 0.09$ and $\beta = 0.4$ together with envelope (solid red) and frequency (dashed green). (b) Comparison of the Fourier transforms of theory (black) and simulation (red).

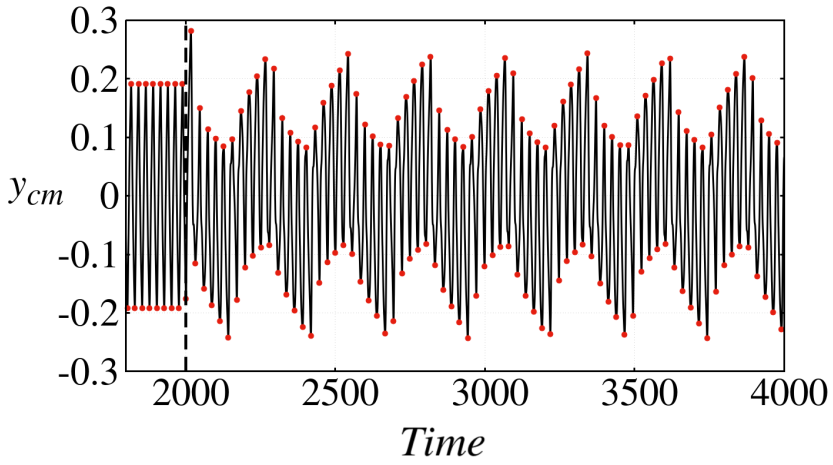

FIGURE 3.33: Vertical component of the vesicle's center of mass, y_{cm}, as function of time in Poiseuille flow modulated with the amplitude $\varepsilon_m = 0.7$ and frequency $f_m = 0.04$. The dashed line represents the time at which the modulation of the Poiseuille flow is switched on.

For $f_m = f_0 = 0.04$ the vesicle oscillates between the two asymmetric solutions of constant envelope as mentioned above (see Figure. 3.33).

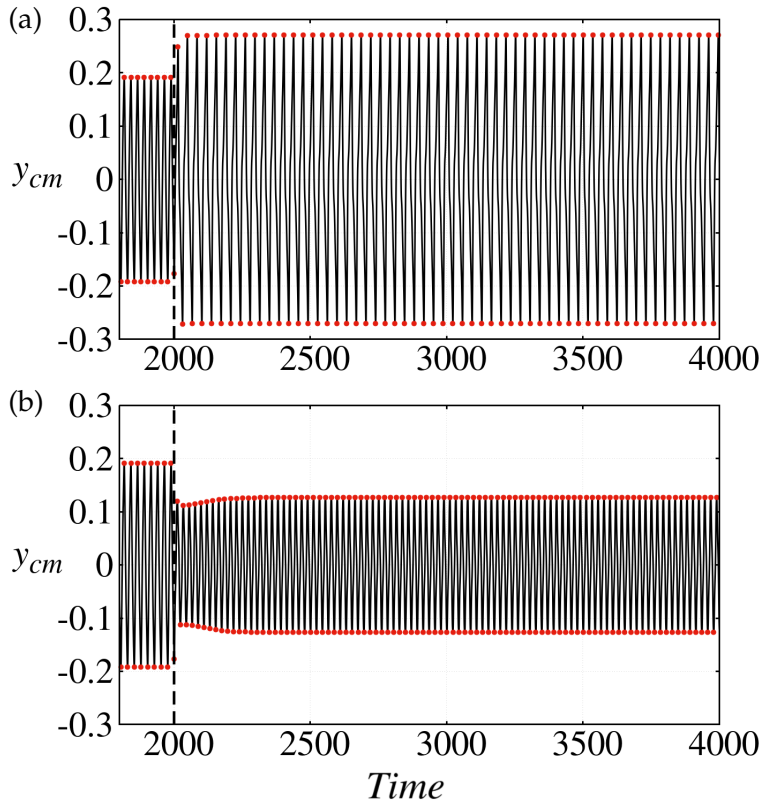

FIGURE 3.34: Vertical component of the vesicle's center of mass, y_{cm}, as function of time in Poiseuille flow modulated the amplitude $\varepsilon_m = 0.7$ and frequencies (a) $f_m = 0.0565$, (b) $f_m = 0.0920$. The dashed line represents the time at which the modulation of the Poiseuille flow is switched on.

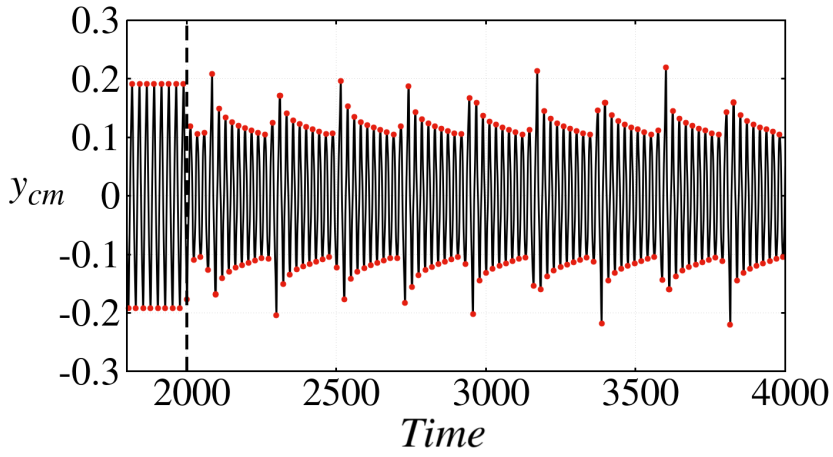

FIGURE 3.35: Vertical component of the vesicle's center of mass, y_{cm}, as function of time in Poiseuille flow modulated with the amplitude $\varepsilon_m = 0.7$ and frequency $f_m = 0.0930$. The dashed line represents the time at which the modulation of the Poiseuille flow is switched on.

Increasing the modulation frequency with a step size of 10^{-3}, the vesicle exhibits stable oscillations already at $f_m = 0.056 < 2f_0$ (see Figure 3.34.a). When increasing the frequency f_m even more, the envelope of the oscillation remains a constant while attenuating until the frequency $f_m = 0.092 > 2f_0$ is reached (Figure 3.34.b). Above this frequency ($f_m > 0.0920$) the envelope of y_{cm} is not a constant again, Figure 3.35. To find the domain of frequencies where the oscillation displays a constant envelope in the simulation, we have varied the modulation amplitude ε_m from 0.1 to 0.9 with a step size of 0.1 ($\varepsilon_m = 1$ is not considered cause for this amplitude the vesicle will evolve to a parachute as discussed before) and the imposed frequency f_m with a step size of 10^{-3}. Fig. 3.36 presents the resulting region (hashed area). Its size increases with increasing ε_m.

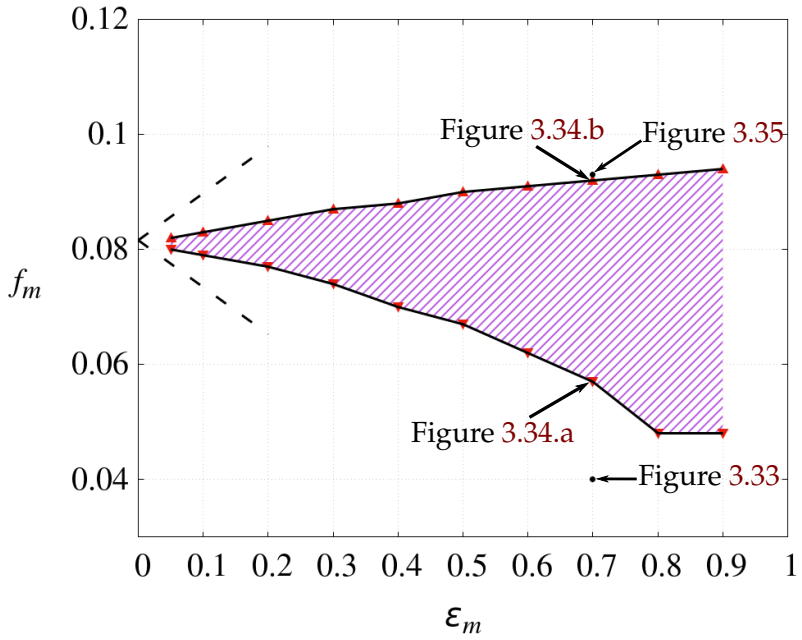

FIGURE 3.36: Region of oscillations with constant envelope (hashed) as a function of the imposed amplitude ε_m and frequency f_m of the modulated flow. The dashed lines indicate an analytical estimate of the boundaries of this region for small ε_m (see text below).

This is due to the fact that the imposed flow not only corresponds to an oscillation around the point B but can also be interpreted as an oscillation around *other* points B′ of same confinement $C_n = 0.55$, as long as their stationary capillary number $C_k^{0'}$ lies in the range of capillary numbers that are reached by the oscillation of the flow. The points B′ all lie on the same vertical line of the phase diagram as point B (see dashed vertical line in Figure 3.14).
A closer look into the results of the simulation reveals that y_{cm} oscillates with a fundamental frequency of $f_0' = f_m/2$ when its envelope is constant. This oscillation corresponds to a mixed modulation around another point of the phase diagram whose stationary CSn has the frequency f_0'. Consequently, there can be two different states depending on the values of f_m and ε_m in our system. State 1 can be understood as a mixed modulation of the stationary CSn of point B, whereas state 2 is a mixed modulation around point B′ with fundamental frequency f_0' and a constant envelope. When f_m is close to $2f_0$, the system is in state 2. However, for this state to be accessible, f_0' has to lie in the range of steady state frequencies (compare Figure 3.22.a)

of the points on the vertical line of the phase diagram that the flow reaches during its oscillation. If we take this criterion as an estimate for the boundaries of the region of oscillations with constant envelope, we obtain the dashed lines depicted in Figure. 3.36.
The discrepancy between this theoretical prediction and the simulations is most probably due to the fact that the oscillation in C_k is only symmetric around the point B but asymmetric for all other points B'. One thus expects a transition region where the system switches between states 1 and 2. This is indeed what we observe: there are frequencies (next to the boundaries of the region of constant envelope) where the system reaches an envelope of constant amplitude which then starts oscillating again. This behavior repeats itself periodically. Further complications arise from the linear approximation of amplitude and frequency ((3.10), where the mixed modulation breaks down for modulation amplitudes larger than $\varepsilon_m \approx 0.2$. When ε_m is close to one we even expect that there are further states that the vesicle might be able to adopt. Simulations for $\varepsilon_m = 0.9$ indeed show that the vesicle tries to take on a shape resembling to a confined slipper but does not quite manage to do so. The underlying theory goes beyond the scope of this paper but could be a promising subject of future studies.

3.5 Two vesicles in Poiseuille flow

In this section, we investigate the distance between a pair of two-dimensional vesicles in a confined Poiseuille flow. As already discussed in section 2.2.6, there are different types of interaction forces between two close lipid bilayer membranes (see section 2.2.6). In the following, we will just consider the hydrodynamic interaction force, where the distance between the two vesicles is only dictated by the external flow. We restrict ourselves to the case where the vesicles adopt a parachute shape, with a reduced area $\nu = 0.65$, and the viscosity ratio $\lambda = 1$. The simulation is done using the BIM method, where the equation (2.31) is evaluated by considering also the influence of the nodes of the second membrane, and it reads,

$$\begin{aligned} u_j(\mathbf{r}_0) = \frac{2}{1+\lambda} u_j^{\infty}(\mathbf{r}_0) \; - \sum_i \frac{1}{2\pi\mu_{ext}(1+\lambda)} \int_{C_i} G_{ij}(\mathbf{r},\mathbf{r}_0)\, f_j(\mathbf{r}) \; \mathrm{d}l(\mathbf{r}) \\ + \sum_i \frac{1-\lambda}{2\pi(1+\lambda)} \int_{C_i}^{PV} u_i(\mathbf{r}) T_{ijk}(\mathbf{r},\mathbf{r}_0) n_k(\mathbf{r}) \; \mathrm{d}l(\mathbf{r}) \end{aligned} \tag{3.17}$$

where the index i stands for the first or the second vesicle. The strength of the interaction between cells is generally governed by the following: their shape and size, the distance between them, their orientation with respect to each other, their individual orientation relative to the direction of the gravitational field, and their velocity and spin relative to the fluid at infinity [124, p.235].
Experimental studies with microfluidic channels showed that RBCs in the capillaries tend to form clusters, due to the hydrodynamic interaction or by the plasma macromolecules [125, 126]. Many numerical studies also observed a pair of vesicles or capsules forming a cluster in a two-dimensional confined and unconfined geometries [127, 128], and also for vesicles and capsules in three-dimensional cylindrical and rectangular channels [129, 111].

Figure 3.37 show two vesicles reaching a stable distance d measured between their respective center of masses. This distance is around $d = 6.2$ for $C_a = 10$ and $W = 4$.

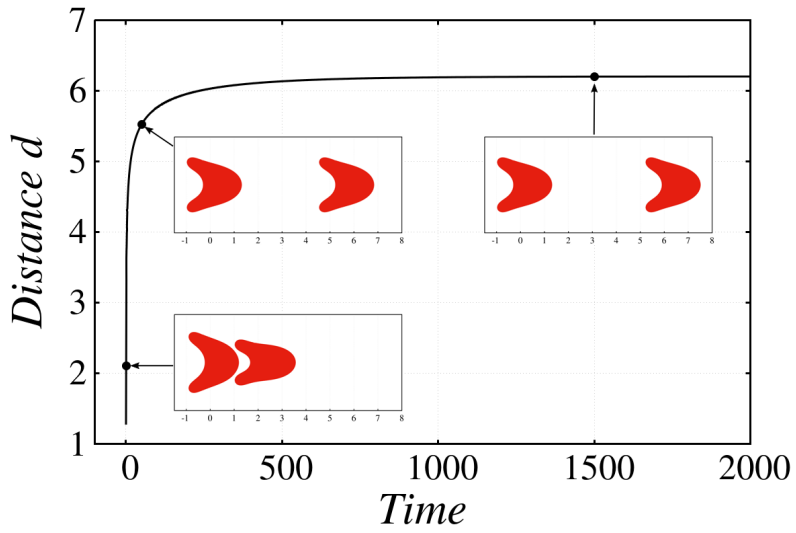

FIGURE 3.37: Distance d between two vesicles center of mass as function of time for $C_a = 10$ and $W = 4$.

Aouane et al. [128] found that the distance between two pair of vesicles is not affected by the capillary number, but rather related to the confinement. In a phase diagram (see Figure 3.38), they found the existence of a strong confinement region were the solution is unique (for $W < 12$), and a region of weak confinement were a stable solution merges with an unstable solution ($W \geq 12$).

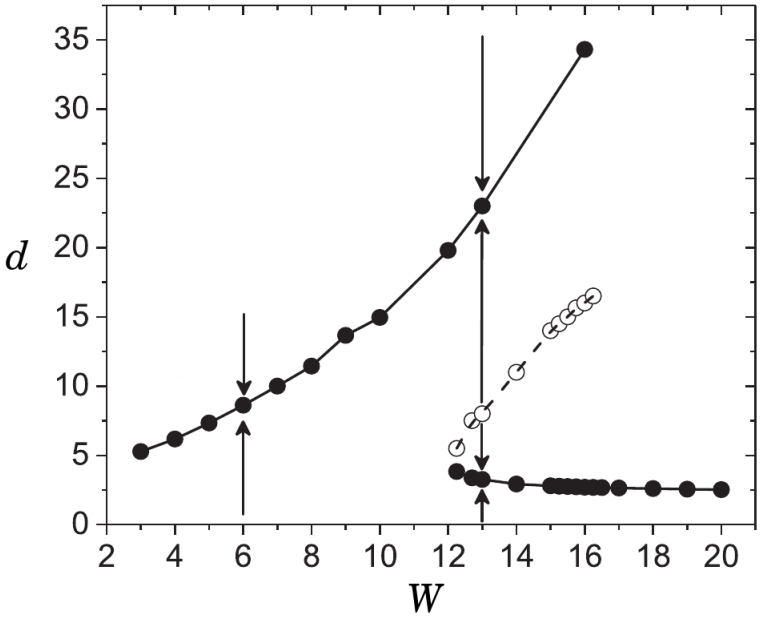

FIGURE 3.38: Distance d between two vesicles center of mass for different channel width W, figure from [128]

For small C_a the pairing dynamics of vesicles is different. Indeed, for weak flow strength, the vesicles will not adopt a stable shape instantaneously but will pass by a transition shape, as already shown in Figure 3.24.a, this leads to an interesting fact: two vesicles in the same flow conditions evolving with different shapes.
Figure 3.39 shows the distance between two vesicles for $C_a = 2.5$ and $C_n = 0.5(W = 4)$, the initial shape of the vesicles is a vertical ellipse, and the initial distance between their center of masses is set as $d_i = 0.2$, see Figure 3.40.a.

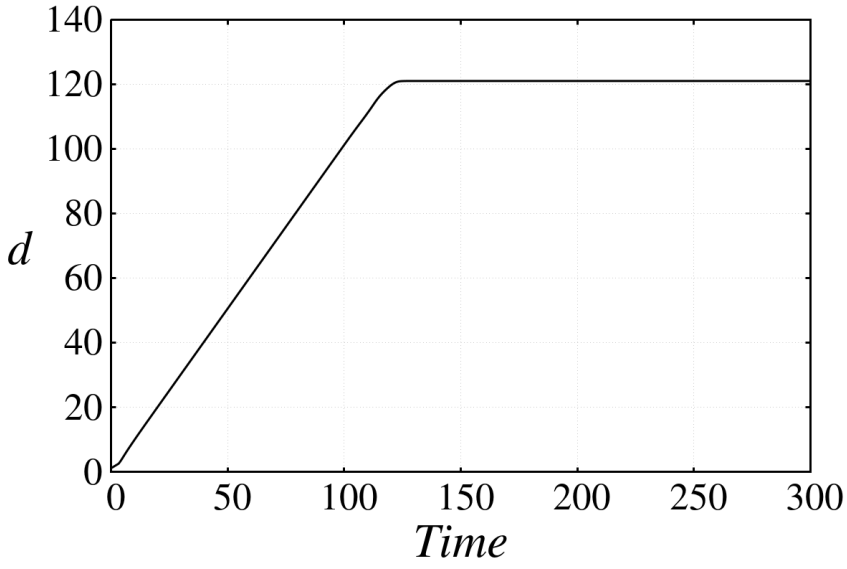

FIGURE 3.39: Distance d between two vesicles center of mass for $C_a = 2.5$ and $W = 4$ as function of time.

When initially the vesicles are close enough, their interaction make the first vesicle quickly adopt the parachute shape, while the second one evolve with a transition shape resembling to a peanut (Figure 3.40.b), after a certain time the second vesicle will also adopt the parachute shape (Figure 3.40.c) and the distance d will become constant.

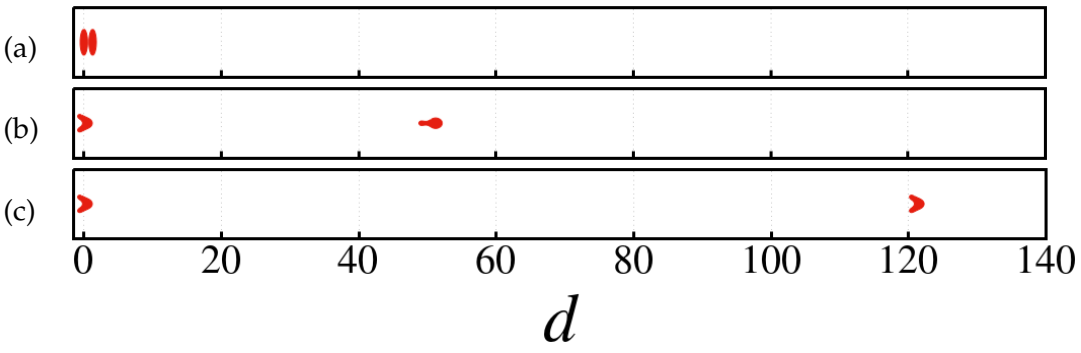

FIGURE 3.40: Corresponding vesicles shapes from Figure 3.39, (a) at time $t = 0$, (b) $t = 50$, and (c) at $t = 300$.

Figure 3.41 shows a comparison between the average velocity of the parachute (First vesicle) and the peanut-like (second vesicle) shape. As the peanut is much faster, it

will move far from the parachute, which explains this large distance d in Figure 3.39.

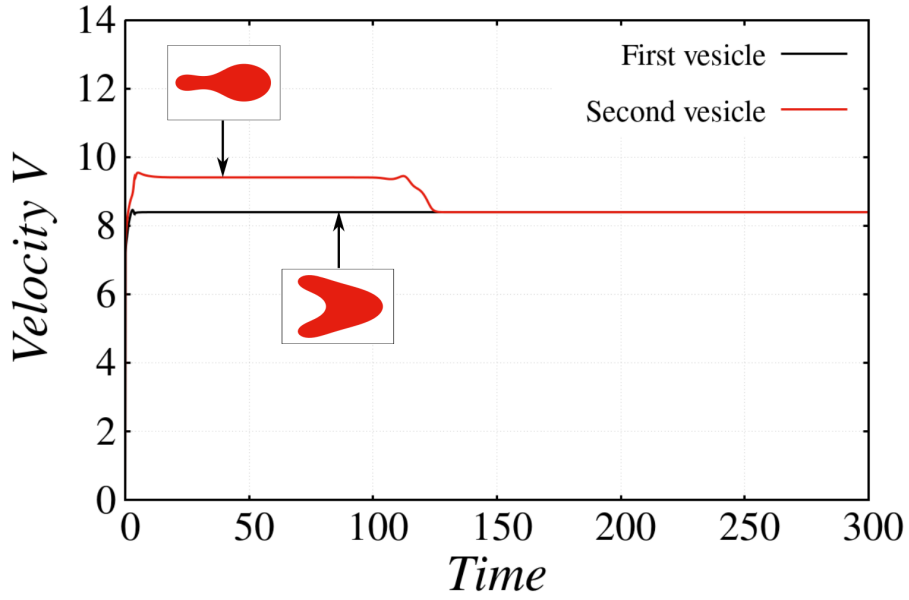

FIGURE 3.41: Comparison between the average velocity of a parachute and a peanut like for $C_a = 2.5$ and $W = 4$ (velocity is in unit of R_0/τ_B).

For an initial distance $d_i = 0.3$ and above, the vesicles will only interact with the surrounding fluid cause they are sufficiently far from each other. Consequently, they will form a cluster as shown in Figure 3.42.

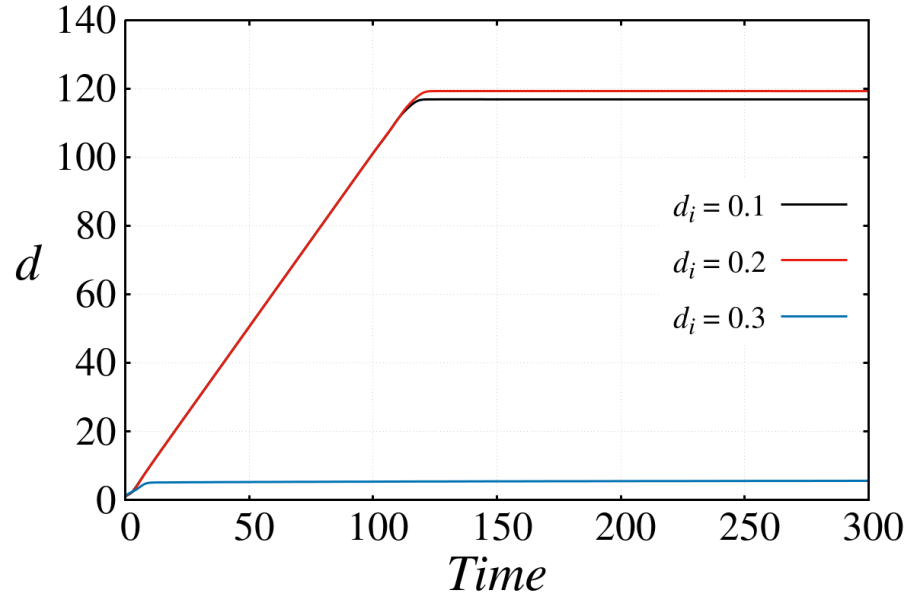

FIGURE 3.42: Distance between two vesicles for different initial distance d_i as function of time ($C_a = 2.5$ and $W = 4$).

We perturb now the imposed flow using the equation (3.8). For a strong C_a, the distance d between vesicles for the steady and the oscillating flow is invariant, cause

the vesicles will instantaneously adopt the parachute shape (see Figure 3.37), and they will oscillate in the same way. However, for a weak C_a, the flow oscillation will accelerate the migration of the second vesicle toward the parachute shape (as already discussed in Sec 3.4), which will affect the distance d between the pair of vesicles, as shown in Figure 3.43.

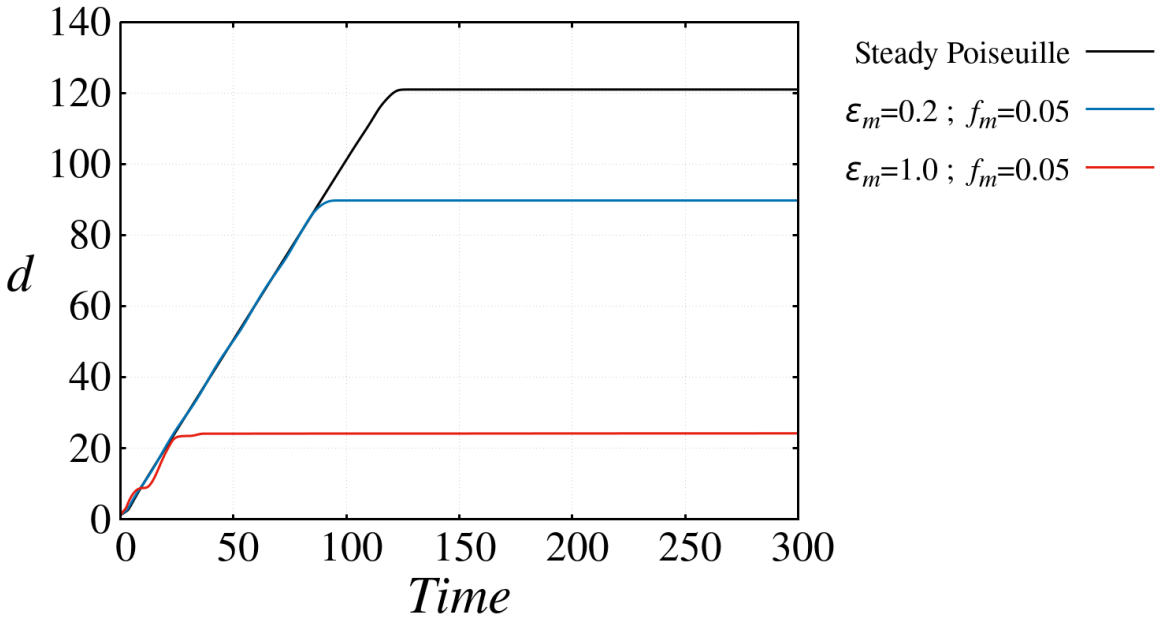

FIGURE 3.43: Distance d between two vesicles in oscillating flow for $C_a = 2.5$ and $W = 4$ as function of time, the initial distance is $d_i = 0.2$.

3.6 Conclusion

In shear flow, and without boundary effect (free-space flow), the vesicle shows three types of motion: (i) for a viscosity ratio λ equal one, the vesicle adopt a tank-treading (TT) motion, where the membrane rotates around the vesicle interior. (ii) Increasing the viscosity contrast, the vesicle starts to rotate periodically in the shear plane instead of only its membrane, this state is referred to as tumbling (TB). (iii) An intermediate regime between TT and TB called the vacillating-breathing (VB) is observed at a higher shear rate. In this state, the long axis of the vesicle oscillates about the flow direction. For a capsule in shear flow, and in addition the TT, TB and VB motions, the membrane can elongate with the direction of the flow. This deformation is captured with the so-called Taylor parameter and is proportional to the shear rate.

Next, we investigated the vesicle behavior in a confined Poiseuille, three types of shapes are found. (i) The symmetric shapes, where the vesicle center of mass always remains on the symmetry axis of the channel, like the parachute shape. (ii) The asymmetric shapes, where the center of mass is dispatched vertically, while the vesicle membrane shows a TT motion, like the slipper shapes. (iii) The oscillatory shapes, they correspond to a transition between symmetric and asymmetric shapes, and in which the vesicle shows an oscillatory motion like a swimmer flagella referred to as the snaking shape. The shapes are presented in a phase diagram as a

function of the capillary number C_a and the confinement C_n.

To characterize the oscillation of the snaking shape, we have studied the motion of the vesicle center of mass as a function of time, we have found that increasing the flow strength or the degree of confinement forces the vesicle to oscillate faster but with decreasing amplitude. The oscillations attenuate until the vesicle makes a transition to either a parachute or an off-centered snaking shape. We also investigated the effect of an oscillating flow on the vesicle shape using amplitude modulation of the applied Poiseuille flow. For the static shapes (parachute and slippers), when the imposed flow is not strong enough, the oscillation will accelerate the shape convergence from the initial to the final shape. On the other hand, for the snaking shape, when the modulation amplitude of the flow is large enough, a transition to static shapes is observed, and two regions of coexistence between the centered snaking and parachutes or with the unconfined slippers are found, as reported in the phase diagram on Figure 3.14. For small modulation amplitudes, the vesicle keeps oscillating but in a more complex manner. These results were published in APS journal [101].

For a pair of two vesicles, we investigated the distance between their respective center of masses as a function of time in steady and oscillating Poiseuille flow for fixed confinement and weak C_a. The case of a strong C_a for different channel width was already studied [128]. We found that the final distance is large, this is due to the fact that for weak flow the vesicle does not adopt its final shape instantaneously. By applying an oscillating flow, or by changing the initial distance, one can accelerate the vesicle shape convergence towards its stable form, and thus reduce this final distance.

Chapter 4

Flow fields

Content

4.1 Flow field for a single vesicle 67
4.1.1 Shear flow 67
4.1.2 Poiseuille flow 68
4.2 Flow field for two vesicles 71
4.2.1 Pair of parachute 71
4.2.2 Pair of slipper 71
4.3 Conclusion 72

The purpose of this chapter is to provide an overview of the flow field inside and outside the vesicle using streamline plot. The resultant flow field is a summation of the imposed flow and the flow induced by the presence of the vesicle. We first plot the streamline for a single vesicle in the shear flow with TT and TB motion, and in a Poiseuille flow for parachute, slipper and Snaking shapes. We also show the streamline for a pair of vesicles with a parachute and slipper shapes.

4.1 Flow field for a single vesicle

The boundary integral representation of the velocity field outside the membrane is given by Pozrikidis [22, p.141]. He considered that the force is discontinuous through the membrane. Therefore, he used two BIM expressions, one for the fluid inside the cell and the other one for the fluid outside the cell. In our simulation, we consider that the force is continuous through the membrane. Thus we only use one BIM expression for both fluids. The velocity field using BIM reads,

$$u_j(\mathbf{r}_0) = u_j^{\infty}(\mathbf{r}_0) - \frac{1}{4\pi\mu_{ext}} \int_C G_{ij}(\mathbf{r},\mathbf{r}_0)\, f_j(\mathbf{r})\ \mathrm{d}l(\mathbf{r}) + \frac{1-\lambda}{4\pi} \int_C u_i(\mathbf{r}) T_{ijk}(\mathbf{r},\mathbf{r}_0) n_k(\mathbf{r})\ \mathrm{d}l(\mathbf{r})\,, \tag{4.1}$$

where $u_j(\mathbf{r}_0)$ is the velocity at the point $\mathbf{r}_0$ due to the membrane forces $f_j(\mathbf{r})$. The point $\mathbf{r}_0$ can be inside or outside the cell domain. $G_{ij}(\mathbf{r},\mathbf{r}_0)$ and $T_{ijk}(\mathbf{r},\mathbf{r}_0)$ are the Green's functions for the Stokes flow, and $u_j^{\infty}(\mathbf{r}_0)$ is the velocity for the external flow. The integral is performed on the membrane contour C. Physically, the two integrals in the right-hand-side of (4.1) gives the flow field induced by the presence of the cell. The sum of the induced and the external flow[1] gives the resultant flow field, as shown in Figure 4.1.

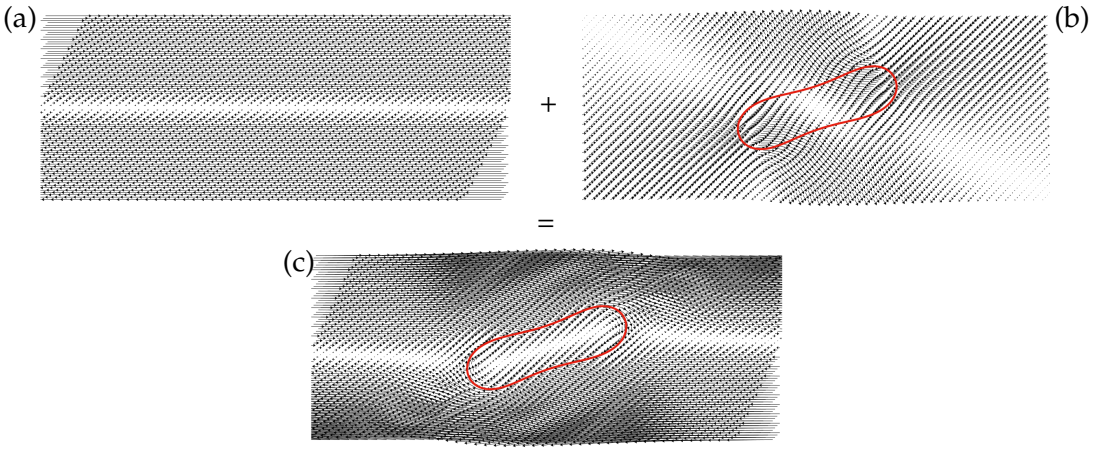

FIGURE 4.1: The flow field around a vesicle in TT motion. (a) The flow field for the external shear flow. (b) The flow field induced by the presence of the vesicle. (c) The summation of the external and the induced flow fields.

4.1.1 Shear flow

The streamlines of the resultant flow field for the TT motion is shown in Figure 4.2, where the inner fluid is rotational. The streamlines in Figures 4.3.a and 4.3.b shows a larger vortex, which is obviously, responsible of the TB motion of the vesicle.

[1] The external flow in all our illustrations is from left to right.

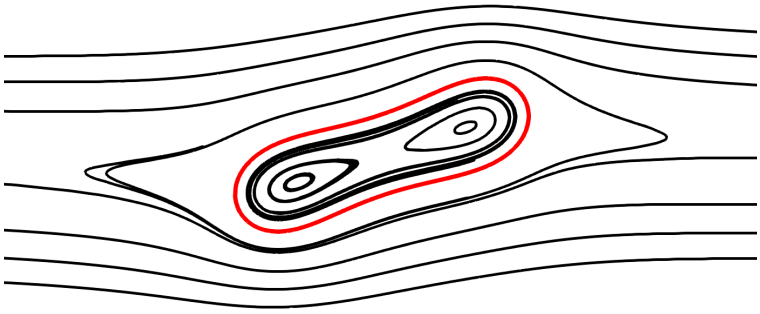

FIGURE 4.2: Streamlines for the fluid inside and outside the vesicle in the TT motion

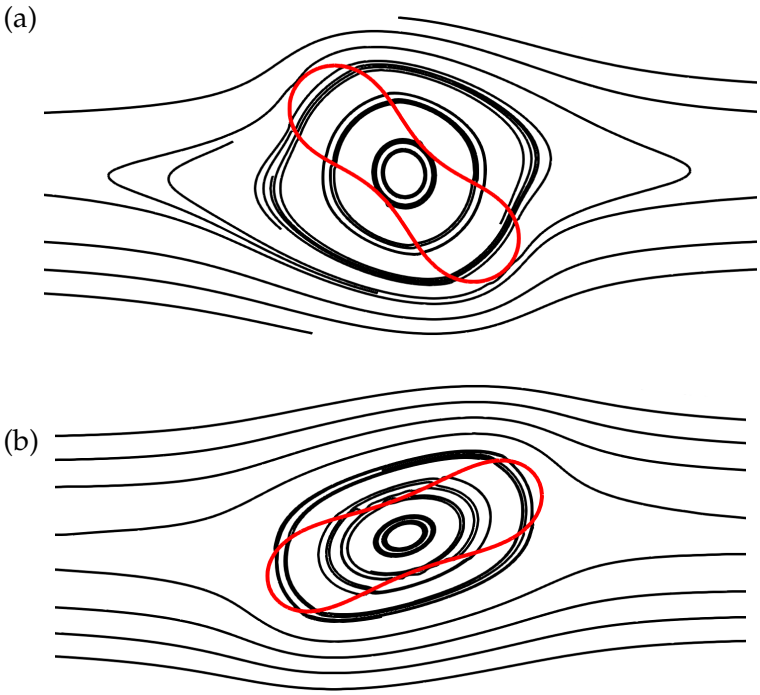

FIGURE 4.3: Streamlines for the fluid inside and outside the vesicle in the TB motion, (a) and (b) shows the TB motion.

4.1.2 Poiseuille flow

For the vesicle shapes in Poiseuille flow, the inner fluid is rotational in the case of the asymmetric slipper shapes (Figures 4.4.b and 4.4.c) where the membrane also shows a TT motion. But for the parachute shape, where the shape is symmetric to the axis of the channel, the inner fluid is irrotational (Figure 4.4.a).
The streamlines around RBCs can be recovered experimentally by following the trajectories of nanoparticles previously added to the flow as shown in Figure 4.4.b and Figure 4.4.e. Here an aqueous solution of Polyethylene glycol nanoparticles of 250 nm is mixed with healthy drawn blood sample previously washed with PBS to prevent the aggregation of RBCs. The prepared solution is then pumped into a rectangular channel of few microns mimicking capillaries, with different velocities in order to obtain different shapes of RBCs. The particles are detected on every frame using

the LoG (Laplacian of a Gaussian) filter after subtracting the background. Combining these filtered images, we obtain the particle's trajectory which also shows the streamline around the cells.
The nanoparticles trajectories (colored curves) in Figures 4.4.b and 4.4.e are in agreement with the streamlines from our simulations in Figures 4.4.a, 4.4.c, and 4.4.d.

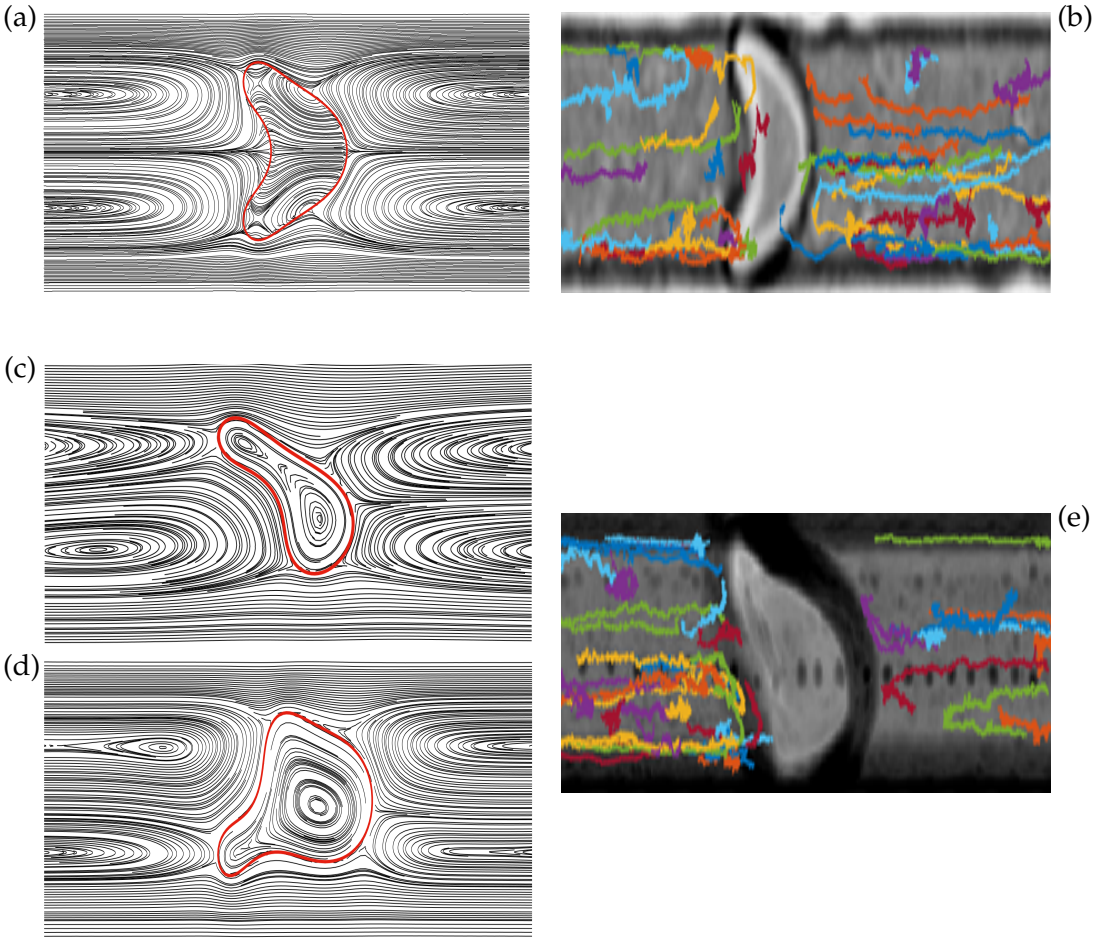

FIGURE 4.4: Streamlines from simulations for the fluid inside and outside the vesicle. (a) For parachute shape. (c) For unconfined slipper. (d) For confined slipper. (b)-(e) Red blood cell with respectively, the parachute, and the unconfined slipper shape. The colors show the nanoparticles trajectories (experiments by F. Yaya).

The Figures 4.5.a-e show the streamlines for the CSn shape motion in one period of oscillation.

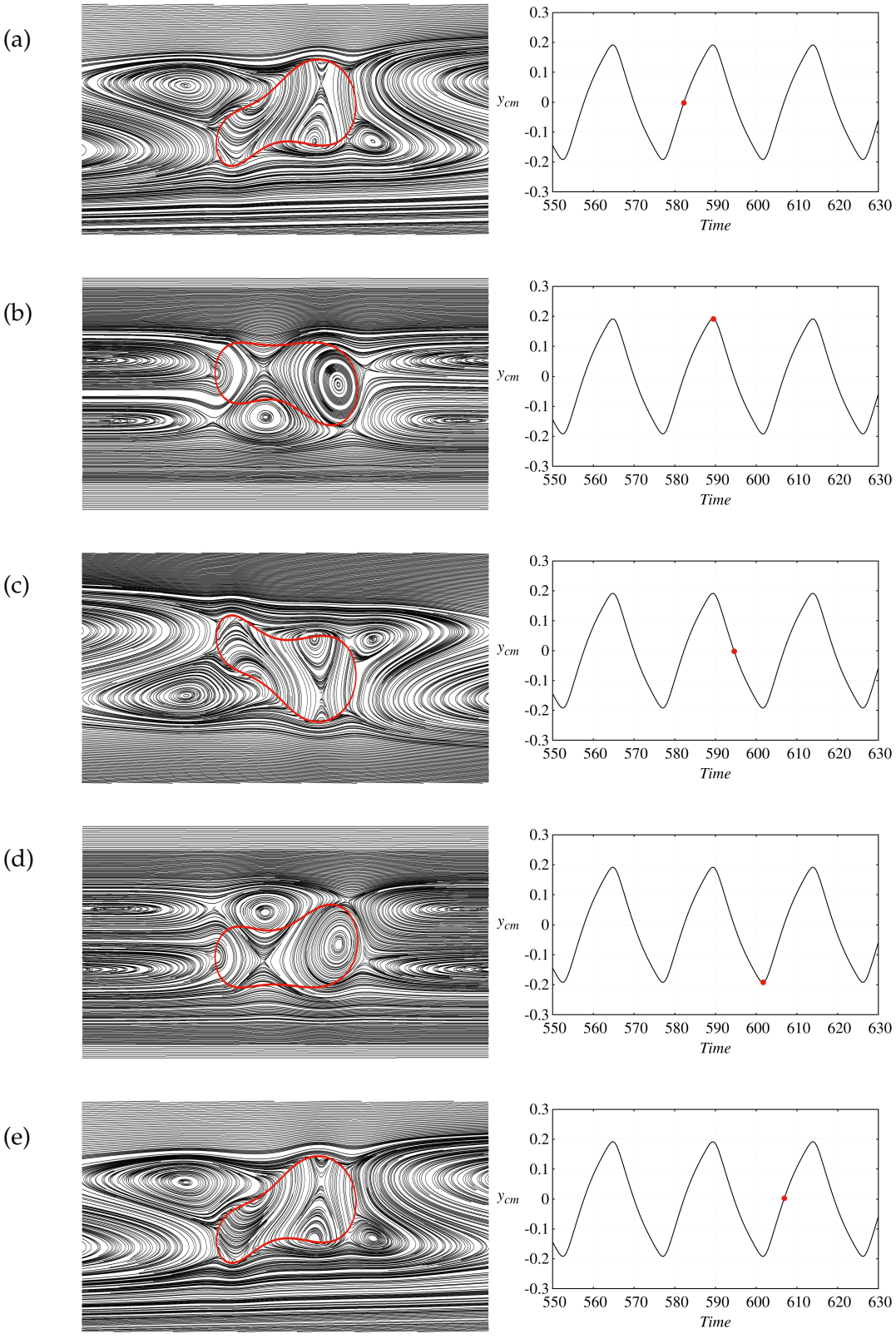

FIGURE 4.5: Streamlines for the fluid inside and outside the vesicle for one oscillation period of the CSn shape (from (a) to (e)).

4.2 Flow field for two vesicles

4.2.1 Pair of parachute

The flow field between and around a pair of two vesicles is obtained by solving the equation (3.17) for the fluid domain inside and outside the membrane of the vesicles. For $C_a = 10$ and $W = 4$, Figure 4.6 shows the streamlines induced by the pair and Figure 4.7 shows the sum of the induced flow with the imposed Poiseuille flow.

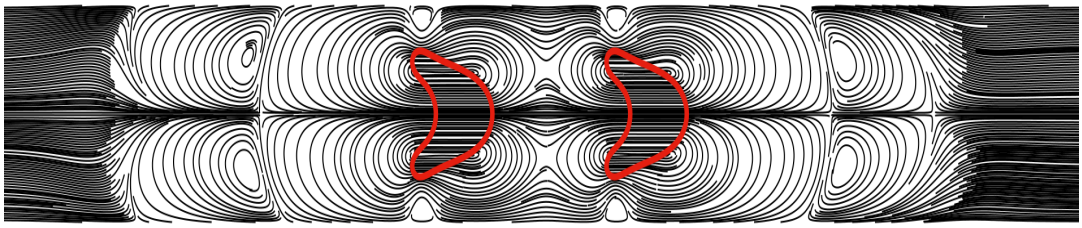

FIGURE 4.6: Streamlines for the fluid inside and outside induced by the presence of the vesicles pair with parachute shape.

(a) 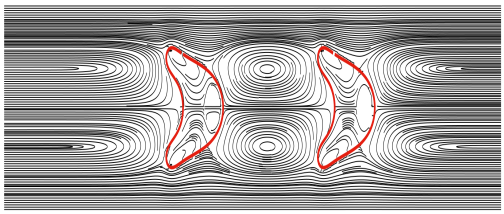  (b)

FIGURE 4.7: (a) Streamlines of the flow field for 2 vesicles in Poiseuille flow, (b) nanoparticles trajectory showing the streamline around two red blood cells in microfluidic channel (experiment by F.Yaya).

The streamlines of the resultant flow profile are similar to the single parachute shape in Figures 4.4.a and 4.4.b, except that in between the two vesicles, two vortices symmetric to the center axis of the channel are formed. These vortices were also observed experimentally (Figure 4.4.a) by following the nanoparticles trajectories. Several studies also reported the formation of vortices between neighboring cells when clusters are formed [129, 128].

4.2.2 Pair of slipper

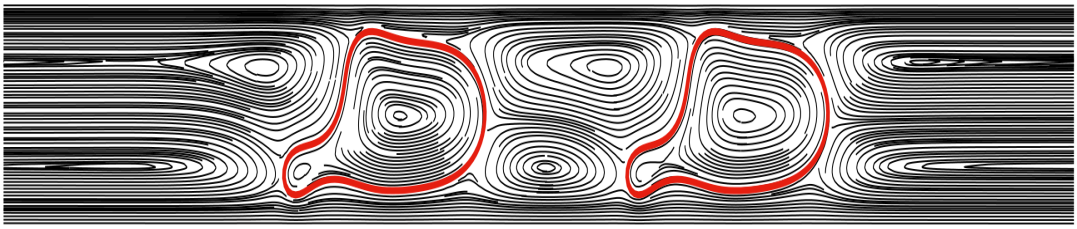

FIGURE 4.8: Streamlines of the resultant flow field for the fluid inside and outside a pair of confined slippers shape.

Decreasing the channel width to $W = 2$ and using the same capillary number $C_a = 10$, the pair of parachutes become a pair of confined slipper. In Figure 4.8, we plot the streamline for the resultant flow field, we observe that the two vortices are not symmetric with respect to the channel axis, unlike the vortices between the pair of parachutes.

4.3 Conclusion

We investigated in this chapter the flow field inside and outside a single and a pair of vesicles using a streamline plot. we observed that for the TT motion in shear or Poiseuille flow the interior liquid is rotational. Unlike the TT motion, in TB motion the fluid outside is also rotational. We have also observed two symmetric vortices or eddies with respect to the channel axis for a pair of parachutes, but the two eddies become asymmetric when the pair adopt asymmetric shapes like slippers. These results simulations were in good agreement with experimental results.

Conclusion & perspectives

The main functions of blood are to supply oxygen, nutrients, and other substances to all of the body's tissues and organs, as well as to remove waste products. It consists of plasma, white blood cells (leukocytes), platelets, and red blood cells (RBCs). The latter constitute about 98% of these blood components, and consequently, have the largest influence on its mechanical properties. RBC is a highly flexible cell made of a membrane surrounding a hemoglobin solution. The membrane is a fluid bilayer of phospholipids and has various membrane-integrated proteins distributed on it. The blood supplies oxygen, nutrients, and other substances through a circulatory system made of vessels of different sizes and properties.
Due to the complexity of the RBC membrane simplified models like capsules, and vesicles are used to mimic the behavior of RBCs, both in simulations and in experiments. The main difference between these two models is their extensibility. In the case of the capsule, the membrane can be extensible depending on the fabrication process, unlike the vesicles. In the absence of external flow, RBCs assume a discocyte shape, where the swelling ratio is around $\nu = 0.65$ (see Figure 2.2). In the presence of external flow, four relevant energy contributions can be identified: (i) Local in-plane, and (ii) out of plane energies, respectively called stretching and bending energies. (iii) Constraint energy used to impose volume and surface conservation. (iv) The energy acting between pairs of membranes or membranes and walls, but are not part of the membrane model itself. The membrane model is formulated in such a way that any deviation from the equilibrium shape increases the membrane energy and response forces are induced which drive the membrane shape towards a new equilibrium shape. Constitutive laws like Helfrich or Skalak are adopted for the bending and the stretching energies. At the scale of cells, the inertial forces of the internal and external flows are negligible compared to the viscous forces, and consequently, the fluid flow can be modeled by the Stokes equation. Using dimensional analysis for the Stokes equation and membrane forces, that can be derived from membrane energies, the system of equations can be described with dimensionless quantities. The capillary number C_a, and the tension number C_T are used for the vesicle model, and the dimensionless shear rate C_s, and the reduced ratio of bending C_e for the capsule model. Another dimensionless parameter, which is used in the case of a cell confined between two walls, is the confinement number C_n. In order to solve the fluid-membrane interaction numerically, two approaches can be used. In the first one, called the boundary element method, the fluid and the membrane dynamics are brought together under a single formulation using Green's functions and the Lorentz reciprocal theorem. The boundary effects are included using the image system method [95]. In the second approach, called the immersed boundary method, the fluid and the membrane dynamics are solved in two separated grids, then the interactions between the fluid and the membrane grid are computed using an approximated Dirac delta function.
In shear flow, the vesicle shows three types of motion. For a viscosity ratio λ equal one, the vesicle adopts a tank-treading (TT) motion, where the membrane rotates

around the interior of the vesicle. Increasing the viscosity contrast, the vesicle starts to rotate periodically, this state is referred to as tumbling (TB). At a higher shear rate, an intermediate motion between TT and TB called the vacillating-breathing (VB) is observed, where the long axis of the vesicle oscillates about the flow direction. For a capsule in shear flow, and in addition to the TT, TB and VB motions, the membrane can elongate with the direction of the flow. This deformation is captured with the so-called Taylor parameter and is proportional to the shear rate. For a healthy RBC, the Taylor parameter is around 0.4.
Next, we focused on the vesicle behavior in a confined Poiseuille, to mimic RBC flow in capillaries. The vesicle model was chosen for its membrane inextensibility, for sake of simplicity. Three types of shapes are found: (i) Symmetric shapes, like the parachute shape, where the vesicle center of mass always remains on the symmetry axis of the channel. (ii) Asymmetric shapes, like the slipper shape, where the center of mass is dispatched vertically, while the vesicle membrane shows a TT motion. (iii) Oscillatory shapes, which correspond to a transition between symmetric and asymmetric shapes, in which the vesicle shows an oscillatory motion like a swimmer flagella, referred to as the snaking shape. The shapes were presented in a phase diagram as a function of the capillary number C_a and the confinement C_n.
In order to understand the behavior of the snaking shape, we have studied the motion of the vesicle center of mass as a function of time. We found that an increase of either the flow strength or the degree of confinement forces the vesicle to oscillate faster but with decreasing amplitude. The oscillations attenuate until the vesicle makes a transition to either a parachute or an off-centered snaking shape. We also investigated the effect of an oscillating flow on the vesicle shape using amplitude modulation of the applied Poiseuille flow to mimic the pulsatile flow in the human circulatory system. For the parachute and slipper shapes, when the imposed flow is not strong enough, the oscillation will accelerate the shape convergence from the initial to the final shape. On the other hand, for the snaking shape, when the modulation amplitude of the flow is large enough, transitions to static shapes are observed, and two regions of coexistence between the centered snaking and parachutes or with the unconfined slippers are found (see Figure 3.14). For small modulation amplitudes, the vesicle keeps oscillating but in a more complex manner.
For the case of two interacting vesicles, we investigated the pair distance as a function of time in steady and oscillating Poiseuille flow for a fixed C_n and weak C_a. We found that the final distance is large. This is due to the fact that for weak flow the vesicle does not adopt its final shape instantaneously. By applying an oscillating flow, or by changing the initial distance, one can accelerate the vesicle shape convergence towards its stable form, and thus reduce this final distance.
We have also investigated the flow field inside and outside a single and pair of vesicle using a streamline plot. We have observed that for the TT motion in shear or Poiseuille flow the interior liquid is rotational. Unlike the TT motion, in TB motion the fluid outside is also rotational. We also have shown two symmetric vortex or eddies with respect to the channel axis for a pair of parachutes, but the two eddies become asymmetric when the pair adopt asymmetric shapes like slippers.
It remains a lot to do. In the first place, a three-dimensional study of the vesicle behavior in confined Poiseuille flow is necessary to complete our understanding. It will also be interesting to study the snaking shape motion as a function of the viscosity, or in a confined Poiseuille flow with deformable boundaries. We can also investigate the snaking shape behavior with stretching energy in addition to the bending and the constraint energies. The simulation of more than two vesicles in steady and oscillating Poiseuille flow may show some interesting behavior.

Appendices

Appendix A

Free-space Green's function for steady Stokes flow

Several methods can be used to determine the Green's function for the steady Stokes flow of an incompressible fluid. For example, using the Fourier transform proprieties [130, p.20], or simply using some vector analysis [131, p.241]. Here, we use the approach proposed by Pozrikidis [22, p.22] to derive the Green's function for a two-dimensional unbounded Stokes flow, also referred to as the free-space Green's function.
First, we rewrite the singularly forced Stokes equation (2.49), and the continuity equation,

$$-\nabla p + \mu\,\nabla^2\mathbf{u} + \mathbf{f}\,\delta(\mathbf{r}-\mathbf{r}_0) = \nabla\sigma + \mathbf{f}\,\delta(\mathbf{r}-\mathbf{r}_0) = 0\,, \tag{A.1}$$

$$\nabla\mathbf{u} = 0\,. \tag{A.2}$$

Introducing the divergence in (A.1), and using the continuity equation, we get,

$$\begin{aligned} \nabla(\nabla p) - \mu\,\nabla(\Delta\mathbf{u}) &= \nabla(\mathbf{f}\,\delta(\hat{\mathbf{r}})) \\ \Delta p - \mu\,\Delta(\nabla\mathbf{u}) &= \delta(\hat{\mathbf{r}})\nabla(\mathbf{f}) + \mathbf{f}\,\nabla(\delta(\hat{\mathbf{r}})) \\ \Delta p &= \delta(\hat{\mathbf{r}})\nabla(\mathbf{f}) + \mathbf{f}\,\nabla(\delta(\hat{\mathbf{r}}))\,, \end{aligned} \tag{A.3}$$

where $\hat{\mathbf{r}} = \mathbf{r} - \mathbf{r}_0$ and $\mathbf{f}$ is a constant that only shows the strength and the direction of a point force placed at the point $\mathbf{r}_0$. Consequently $\nabla\mathbf{f} = 0$, then (A.3) becomes,

$$\Delta p = \mathbf{f}\,\nabla(\delta(\hat{\mathbf{r}}))\,, \tag{A.4}$$

The equation in (A.4) is similar to Laplace equation ($\Delta\phi(x) = 0$), which also satisfy,

$$\Delta\phi(x) = -\delta(\hat{x})\,, \tag{A.5}$$

ϕ vanish at the infinity, and has as fundamental solution,

$$\phi(x) = \begin{cases} -\dfrac{1}{2\pi}\ln(x) & \text{for 2D} \\[2ex] \dfrac{1}{4\pi x} & \text{for 3D.} \end{cases} \tag{A.6}$$

Using the two-dimensional solution of Laplace equation in (A.6), the equation (A.4) becomes,

$$\begin{aligned}\Delta p &= \frac{1}{2\pi}\,\mathbf{f}\,\nabla\left[\Delta \ln(\hat{\mathbf{r}})\right] = \frac{1}{2\pi}\,\mathbf{f}\,\Delta\left[\nabla \ln(\hat{\mathbf{r}})\right] \\ &= \frac{1}{2\pi}\,\mathbf{f}\,\Delta\left[\nabla \ln(\mid \hat{\mathbf{r}} \mid)\right]\,,\end{aligned} \tag{A.7}$$

where $\hat{r} = \mid \hat{\mathbf{r}} \mid = \mid \mathbf{r} - \mathbf{r}_0 \mid = \sqrt{(r-r_0)_i^2 + (r-r_0)_j^2}$. For three-dimensional case, one can use the fundamental solution of Laplace equation in 3D case and follow the same steps as described below.

Integrating (A.7) we obtain,

$$p = \frac{1}{2\pi}\,\mathbf{f}\,\nabla\left[\ln(\hat{\mathbf{r}})\right] + \zeta(\mathbf{r})\,. \tag{A.8}$$

Using the condition that the pressure vanishes in the infinity (similarly to Laplace equation), we have,

$$\lim_{r\to\infty} p = \frac{1}{2\pi}\,\mathbf{f}\,\lim_{r\to\infty}\frac{\nabla\hat{\mathbf{r}}}{\hat{\mathbf{r}}} + \lim_{r\to\infty}\zeta(\mathbf{r}) = 0\,, \tag{A.9}$$

which implies that $\zeta \equiv 0$, and we obtain,

$$p = \frac{1}{2\pi}\,\mathbf{f}\,\nabla\left[\ln(\hat{\mathbf{r}})\right]\,, \tag{A.10}$$

Now deriving (A.10), where $\nabla = \frac{\partial}{\partial x_i} + \frac{\partial}{\partial x_j}$ and $\hat{\mathbf{r}} = \sqrt{\hat{r}_i^2 + \hat{r}_j^2}$, we obtain,

$$p = \frac{1}{4\pi}\left(2\frac{\hat{\mathbf{r}}}{\hat{\mathbf{r}}^2}\right)\,\mathbf{f} = \frac{1}{4\pi}\mathbf{g}\,\mathbf{f}\,, \tag{A.11}$$

$\mathbf{g}$ is called the pressure vector, and also referred to as the free-space Green's function for the pressure, in Einstein notation it gives,

$$p = \frac{1}{4\pi} g_j(\mathbf{r},\mathbf{r}_0)\; f_j\,, \tag{A.12}$$

where,

$$g_j(\mathbf{r},\mathbf{r}_0) = 2\frac{\hat{r}_j}{\hat{\mathbf{r}}^2}\,. \tag{A.13}$$

Now we consider the biharmonic equation $\Delta(\Delta\psi) = \Delta\phi = 0$, which will also satisfy,

$$\Delta(\Delta\psi) = -\delta(\hat{\mathbf{r}})\,. \tag{A.14}$$

Substituting (A.14) into (A.4), and using (A.5), we get,

$$p = -\mathbf{f}\,\nabla\phi = -\mathbf{f}\,\nabla(\Delta\psi) = -\mathbf{f}\,\Delta(\nabla\psi)\,. \tag{A.15}$$

Now substituting (A.15), and (A.14) into the Stokes equation (A.1), we obtain,

$$\mathbf{u} = -\frac{\mathbf{f}}{\mu}(\nabla\nabla - \mathbb{1}\Delta)\psi\,. \tag{A.16}$$

It remains now to find a solution for ψ by solving $\Delta\psi = \phi = -1/2\pi \ln(\hat{\mathbf{r}})$.

Considering $\hat{\mathbf{r}}$ in polar coordinate system $(\mathbf{e}_r, \mathbf{e}_\theta)$, the Laplacian of ψ reads then,

$$\Delta\psi = \frac{\partial^2\psi}{\partial\mathbf{r}^2} + \frac{1}{\hat{\mathbf{r}}}\frac{\partial\psi}{\partial\mathbf{r}} + \frac{1}{\hat{\mathbf{r}}^2}\frac{\partial^2\psi}{\partial\theta^2} = -\frac{1}{2\pi}\ln(\hat{\mathbf{r}})\,. \tag{A.17}$$

As ψ is independent of θ we obtain,

$$\begin{aligned}\Delta\psi = \frac{\partial^2\psi}{\partial\mathbf{r}^2} + \frac{1}{\hat{\mathbf{r}}}\frac{\partial\psi}{\partial\mathbf{r}} &= \psi'' + \frac{1}{\hat{\mathbf{r}}}\psi' \\ &= -\frac{1}{2\pi}\ln(\hat{\mathbf{r}})\,.\end{aligned} \tag{A.18}$$

Rearranging now (A.18),

$$\left(\hat{\mathbf{r}}\psi'\right)' = -\frac{\hat{\mathbf{r}}}{2\pi}\ln(\hat{\mathbf{r}})\,. \tag{A.19}$$

Integrating[1] twice from both sides we obtain,

$$\psi(\hat{\mathbf{r}}) = \frac{\hat{\mathbf{r}}^2}{8\pi}(1 - \ln(\hat{\mathbf{r}})) + C_1\ln(\hat{\mathbf{r}}) + C_2\,. \tag{A.20}$$

Using the condition that ψ must vanish at the infinity and the equation (A.14), we find that the constant C_1 and C_2 are equal to zero, we obtain,

$$\psi(\hat{\mathbf{r}}) = \frac{\hat{\mathbf{r}}^2}{8\pi}(1 - \ln(\hat{\mathbf{r}}))\,. \tag{A.21}$$

Substituting (A.21) into (A.16), and after some straight forward algebra we have finally,

$$\begin{aligned}\mathbf{u} &= \frac{1}{4\pi\mu}\mathbf{f}\left[\nabla\nabla(\frac{\hat{\mathbf{r}}^2}{2}(\ln\hat{\mathbf{r}} - 1)) - \mathbb{1}\Delta(\frac{\hat{\mathbf{r}}^2}{2}(1 - \ln\hat{\mathbf{r}}))\right] \\ &= \frac{1}{4\pi\mu}\left[-\mathbb{1}\ln(\hat{\mathbf{r}}) + \frac{\hat{\mathbf{r}}\hat{\mathbf{r}}}{\hat{\mathbf{r}}^2}\right]\mathbf{f} \\ &= \frac{1}{4\pi\mu}\mathbf{G}(\hat{\mathbf{r}})\mathbf{f}\,.\end{aligned} \tag{A.22}$$

Using Einstein notation we obtain,

$$u_i = \frac{1}{4\pi\mu}G_{ij}(\mathbf{r}, \mathbf{r}_0)f_j\,, \tag{A.23}$$

where $G_{ij}(\mathbf{r}, \mathbf{r}_0)$ is the free-space Green function for the velocity, also called the stokeslet, or the first Oseen-Burgers tensor, and given by,

$$G_{ij}(\mathbf{r}, \mathbf{r}_0) = -\delta_{ij}\ln(\hat{\mathbf{r}}) + \frac{\hat{r}_i\hat{r}_j}{\hat{\mathbf{r}}^2}\,. \tag{A.24}$$

[1] $\hat{\mathbf{r}} = \mathbf{r} - \mathbf{r}_0$, where $\mathbf{r}$ is variable and $\mathbf{r}_0$ is constant. The first and the second integral of (A.19) is then

$$\int\left[(\mathbf{r} - \mathbf{r}_0)\,\psi'\right]'\mathrm{d}\mathbf{r} = -\frac{1}{2\pi}\int(\mathbf{r} - \mathbf{r}_0)\ln(\mathbf{r} - \mathbf{r}_0)\,\mathrm{d}\mathbf{r}$$

$$\int\psi' dr = \int\left[-\frac{1}{4\pi}\hat{\mathbf{r}}\ln(\hat{\mathbf{r}}) + \frac{1}{8\pi}\hat{\mathbf{r}} + \frac{C_1}{\hat{\mathbf{r}}}\right]\mathrm{d}\mathbf{r}$$

Now we consider the stress tensor for a Newtonian fluid,

$$\sigma_{ik} = -p\delta_{ik} + \mu \left(\frac{\partial u_i}{\partial x_k} + \frac{\partial u_k}{\partial x_i} \right) . \tag{A.25}$$

Substituting (A.12), and (A.23) into (A.25) we obtain,

$$\begin{aligned} \sigma_{ik} &= \frac{1}{4\pi} \left[-\delta_{ik}\, g_j(\mathbf{r}, \mathbf{r}_0) + \frac{\partial G_{ij}(\mathbf{r}, \mathbf{r}_0)}{\partial x_k} + \frac{\partial G_{ik}(\mathbf{r}, \mathbf{r}_0)}{\partial x_i} \right] f_j \\ &= \frac{1}{4\pi} T_{ijk}(\mathbf{r}, \mathbf{r}_0)\, f_j \,, \end{aligned} \tag{A.26}$$

where,

$$T_{ijk}(\mathbf{r}, \mathbf{r}_0) = -\delta_{ik}\, g_j(\mathbf{r}, \mathbf{r}_0) + \frac{\partial G_{ij}(\mathbf{r}, \mathbf{r}_0)}{\partial x_k} + \frac{\partial G_{ik}(\mathbf{r}, \mathbf{r}_0)}{\partial x_i} . \tag{A.27}$$

Substituting now (A.13) and (A.24) into (A.27), and after some algebra, we obtain the free-space Green function for the stress field, also called the stresslet, or the second Oseen-Burgers tensor,

$$T_{ijk}(\mathbf{r}, \mathbf{r}_0) = -4 \frac{\hat{r}_i\, \hat{r}_j\, \hat{r}_k}{\hat{\mathbf{r}}^4} . \tag{A.28}$$

Appendix B

Boundary integral representation of unbounded steady Stokes flow

To develop the boundary integral formulation for steady Stokes flow we proceed in 3 steps. (i) First, we define the Green second identity. (ii) We introduce the free-space Green's functions for a two-dimensional steady Stokes flow. (iii) And finally, we derive the integral representation using the divergence theorem. More details can be found in [22, p.19], and [132, p.161].

Green's second identity

Let us consider two unrelated Newtonian and incompressible fluids. The associated velocity fields are $\mathbf{u}$ and $\mathbf{u}'$, the stress tensors are σ, σ' and the pressures are P and P'. Whence,

$$\begin{aligned}\mathbf{u}' \cdot (\nabla\sigma) = u_i' \frac{\partial \sigma_{ij}}{\partial x_j} &= \frac{\partial}{\partial x_j}\left(u_i' \sigma_{ij}\right) - \sigma_{ij}\frac{\partial u_i'}{\partial x_j} \\ &= \frac{\partial}{\partial x_j}\left(u_i' \sigma_{ij}\right) - \frac{\partial u_i'}{\partial x_j}\left[-p\delta_{ij} + \mu\left(\frac{\partial u_i}{\partial x_j} + \frac{\partial u_j}{\partial x_i}\right)\right] \\ &= \frac{\partial}{\partial x_j}\left(u_i' \sigma_{ij}\right) + p\frac{\partial(\delta_{ij}u_i')}{\partial x_j} - \mu\left(\frac{\partial u_i}{\partial x_j} + \frac{\partial u_j}{\partial x_i}\right)\frac{\partial u_i'}{\partial x_j},\end{aligned} \tag{B.1}$$

where δ_{ij} is the Kronecker function ($\delta_{ij} = 1$ if $i = j$, and $\delta_{ij} = 0$ if $i \neq j$) and μ the fluid viscosity. Invoking the Kronecker's delta function definition $u_i'\delta_{ij} = u_j'$ and using the continuity equation $\partial u_j'/\partial x_j = 0$ to eliminate the pressure term in (B.1), we obtain the Green's first identity counterpart,

$$u_i' \frac{\partial \sigma_{ij}}{\partial x_j} = \frac{\partial}{\partial x_j}\left(u_i' \sigma_{ij}\right) - \mu\left(\frac{\partial u_i}{\partial x_j} + \frac{\partial u_j}{\partial x_i}\right)\frac{\partial u_i'}{\partial x_j}. \tag{B.2}$$

Switching the roles of $\mathbf{u}$ and $\mathbf{u}'$ we obtain,

$$u_i \frac{\partial \sigma_{ij}'}{\partial x_j} = \frac{\partial}{\partial x_j}\left(u_i \sigma_{ij}'\right) - \mu\left(\frac{\partial u_i'}{\partial x_j} + \frac{\partial u_j'}{\partial x_i}\right)\frac{\partial u_i}{\partial x_j}. \tag{B.3}$$

Subtracting now (B.2) from (B.3), we obtain the Green second identity counterpart,

$$\frac{\partial}{\partial x_j}\left(u_i'\sigma_{ij} - u_i\sigma_{ij}'\right) = u_i'\frac{\partial \sigma_{ij}}{\partial x_j} - u_i\frac{\partial \sigma_{ij}'}{\partial x_j}\,. \tag{B.4}$$

In the absence of body force ($\nabla\sigma = 0$), the right-hand side term in (B.4) vanishes, yielding to the Lorentz reciprocal relation,

$$\frac{\partial}{\partial x_j}\left(u_i'\sigma_{ij} - u_i\sigma_{ij}'\right) = 0\,. \tag{B.5}$$

The Lorentz reciprocal relation (and the second Green's identity) allow us to construct a solution for the desired flow without solving the equations of motion, just by using information of another flow.

Free-space Green's function

The pressure, the stress, and the velocity field due to a point force located at r_0 can be expressed in terms of the stokeslet $\mathbf{G}(\mathbf{r}, \mathbf{r_0})$, the stresslet $\mathbf{T}(\mathbf{r}, \mathbf{r_0})$, and the pressure vector $\mathbf{g}(\mathbf{r}, \mathbf{r_0})$ (see appendix A) as,

$$u_i(\mathbf{r}) = \frac{1}{4\pi\mu}G_{ij}(\mathbf{r}, \mathbf{r}_0)f_j, \qquad p(\mathbf{r}) = \frac{1}{4\pi}g_j(\mathbf{r}, \mathbf{r}_0)f_j, \qquad \sigma_{ik}(\mathbf{r}) = \frac{1}{4\pi}T_{ijk}(\mathbf{r}, \mathbf{r}_0)f_j, \tag{B.6}$$

where the associated free-space Greens function are given by,

$$G_{ij}(\mathbf{r}, \mathbf{r}_0) = -\delta_{ij}\ln(|(\mathbf{r} - \mathbf{r}_0)|) + \frac{(r - r_0)_i(r - r_0)_j}{|\mathbf{r} - \mathbf{r}_0|^2}\,, \tag{B.7}$$

$$T_{ijk}(\mathbf{r}, \mathbf{r}_0) = -4\,\frac{(r - r_0)_i(r - r_0)_j(\mathbf{r} - \mathbf{r}_0)_k}{|\mathbf{r} - \mathbf{r}_0|^4}\,, \tag{B.8}$$

$$g_j(\mathbf{r}, \mathbf{r}_0) = 2\frac{(r - r_0)_j}{|\mathbf{r} - \mathbf{r}_0|^2}\,. \tag{B.9}$$

The Greens function must satisfy the Stokes equation in (B.10), and the continuity equation in (B.11),

$$\begin{aligned} -\frac{\partial p_j(\mathbf{r})}{\partial x_i} + \nabla^2 G_{ij}(\mathbf{r}, \mathbf{r}_0) + 4\pi\,\delta_{ij}\,\delta(\mathbf{r} - \mathbf{r}_0) = 0\,, \\ \frac{\partial T_{ijk}(\mathbf{r}, \mathbf{r}_0)}{\partial x_k} + 4\pi\,\delta_{ij}\,\delta(\mathbf{r} - \mathbf{r}_0) = 0\,, \end{aligned} \tag{B.10}$$

$$\frac{\partial G_{ij}(\mathbf{r}, \mathbf{r}_0)}{\partial x_i} = 0\,. \tag{B.11}$$

Using the expressions in (B.6), the Lorentz reciprocal identity in (B.5) can be written,

$$\frac{\partial}{\partial x_k}\left[G_{ij}(\mathbf{r}, \mathbf{r}_0)\;\sigma_{ik}(\mathbf{r}) - \mu\;u_i(\mathbf{r})\;T_{ijk}(\mathbf{r}, \mathbf{r}_0)\right] = 0\,. \tag{B.12}$$

Using the divergence theorem in the plane[1], we obtain,

$$\oint_C \left[G_{ij}(\mathbf{r},\mathbf{r}_0)\ \sigma_{ik}(\mathbf{r}) - \mu\ u_i(\mathbf{r})\ T_{ijk}(\mathbf{r},\mathbf{r}_0) \right] n_k(\mathbf{r})\ \mathrm{d}l(\mathbf{r}) = 0\,. \tag{B.13}$$

Integral representation

Now consider two Stokes flow, one is due to a point force (B.14) with the corresponding velocity and stress tensor $(\mathbf{u}',\sigma')$, and a second unknown one, without a point force effect (B.15), where the velocity and stress tensor are $(\mathbf{u},\sigma)$. As we already know the solution for the fluid $(\mathbf{u}',\sigma')$, the idea is to use the second Green identity (or Lorentz reciprocal formula) to construct a solution for the second flow $(\mathbf{u},\sigma)$ from the solution of the fluid $(\mathbf{u}',\sigma')$,

$$-\nabla p' + \mu\ \nabla^2\mathbf{u}' = \nabla\sigma' = -\mathbf{f}\ \delta(\mathbf{r}-\mathbf{r}_0)\,, \tag{B.14}$$

$$-\nabla p + \mu\ \nabla^2\mathbf{u} = \nabla\sigma = 0\,. \tag{B.15}$$

The Green second identity relation (B.4) reads,

$$u_i'\ \frac{\partial\sigma_{ik}}{\partial x_k} - u_i\ \frac{\partial\sigma_{ik}'}{\partial x_k} = \frac{\partial}{\partial x_k}\left(u_i'\sigma_{ik} - u_i\sigma_{ik}'\right)\,. \tag{B.16}$$

From (B.15), we have,

$$\frac{\partial\sigma_{ik}}{\partial x_k} = 0\,. \tag{B.17}$$

And from (B.14), we have,

$$\frac{\partial\sigma_{ik}'}{\partial x_k} = -f_j\ \delta_{ij}\ \delta(\mathbf{r}-\mathbf{r}_0)\,. \tag{B.18}$$

Substituting the velocity and the stress field expressions in (B.6), and the derivatives in (B.17) and (B.18), into the Green's second identity relation in (B.16) we obtain,

$$u_i(\mathbf{r})\ \delta_{ij}\ \delta(\mathbf{r}-\mathbf{r}_0)\ f_j = \frac{\partial}{\partial x_k}\left(\frac{1}{4\pi\mu}\ G_{ij}(\mathbf{r},\mathbf{r}_0)\ f_j\ \sigma_{ik}(\mathbf{r}) - u_i(\mathbf{r})\ \frac{1}{4\pi}\ T_{ijk}(\mathbf{r},\mathbf{r}_0)\ f_j\right)\,. \tag{B.19}$$

Discarding f_j, and using the Kronecker delta definition ($u_i\delta_{ij} = u_j$) we obtain,

$$u_j(\mathbf{r})\ \delta(\mathbf{r}-\mathbf{r}_0) = \frac{1}{4\pi\mu}\ \frac{\partial}{\partial x_k}\left[G_{ij}(\mathbf{r},\mathbf{r}_0)\ \sigma_{ik}(\mathbf{r}) - \mu\ u_i(\mathbf{r})\ T_{ijk}(\mathbf{r},\mathbf{r}_0)\right] \tag{B.20}$$

Now integrating (B.20) over a selected area A that is enclosed by a contour denoted C, and using the Gauss divergence theorem in the plane for the right-hand side, we obtain,

[1] The divergence theorem of Gauss in the plane state that for any two-dimensional, and differentiable vector $\mathbf{V}$ over an area, we have

$$\iint_A \nabla\mathbf{V}\ \mathrm{d}S = \int_C \mathbf{V}\,\mathbf{n}\ \mathrm{d}l\,,$$

where l is the arc length along the contour C, and $\mathbf{n}$ is the unit normal vector on A pointing outward.

$$\begin{aligned}\iint_A u_j(\mathbf{r})\ \delta(\mathbf{r}-\mathbf{r}_0)\ \mathrm{d}S &= \iint_A \frac{1}{4\pi\mu}\ \frac{\partial}{\partial x_k}\left[G_{ij}(\mathbf{r},\mathbf{r}_0)\ \sigma_{ik}(\mathbf{r}) - \mu\ u_i(\mathbf{r})\ T_{ijk}(\mathbf{r},\mathbf{r}_0)\right]\ \mathrm{d}S \\ &= -\frac{1}{4\pi\mu}\ \oint_C G_{ij}(\mathbf{r},\mathbf{r}_0)\ \sigma_{ik}(\mathbf{r})\ n_k(\mathbf{r})\ \mathrm{d}l(\mathbf{r}) \\ &\quad + \frac{1}{4\pi}\ \oint_C u_i(\mathbf{r})\ T_{ijk}(\mathbf{r},\mathbf{r}_0)\ n_k(\mathbf{r})\ \mathrm{d}l(\mathbf{r})\,,\end{aligned} \tag{B.21}$$

where the unit normal vector $\mathbf{n}$ is pointing into the control area enclosed by C.

Next, and using the Dirac delta properties[2] on left-hand side of (B.21), we obtain,

$$\begin{aligned}u_j(\mathbf{r}_0) = &-\frac{1}{4\pi\mu}\ \oint_C G_{ij}(\mathbf{r},\mathbf{r}_0)\ f_i(\mathbf{r})\ \mathrm{d}l(\mathbf{r}) \\ &+\frac{1}{4\pi}\ \oint_C u_i(\mathbf{r})\ T_{ijk}(\mathbf{r},\mathbf{r}_0)\ n_k(\mathbf{r})\ \mathrm{d}l(\mathbf{r})\,,\end{aligned} \tag{B.22}$$

where $\mathbf{f} \equiv \sigma\,\mathbf{n}$ is the traction in the domain boundary. Equation (B.22) provides us with a representation of flow in terms of two distributions involving the stokeslet G_{ij} and the associated stresslet T_{ijk}. The first distribution on the right-hand of (B.22) is called the single-layer potential, and the second distribution is called the double-layer potential. The reason for this terminology is that for the single layer, the potentials are just superpositions of the hydrodynamic potentials of a point force, whereas the double layer potentials are those caused by a layer of sources (or sinks) and doublets of point forces [130, p.376].

Next, we examine the behavior of the boundary integral representation as the point $\mathbf{r}_0$ approaches the boundary A of a selected domain of the flow. Investigating the limit of the single-layer and the double-layer potential as $(\mathbf{r}-\mathbf{r}_0)$ tend to 0, we found that the stokeslet exhibits a weak singularity. The single-layer integral remains continuous as the point $\mathbf{r}_0$ approaches and then crosses A from either side. Whereas, the double-layer potential undergoes a discontinuity as the point $\mathbf{r}_0$ crosses the boundary A [132, p.16]. Applying the divergence theorem to the second equation in (B.11), and using the proprieties of Dirac delta function, we obtain,

$$\frac{1}{4\pi}\oint_C T_{ijk}(\mathbf{r},\mathbf{r}_0)n_k(\mathbf{r})\,\mathrm{d}l(\mathbf{r}) = \begin{cases}\delta_{ij} & \text{When } \mathbf{r}_0 \text{ is inside } C \\ \dfrac{1}{2}\,\delta_{ij} & \text{When } \mathbf{r}_0 \text{ is on } C \\ 0 & \text{When } \mathbf{r}_0 \text{ is outside } C\end{cases} \tag{B.23}$$

where the unit normal vector $n_k(\mathbf{r})$ points into the control area enclosed by C. Equation (B.23) can be written as,

$$\lim_{\mathbf{r}_0\to C}\oint_C u_i(\mathbf{r})T_{ijk}(\mathbf{r},\mathbf{r}_0)n_k(\mathbf{r})\,\mathrm{d}l(\mathbf{r}) = \oint_C^{PV} u_i(\mathbf{r})T_{ijk}(\mathbf{r},\mathbf{r}_0)n_k(\mathbf{r})\,\mathrm{d}l(\mathbf{r}) \pm 2\pi\ u_j(\mathbf{r}_0)\,. \tag{B.24}$$

[2]The integral of the product of an arbitrary function, $f(x)$, and the delta function over an interval that contains the point x_0 is

$$\int f(x)\ \delta(x-x_0)\ \mathrm{d}x = f(x_0)$$

Where the superscript PV indicates the principal value integral of the double layer potential found by placing the point $\mathbf{r}_0$ precisely on the contour C. The plus sign on the right-hand side of (B.24) applies when the point $\mathbf{r}_0$ approaches from the external side, in the direction of the normal vector $\mathbf{n}$, and the negative sign is when it approaches from the internal side.
Using the relation in (B.24), we finally obtain the boundary integral representation of the Stokes equation,

$$\begin{aligned} \alpha u_j(\mathbf{r}_0) = &- \frac{1}{4\pi\mu} \oint_C G_{ij}(\mathbf{r},\mathbf{r}_0)\, f_i(\mathbf{r})\ \mathrm{d}l(\mathbf{r}) \\ &+ \frac{1}{4\pi} \oint_C^{PV} u_i(\mathbf{r})\, T_{ijk}(\mathbf{r},\mathbf{r}_0)\, n_k(\mathbf{r})\ \mathrm{d}l(\mathbf{r})\,, \end{aligned} \tag{B.25}$$

where $\alpha = 0$ when $\mathbf{r}_0$ is outside A, $\alpha = 1$ when $\mathbf{r}_0$ is inside A, and $\alpha = 1/2$ when $\mathbf{r}_0$ is on C.

Appendix C

Boundary integral representation for flow past a closed interface

To describe the flow field around a closed interface, we use a boundary integral formulation that considers the flow on each side of the interface separately. We consider that the velocity is continuous across the interface, while the surface forces are discontinuous [22, p.139].

The boundary integral representation (B.22) at a point $\mathbf{r}_0$ in the external fluid disturbed by the presence of a closed interface reads,

$$\begin{aligned} u_j^{'}(\mathbf{r}_0) = &- \frac{1}{4\pi\mu} \oint_C G_{ij}(\mathbf{r},\mathbf{r}_0)\, f_i^{'}(\mathbf{r})\ \mathrm{d}l(\mathbf{r}) \\ &+ \frac{1}{4\pi} \oint_C u_i^{'}(\mathbf{r})\, T_{ijk}(\mathbf{r},\mathbf{r}_0)\, n_k(\mathbf{r})\ \mathrm{d}l(\mathbf{r})\,, \end{aligned} \tag{C.1}$$

where the prime symbol stands for the external perturbed flow and μ for the external viscosity. Now for the same point $\mathbf{r}_0$ that is located exterior to the closed interface, we apply the reciprocal identity in (B.13) for an incident exterior flow $\mathbf{u}^{\infty}$, we obtain,

$$\begin{aligned} 0 = &- \frac{1}{4\pi\mu} \oint_C G_{ij}(\mathbf{r},\mathbf{r}_0)\, f_i^{\infty}(\mathbf{r})\ \mathrm{d}l(\mathbf{r}) \\ &+ \frac{1}{4\pi} \oint_C u_i^{\infty}(\mathbf{r})\, T_{ijk}(\mathbf{r},\mathbf{r}_0)\, n_k(\mathbf{r})\ \mathrm{d}l(\mathbf{r})\,. \end{aligned} \tag{C.2}$$

Summing now the boundary integral representation for the disturbed external flow in (C.1) with the external incident flow in (C.2), we formulate the total external velocity $\mathbf{u}^{(2)} = \mathbf{u}^{\infty} + \mathbf{u}^{'}$ and the total traction force $\mathbf{f}^{(2)} = \mathbf{f}^{\infty} + \mathbf{f}^{'}$, we obtain,

$$\begin{aligned} u_j^{'}(\mathbf{r}_0) = &- \frac{1}{4\pi\mu} \oint_C G_{ij}(\mathbf{r},\mathbf{r}_0)\, f_i^{(2)}(\mathbf{r})\ \mathrm{d}l(\mathbf{r}) \\ &+ \frac{1}{4\pi} \oint_C u_i^{(2)}(\mathbf{r})\, T_{ijk}(\mathbf{r},\mathbf{r}_0)\, n_k(\mathbf{r})\ \mathrm{d}l(\mathbf{r})\,. \end{aligned} \tag{C.3}$$

Adding the incident velocity field $\mathbf{u}^{\infty}$ to both sides in (C.3), we obtain,

$$\begin{aligned} u_j^{(2)}(\mathbf{r}_0) =& u_j^{\infty}(\mathbf{r}) - \frac{1}{4\pi\mu} \oint_C G_{ij}(\mathbf{r},\mathbf{r}_0)\, f_i^{(2)}(\mathbf{r})\ \mathrm{d}l(\mathbf{r}) \\ &+ \frac{1}{4\pi} \oint_C u_i^{(2)}(\mathbf{r})\, T_{ijk}(\mathbf{r},\mathbf{r}_0)\, n_k(\mathbf{r})\ \mathrm{d}l(\mathbf{r})\,, \end{aligned} \tag{C.4}$$

where the superscript $^{(2)}$ stands for the total external flow.

Now we consider an internal flow with the velocity field $\mathbf{u}^{(1)}$ and the viscosity $\lambda\mu$, where λ is the viscosity ratio between the internal and external viscosity ($\lambda = \mu^{(1)}/\mu$). Applying the reciprocal theorem at the point $\mathbf{r}_0$ lying now in the internal fluid, we obtain,

$$\begin{aligned} 0 =& -\frac{1}{4\pi\lambda\mu} \oint_C G_{ij}(\mathbf{r},\mathbf{r}_0)\, f_i^{(1)}(\mathbf{r})\ \mathrm{d}l(\mathbf{r}) \\ &+ \frac{1}{4\pi} \oint_C u_i^{(1)}(\mathbf{r})\, T_{ijk}(\mathbf{r},\mathbf{r}_0)\, n_k(\mathbf{r})\ \mathrm{d}l(\mathbf{r})\,. \end{aligned} \tag{C.5}$$

Subtracting now (C.5) from (C.4), to formulate the difference between the total exterior traction $\mathbf{f}^{(2)}$ and the interior traction $\mathbf{f}^{(1)}$, we obtain,

$$\begin{aligned} u_j^{(2)}(\mathbf{r}_0) =& u_j^{\infty}(\mathbf{r}) - \frac{1}{4\pi\mu} \oint_C G_{ij}(\mathbf{r},\mathbf{r}_0)\ \left[f_i^{(2)} - f_i^{(1)}\right](\mathbf{r})\ \mathrm{d}l(\mathbf{r}) \\ &+ \frac{1}{4\pi} \oint_C \left[u_i^{(2)} - \lambda u_i^{(1)}\right](\mathbf{r})\, T_{ijk}(\mathbf{r},\mathbf{r}_0)\, n_k(\mathbf{r})\ \mathrm{d}l(\mathbf{r})\,. \end{aligned} \tag{C.6}$$

Setting the jump in traction across the interface as $\Delta\mathbf{f} = \mathbf{f}^{(2)} - \mathbf{f}^{(1)}$, and assuming that the velocity is continuous across the interface $\mathbf{u}^{\infty} + \mathbf{u}' = \mathbf{u}^{(2)} = \mathbf{u}^{(1)} = \mathbf{u}$, we derive the integral representation,

$$\begin{aligned} u_j(\mathbf{r}_0) =& u_j^{\infty}(\mathbf{r}) - \frac{1}{4\pi\mu} \oint_C G_{ij}(\mathbf{r},\mathbf{r}_0)\, \Delta f_i(\mathbf{r})\ \mathrm{d}l(\mathbf{r}) \\ &+ \frac{1-\lambda}{4\pi} \oint_C u_i(\mathbf{r})\, T_{ijk}(\mathbf{r},\mathbf{r}_0)\, n_k(\mathbf{r})\ \mathrm{d}l(\mathbf{r})\,. \end{aligned} \tag{C.7}$$

Now letting the point $\mathbf{r}_0$ approaching the closed interface from the outside, and using the relation in (B.24) (with the plus sign as $\mathbf{r}_0$ approaches from the external side of the considered interface), the right-hand side in (C.7) becomes,

$$\begin{aligned} u_j(\mathbf{r}_0) =& u_j^{\infty}(\mathbf{r}) - \frac{1}{4\pi\mu} \oint_C G_{ij}(\mathbf{r},\mathbf{r}_0)\, \Delta f_i(\mathbf{r})\ \mathrm{d}l(\mathbf{r}) \\ &+ \frac{1-\lambda}{4\pi} \oint_C^{PV} u_i(\mathbf{r})\, T_{ijk}(\mathbf{r},\mathbf{r}_0)\, n_k(\mathbf{r})\ \mathrm{d}l(\mathbf{r}) + \frac{1-\lambda}{2}\, u_j(\mathbf{r}_0)\,, \end{aligned} \tag{C.8}$$

where the superscript PV denotes the principal value of the double-layer potential (see B.23). Rearranging (C.8), we finally obtain the integral equation for the flow field around a closed interface, where the point $\mathbf{r}_0$ is lying in the interface,

$$\begin{aligned} \frac{1+\lambda}{2}\, u_j(\mathbf{r}_0) =& u_j^{\infty}(\mathbf{r}) - \frac{1}{4\pi\mu} \oint_C G_{ij}(\mathbf{r},\mathbf{r}_0)\, \Delta f_i(\mathbf{r})\ \mathrm{d}l(\mathbf{r}) \\ &+ \frac{1-\lambda}{4\pi} \oint_C^{PV} u_i(\mathbf{r})\, T_{ijk}(\mathbf{r},\mathbf{r}_0)\, n_k(\mathbf{r})\ \mathrm{d}l(\mathbf{r})\,. \end{aligned} \tag{C.9}$$

It will be noted that when the viscosities on each side of the interface are equal ($\lambda = 1$), the double-layer distribution vanish, and the flow is expressed only in terms of a single-layer potential, and when $\lambda = 0$ the particle becomes a rigid body. the jump in hydrodynamic traction across the interface may be expressed in terms of a constitutive law that may involve a number of physical constants, including the densities of the fluids, surface tension, surface viscosity, surface elasticity, and surface modules of bending and dilatation [22].

Bibliography

[1] Oguz K Baskurt, Max R Hardeman, and Michael W Rampling. *Handbook of hemorheology and hemodynamics*. Vol. 69. p. 34-36. IOS press, 2007.

[2] Robin Fåhraeus. "The suspension stability of the blood". In: *Physiological Reviews* 9.2 (1929), pp. 241–274.

[3] GER Lloyd. *Introduction to Hippocratic Writings. Translated by J. Chadwick and WN Mann*. p. 262. 1983.

[4] Kenneth D Keele. "Leonardo da Vinci's views on arteriosclerosis." In: *Medical history* 17.3 (1973), p. 304.

[5] Pedretti Keele. *Leonardo Da Vinci. Corpus of the Anatomical Studies in the Collection of Her Majesty the Queen at Windsor Castle.* p. 172. Johnson Reprint, 1979.

[6] William Harvey. "De motu cordis et sanguinis in animalibus". In: *Frankfort del Main. W. Fitzer* 1628 (1952).

[7] M Malpighius and II Epistel. "About the lungs". In: *Classics in Cardiology* 1 (1941), pp. 89–97.

[8] A Van Leeuwenhoek. "Microscopical observations concerning blood, milk, bones, the brain, spittle and cuticula". In: *Philosoph Trans Roy Soc London* 9 (1674), pp. 121–128.

[9] A Schierbeek. "The collected letters of Antoni van Leeuwenhoek". In: *Antonie van Leeuwenhoek* 19.1 (1953), pp. 181–188.

[10] Jean Leonard Poiseuille. *Recherches expérimentales sur le mouvement des liquides dans les tubes de très-petits diamètres*. Imprimerie Royale, 1844.

[11] Gotthilf Hagen. "Ueber die Bewegung des Wassers in engen cylindrischen Röhren". In: *Annalen der Physik* 122.3 (1839), pp. 423–442.

[12] Robin Fåhræus and Torsten Lindqvist. "The viscosity of the blood in narrow capillary tubes". In: *American Journal of Physiology–Legacy Content* 96.3 (1931), pp. 562–568.

[13] Aleksander S Popel and Paul C Johnson. "Microcirculation and hemorheology". In: *Annu. Rev. Fluid Mech.* 37 (2005), pp. 43–69.

[14] R Skalak and PI Branemark. "Deformation of red blood cells in capillaries". In: *Science* 164.3880 (1969), pp. 717–719.

[15] Wolfgang Helfrich. "Elastic properties of lipid bilayers: theory and possible experiments". In: *Zeitschrift für Naturforschung C* 28.11-12 (1973), pp. 693–703.

[16] Prosenjit Bagchi, Paul C Johnson, and Aleksander S Popel. "Computational fluid dynamic simulation of aggregation of deformable cells in a shear flow". In: *Journal of biomechanical engineering* 127.7 (2005), pp. 1070–1080.

[17] Junfeng Zhang, Paul C Johnson, and Aleksander S Popel. "Red blood cell aggregation and dissociation in shear flows simulated by lattice Boltzmann method". In: *Journal of biomechanics* 41.1 (2008), pp. 47–55.

[18] R Skalak et al. "Strain energy function of red blood cell membranes". In: *Biophysical Journal* 13.3 (1973), pp. 245–264.

[19] Charles S Peskin. "Numerical analysis of blood flow in the heart". In: *Journal of computational physics* 25.3 (1977), pp. 220–252.

[20] Charles S Peskin. "The immersed boundary method". In: *Acta numerica* 11 (2002), pp. 479–517.

[21] GK Youngren and Andrias Acrivos. "Stokes flow past a particle of arbitrary shape: a numerical method of solution". In: *Journal of fluid Mechanics* 69.2 (1975), pp. 377–403.

[22] C. Pozrikidis. *Boundary integral and singularity methods for linearized viscous flow*. Cambridge University Press, 1992.

[23] HL Goldsmith, Jean Marlow, and Frank Campbell MacIntosh. "Flow behaviour of erythrocytes-I. Rotation and deformation in dilute suspensions". In: *Proc. R. Soc. Lond. B* 182.1068 (1972), pp. 351–384.

[24] Thomas M Fischer, M Stohr-Lissen, and Holger Schmid-Schonbein. "The red cell as a fluid droplet: tank tread-like motion of the human erythrocyte membrane in shear flow". In: *Science* 202.4370 (1978), pp. 894–896.

[25] Manouk Abkarian, Magalie Faivre, and Annie Viallat. "Swinging of red blood cells under shear flow". In: *Physical review letters* 98.18 (2007), p. 188302.

[26] M Mason Guest et al. "Red blood cells: change in shape in capillaries". In: *Science* 142.3597 (1963), pp. 1319–1321.

[27] Manouk Abkarian et al. "Cellular-scale hydrodynamics". In: *Biomedical materials* 3.3 (2008), p. 034011.

[28] Giovanna Tomaiuolo et al. "Red blood cell deformation in microconfined flow". In: *Soft Matter* 5.19 (2009), pp. 3736–3740.

[29] Gerrit Danker et al. "Dynamics and rheology of a dilute suspension of vesicles: Higher-order theory". In: *Physical Review E* 76.4 (2007), p. 041905.

[30] Marine Thiébaud and Chaouqi Misbah. "Rheology of a vesicle suspension with finite concentration: A numerical study". In: *Physical Review E* 88.6 (2013), p. 062707.

[31] B Kaoui et al. "Complexity of vesicle microcirculation". In: *Physical Review E* 84.4 (2011), p. 041906.

[32] N Tahiri et al. "On the problem of slipper shapes of red blood cells in the microvasculature". In: *Microvascular research* 85 (2013), pp. 40–45.

[33] Othmane Aouane et al. "Vesicle dynamics in a confined Poiseuille flow: From steady state to chaos". In: *Physical Review E* 90.3 (2014), p. 033011.

[34] Dmitry A Fedosov, Matti Peltomäki, and Gerhard Gompper. "Deformation and dynamics of red blood cells in flow through cylindrical microchannels". In: *Soft matter* 10.24 (2014), pp. 4258–4267.

[35] Colin Gerald Caro, TJ Pedley, and RC Schroter. *The mechanics of the circulation*. Cambridge University Press, 2012.

[36] CNX OpenStax. *OpenStax, Anatomy & Physiology*. https://cnx.org/contents/FPtK1zmh@8.108:zMTtFGyH@4. pp. 889-896. 2017.

[37] Marshall A Lichtman. "Rheology of Leukocytes, Leukocyte Suspensions, and Blood in Leukemia POSSIBLE RELATIONSHIP TO CLINICAL MANIFESTATIONS". In: *Journal of Clinical Investigation* 52.2 (1973), p. 350.

[38] Shu Chien. "Red cell deformability and its relevance to blood flow". In: *Annual review of physiology* 49.1 (1987), pp. 177–192.

[39] P Janmey. "Cell membranes and the cytoskeleton". In: *Handbook of biological physics* 1 (1995), pp. 805–49.

[40] RP Rand and AC Burton. "Mechanical properties of the red cell membrane: I. Membrane stiffness and intracellular pressure". In: *Biophysical Journal* 4.2 (1964), pp. 115–135.

[41] RP Rand. "Mechanical properties of the red cell membrane: II. Viscoelastic breakdown of the membrane". In: *Biophysical Journal* 4.4 (1964), pp. 303–316.

[42] HL Reid et al. "A simple method for measuring erythrocyte deformability." In: *Journal of clinical pathology* 29.9 (1976), p. 855.

[43] Marita L Rodriguez, Patrick J McGarry, and Nathan J Sniadecki. "Review on cell mechanics: experimental and modeling approaches". In: *Applied Mechanics Reviews* 65.6 (2013), p. 060801.

[44] Bill Daily, Elliot L Elson, and G Ireneus Zahalak. "Cell poking. Determination of the elastic area compressibility modulus of the erythrocyte membrane". In: *Biophysical journal* 45.4 (1984), pp. 671–682.

[45] Daehwan Shin and Kyriacos Athanasiou. "Cytoindentation for obtaining cell biomechanical properties". In: *Journal of Orthopaedic Research* 17.6 (1999), pp. 880–890.

[46] Pierre Zachee et al. "Imaging red blood cells with the atomic force microscope". In: *British journal of haematology* 95.3 (1996), pp. 472–481.

[47] Kristen E Bremmell, Allan Evans, and Clive A Prestidge. "Deformation and nano-rheology of red blood cells: An AFM investigation". In: *Colloids and Surfaces B: Biointerfaces* 50.1 (2006), pp. 43–48.

[48] Ming Dao, Chwee Teck Lim, and Subra Suresh. "Mechanics of the human red blood cell deformed by optical tweezers". In: *Journal of the Mechanics and Physics of Solids* 51.11 (2003), pp. 2259–2280.

[49] Jochen Guck et al. "The optical stretcher: a novel laser tool to micromanipulate cells". In: *Biophysical journal* 81.2 (2001), pp. 767–784.

[50] Ihab Sraj et al. "Cell deformation cytometry using diode-bar optical stretchers". In: *Journal of biomedical optics* 15.4 (2010), pp. 047010–047010.

[51] Moritz K Kreysing et al. "The optical cell rotator". In: *Optics Express* 16.21 (2008), pp. 16984–16992.

[52] Jochen Guck et al. "Optical deformability as an inherent cell marker for testing malignant transformation and metastatic competence". In: *Biophysical journal* 88.5 (2005), pp. 3689–3698.

[53] Roe E Wells, Robert Denton, and Edward W Merrill. "Measurement of viscosity of biologic fluids by cone plate viscometer". In: *The Journal of laboratory and clinical medicine* 57.4 (1961), pp. 646–656.

[54] Giovanna Tomaiuolo et al. "Microfluidics analysis of red blood cell membrane viscoelasticity". In: *Lab on a Chip* 11.3 (2011), pp. 449–454.

[55] Gene Hou, Jin Wang, and Anita Layton. "Numerical methods for fluid-structure interaction—a review". In: *Communications in Computational Physics* 12.2 (2012), pp. 337–377.

[56] Chaouqi Misbah. "Vesicles, capsules and red blood cells under flow". In: *Journal of Physics: Conference Series*. Vol. 392. 1. IOP Publishing. 2012, p. 012005.

[57] Dominique Barthes-Biesel. "Motion and deformation of elastic capsules and vesicles in flow". In: *Annual Review of Fluid Mechanics* 48 (2016), pp. 25–52.

[58] Alec D Bangham and RW Horne. "Negative staining of phospholipids and their structural modification by surface-active agents as observed in the electron microscope". In: *Journal of molecular biology* 8.5 (1964), 660IN2–668IN10.

[59] MJ Hope et al. "Production of large unilamellar vesicles by a rapid extrusion procedure. Characterization of size distribution, trapped volume and ability to maintain a membrane potential". In: *Biochimica et Biophysica Acta (BBA)-Biomembranes* 812.1 (1985), pp. 55–65.

[60] Miglena I Angelova and Dimiter S Dimitrov. "Liposome electroformation". In: *Faraday discussions of the Chemical Society* 81 (1986), pp. 303–311.

[61] Ting Wang et al. "Preparation of submicron unilamellar liposomes by freeze-drying double emulsions". In: *Biochimica et Biophysica Acta (BBA)-Biomembranes* 1758.2 (2006), pp. 222–231.

[62] M Hishida et al. "Hydration process of multi-stacked phospholipid bilayers to form giant vesicles". In: *Chemical Physics Letters* 455.4 (2008), pp. 297–302.

[63] Dirk van Swaay et al. "Microfluidic methods for forming liposomes". In: *Lab on a Chip* 13.5 (2013), pp. 752–767.

[64] Yannick Lefebvre et al. "Flow of artificial microcapsules in microfluidic channels: A method for determining the elastic properties of the membrane". In: *Physics of Fluids* 20.12 (2008), p. 123102.

[65] Constantine Pozrikidis. *Modeling and simulation of capsules and biological cells*. CRC Press, 2003, Chapter.2.

[66] SS Bansode et al. "Microencapsulation: a review". In: *International Journal of Pharmaceutical Sciences Review and Research* 1.2 (2010), pp. 38–43.

[67] Albert Edward Green and Wolfgang Zerna. *Theoretical elasticity*. Courier Corporation, 1992.

[68] Raymond W Ogden. *Non-linear elastic deformations*. Courier Corporation, 1997.

[69] EA Evans. "A new material concept for the red cell membrane". In: *Biophysical journal* 13.9 (1973), pp. 926–940.

[70] Timm Krüger et al. *The Lattice Boltzmann Method*. Springer, 2017.

[71] Udo Seifert, Karin Berndl, and Reinhard Lipowsky. "Shape transformations of vesicles: Phase diagram for spontaneous-curvature and bilayer-coupling models". In: *Physical Review A* 44.2 (1991), p. 1182.

[72] Peter B Canham. "The minimum energy of bending as a possible explanation of the biconcave shape of the human red blood cell". In: *Journal of theoretical biology* 26.1 (1970), 61IN777–76IN881.

[73] Gerhard Gompper and Michael Schick. *Soft Matter: Volume 4-Lipid Bilayers and Red Blood Cells*. Vol. 4. Wiley-VCH, 2008, p.107–123.

[74] Saša Svetina et al. "The cooperative role of membrane skeleton and bilayer in the mechanical behaviour of red blood cells". In: *Bioelectrochemistry* 62.2 (2004), pp. 107–113.

[75] E.Evans and R.Skalak. *Mechanics and thermodynamics of biomembranes*. CRC PressI Llc, 1980.

[76] Udo Seifert. "Fluid membranes in hydrodynamic flow fields: Formalism and an application to fluctuating quasispherical vesicles in shear flow". In: *The European Physical Journal B-Condensed Matter and Complex Systems* 8.3 (1999), pp. 405–415.

[77] Badr Kaoui et al. "Lateral migration of a two-dimensional vesicle in unbounded Poiseuille flow". In: *Physical Review E* 77.2 (2008), p. 021903.

[78] Dominique Barthes-Biesel, Anna Diaz, and Emmanuelle Dhenin. "Effect of constitutive laws for two-dimensional membranes on flow-induced capsule deformation". In: *Journal of Fluid Mechanics* 460 (2002), pp. 211–222.

[79] V Adrian Parsegian. *Van der Waals forces: a handbook for biologists, chemists, engineers, and physicists*. Cambridge University Press, 2006.

[80] Jacob N Israelachvili. *Intermolecular and surface forces*. Academic press, 2011.

[81] Sho Asakura and Fumio Oosawa. "Interaction between particles suspended in solutions of macromolecules". In: *Journal of Polymer Science Part A: Polymer Chemistry* 33.126 (1958), pp. 183–192.

[82] Shu Chien. "Biophysical behavior of red cells in suspensions". In: *The red blood cell* 2.4 (1975), pp. 1031–133.

[83] Giovanna Tomaiuolo et al. "Red blood cell clustering in Poiseuille microcapillary flow". In: *Physics of Fluids* 24.5 (2012), p. 051903.

[84] Krzysztof Boryczko, Witold Dzwinel, and David A Yuen. "Dynamical clustering of red blood cells in capillary vessels". In: *Journal of molecular modeling* 9.1 (2003), pp. 16–33.

[85] Geert W Schmid-Schönbein et al. "The interaction of leukocytes and erythrocytes in capillary and postcapillary vessels". In: *Microvascular research* 19.1 (1980), pp. 45–70.

[86] Dominique Barthes-Biesel and JM Rallison. "The time-dependent deformation of a capsule freely suspended in a linear shear flow". In: *Journal of Fluid Mechanics* 113 (1981), pp. 251–267.

[87] Chaouqi Misbah. "Vacillating breathing and tumbling of vesicles under shear flow". In: *Physical review letters* 96.2 (2006), p. 028104.

[88] S Ramanujan and C Pozrikidis. "Deformation of liquid capsules enclosed by elastic membranes in simple shear flow: large deformations and the effect of fluid viscosities". In: *Journal of Fluid Mechanics* 361 (1998), pp. 117–143.

[89] Charles D Eggleton and Aleksander S Popel. "Large deformation of red blood cell ghosts in a simple shear flow". In: *Physics of fluids* 10.8 (1998), pp. 1834–1845.

[90] Prosenjit Bagchi. "Mesoscale simulation of blood flow in small vessels". In: *Biophysical journal* 92.6 (2007), pp. 1858–1877.

[91] C. Pozrikidis. "Interfacial dynamics for Stokes flow". In: *Journal of Computational Physics* 169.2 (2001), pp. 250–301.

[92] J Beaucourt et al. "Steady to unsteady dynamics of a vesicle in a flow". In: *Physical Review E* 69.1 (2004), p. 011906.

[93] Prasanta Kumar Banerjee and Roy Butterfield. *Boundary element methods in engineering science*. Vol. 17. McGraw-Hill London, 1981.

[94] MH Aliabadi and PH Wen. *Boundary element methods in engineering and sciences*. Vol. 4. World Scientific, 2011.

[95] JR Blake. "A note on the image system for a Stokeslet in a no-slip boundary". In: *Mathematical Proceedings of the Cambridge Philosophical Society*. Vol. 70. 2. Cambridge University Press. 1971, pp. 303–310.

[96] Horace Lamb. *Hydrodynamics*. Cambridge university press, 1932.

[97] Nadav Liron and S Mochon. "Stokes flow for a stokeslet between two parallel flat plates". In: *Journal of Engineering Mathematics* 10.4 (1976), pp. 287–303.

[98] Sai K Doddi and Prosenjit Bagchi. "Effect of inertia on the hydrodynamic interaction between two liquid capsules in simple shear flow". In: *International journal of multiphase flow* 34.4 (2008), pp. 375–392.

[99] Michael M Dupin et al. "Modeling the flow of dense suspensions of deformable particles in three dimensions". In: *Physical Review E* 75.6 (2007), p. 066707.

[100] T Biben and C Misbah. "An advected-field method for deformable entities under flow". In: *The European Physical Journal B-Condensed Matter and Complex Systems* 29.2 (2002), pp. 311–316.

[101] Zakaria Boujja et al. "Vesicle dynamics in confined steady and harmonically modulated Poiseuille flows". In: *Physical Review E* 98.4 (2018), p. 043111.

[102] Thierry Biben, Klaus Kassner, and Chaouqi Misbah. "Phase-field approach to three-dimensional vesicle dynamics". In: *Physical Review E* 72.4 (2005), p. 041921.

[103] Thierry Biben, Alexander Farutin, and Chaouqi Misbah. "Three-dimensional vesicles under shear flow: Numerical study of dynamics and phase diagram". In: *Physical Review E* 83.3 (2011), p. 031921.

[104] VV Lebedev, KS Turitsyn, and SS Vergeles. "Dynamics of nearly spherical vesicles in an external flow". In: *Physical review letters* 99.21 (2007), p. 218101.

[105] Julien Deschamps et al. "Dynamics of a vesicle in general flow". In: *Proceedings of the National Academy of Sciences* 106.28 (2009), pp. 11444–11447.

[106] Luc Petit, Jean-Pierre Hulin, and Étienne Guyon. *Hydrodynamique physique 3e édition (2012)*. EDP sciences, 2012.

[107] Hiroshi Noguchi and Gerhard Gompper. "Shape transitions of fluid vesicles and red blood cells in capillary flows". In: *Proceedings of the National Academy of Sciences of the United States of America* 102.40 (2005), pp. 14159–14164.

[108] Victoria Vitkova, M Mader, and Thomas Podgorski. "Deformation of vesicles flowing through capillaries". In: *EPL (Europhysics Letters)* 68.3 (2004), p. 398.

[109] Gwennou Coupier et al. "Shape diagram of vesicles in Poiseuille flow". In: *Physical review letters* 108.17 (2012), p. 178106.

[110] Stefano Guido and Giovanna Tomaiuolo. "Microconfined flow behavior of red blood cells in vitro". In: *Comptes Rendus Physique* 10.8 (2009), pp. 751–763.

[111] Achim Guckenberger et al. "Numerical–experimental observation of shape bistability of red blood cells flowing in a microchannel". In: *Soft matter* 14.11 (2018), pp. 2032–2043.

[112] Bruce M Koeppen and Bruce A Stanton. *Cardiovascular Physiology 6th ed*. Elsevier Health Sciences, 1992.

[113] David N Ku et al. “Pulsatile flow and atherosclerosis in the human carotid bifurcation. Positive correlation between plaque location and low oscillating shear stress.” In: *Arteriosclerosis, thrombosis, and vascular biology* 5.3 (1985), pp. 293–302.

[114] A Farutin and C Misbah. “Rheology of vesicle suspensions under combined steady and oscillating shear flows”. In: *Journal of Fluid Mechanics* 700 (2012), pp. 362–381.

[115] Steffen Kessler, Reimar Finken, and Udo Seifert. “Elastic capsules in shear flow: Analytical solutions for constant and time-dependent shear rates”. In: *The European Physical Journal E: Soft Matter and Biological Physics* 29.4 (2009), pp. 399–413.

[116] D Matsunaga et al. “Deformation of a spherical capsule under oscillating shear flow”. In: *Journal of Fluid Mechanics* 762 (2015), pp. 288–301.

[117] Hiroshi Noguchi et al. “Dynamics of fluid vesicles in flow through structured microchannels”. In: *EPL (Europhysics Letters)* 89.2 (2010), p. 28002.

[118] David M Silver et al. “Estimation of pulsatile ocular blood flow from intraocular pressure”. In: *Acta Ophthalmologica* 67.S191 (1989), pp. 25–29.

[119] Isidore Mandelbaum and Winton H Burns. “Pulsatile and nonpulsatile blood flow”. In: *Jama* 191.8 (1965), pp. 657–660.

[120] T Ariman, MA Turk, and ND Sylvester. “On steady and pulsatile flow of blood”. In: *Journal of Applied Mechanics* 41.1 (1974), pp. 1–7.

[121] TAKASHI Nakajima et al. “Deformation response of red blood cells in oscillatory shear flow”. In: *American Journal of Physiology-Heart and Circulatory Physiology* 259.4 (1990), H1071–H1078.

[122] Steven W Smith et al. “The scientist and engineer’s guide to digital signal processing”. In: (1997).

[123] Edward Ozimek and Aleksander Sk. “Perception of amplitude and frequency modulated signals (mixed modulation)”. In: *The Journal of the Acoustical Society of America* 82.5 (1987), pp. 1598–1603.

[124] John Happel and Howard Brenner. *Low Reynolds number hydrodynamics: with special applications to particulate media*. Vol. 1. Springer Science & Business Media, 2012.

[125] George Mchedlishvili and Nobuji Maeda. “Blood flow structure related to red cell flow: determinant of blood fluidity in narrow microvessels”. In: *The Japanese journal of physiology* 51.1 (2001), pp. 19–30.

[126] Viviana Claverıa et al. “Clusters of red blood cells in microcapillary flow: hydrodynamic versus macromolecule induced interaction”. In: *Soft matter* 12.39 (2016), pp. 8235–8245.

[127] Giovanni Ghigliotti et al. “Why and how does collective red blood cells motion occur in the blood microcirculation?” In: *Physics of Fluids* 24.10 (2012), p. 101901.

[128] Othmane Aouane et al. “Hydrodynamic pairing of soft particles in a confined flow”. In: *Physical Review Fluids* 2.6 (2017), p. 063102.

[129] J Liam McWhirter, Hiroshi Noguchi, and Gerhard Gompper. “Flow-induced clustering and alignment of vesicles and red blood cells in microcapillaries”. In: *Proceedings of the National Academy of Sciences* 106.15 (2009), pp. 6039–6043.

[130] Sangtae Kim and Seppo J Karrila. *Microhydrodynamics: principles and selected applications*. Courier Corporation, 2013.

[131] Jan KG Dhont. *An introduction to dynamics of colloids*. Vol. 2. Elsevier, 1996.

[132] Constantine Pozrikidis. *A practical guide to boundary element methods with the software library BEMLIB*. CRC Press, 2002.